

**CHARACTERIZATION AND MODELLING OF
EFFECTS OF CLEAR AIR ON MULTIPATH
FADING IN TERRESTRIAL LINKS**

by
Mike Omondi Asiyo

Dissertation submitted in fulfilment of the requirement for the degree
MASTER OF SCIENCE IN ENGINEERING: ELECTRONIC ENGINEERING
in the
School of Engineering

UNIVERSITY OF KWAZULU-NATAL

Supervisor: Prof. Thomas Joachim Odhiambo Afullo

March 2013

As the candidate's supervisor, I have approved this dissertation for submission.

SignedDate

Name: Prof. Thomas J. O. Afullo

Declaration 1 - Plagiarism

I, **Mike Omondi Asiyu**, declare that

1. The research reported in this dissertation, except where otherwise indicated, is my original research.
2. This dissertation has not been submitted for any degree or examination at any other university.
3. This dissertation does not contain other persons' data, pictures, graphs or other information, unless specifically acknowledged as being sourced from other persons.
4. This dissertation does not contain other persons' writing, unless specifically acknowledged as being sourced from other researchers. Where other written sources have been quoted, then:
 - (a) Their words have been re-written but the general information attributed to them has been referenced.
 - (b) Where their exact words have been used, then their writing has been placed in italics and inside quotation marks, and referenced.
5. This dissertation does not contain text, graphics or tables copied and pasted from the Internet, unless specifically acknowledged, and the source being detailed in the dissertation and in the References sections.

SignedDate

Declaration 2 - Publications

The following papers have been published and parts of their materials are included in the thesis:

Published Papers:

1. **M. O. Asiy**o and T. J. O. Afullo, “Tropospheric propagation mechanisms influencing multipath fading based on local measurements,” in *Proceedings of Southern Africa Telecommunication Networks and Applications Conference*, George, South Africa, 2-5 September, 2012, ISBN: 978-0-620-53713-1.
2. **M. O. Asiy**o and T. J. O. Afullo, “Statistical estimation of fade depth and outage predictions due to multipath propagation in Southern Africa,” *Progress in Electromagnetic Research Journal B*, vol.46, 251-274, 2013.

In the first paper we use radiosonde data to investigate the presence of anomalous conditions along three coastal towns in South Africa. We also estimated fade depths exceeded for a certain percentage of time in two of the locations and investigated if there is correlation between these estimated fade depths and the anomalous conditions.

In the second paper, we determine the geoclimatic factor K for five locations in South Africa i.e., Durban, Pretoria, Cape Town, Bloemfontein and Polokwane. These values are estimated from point refractivity gradient derived from meteorological data obtained from South Africa Weather Service. The point refractivity gradient is estimated from cumulative distribution curves of refractivity gradients. We use inverse distance weighting method to estimate this value in cases where it is not directly available from the distribution curves. The values of estimated geoclimatic factor are used in estimating the probability that a certain fade depth is exceeded for a certain percentage of time. Outage probabilities are also estimated given that the fade depth exceeded falls below the squelch level. We compare our findings with earlier work done in Durban (South Africa) and Rwanda (Central Africa).

Accepted Papers:

1. **M. O. Asiy**o and T. J. O. Afullo, “Spatial interpolation techniques for mapping geoclimatic factor K in South Africa,” in *Proceedings of Progress in Electromagnetic Research Symposium*, Taipei, Taiwan, 25-28 March, 2013.

In this paper, we have applied three interpolation techniques to estimate the geoclimatic factor for the whole of South Africa from values obtained in five locations derived from radiosonde sounding data. We investigate the accuracy of each of the three methods by

determining the root mean square error (RMSE) and the mean absolute error (MAE) from five control points. The method that provides the lowest value of these error parameters is assumed to be the best interpolation technique for our data and its interpolated values taken as the best estimates.

SignedDate

Acknowledgements

First and foremost, I would like to sincerely extend my greatest appreciation to my supervisor, Professor Thomas Joachim Odhiambo Afullo, for his guidance, constructive criticism, advice and encouragement throughout my masters program. This dissertation could not have been without his tireless effort.

Many thanks to the staff at the Department of Electrical, Electronic and Computer Engineering for the invaluable time you accorded me when in need. Special thanks to Professor Jules Tapamo, for introducing me to \LaTeX , the effort can be clearly seen in the way this dissertation is presented. His encouragement cannot go unnoticed, more so when my supervisor was away on sabbatical leave. His words “see everything as a challenge, prove them wrong,” will ever remain with me.

I would also like to extend my sincere gratitude to my colleagues, especially, Mr Abraham Nyete, Mr Adetan Oluwumi, Mr Peter Akuon, Mr Akintunde Alonge and Ms Fulatsa Zwane, for the their precious time they accorded me whenever I needed their co-operation.

Special thanks to my family for the sacrifice and perseverance of staying alone during my study period. Thanks for your unwavering support and, more important your love.

May our good Lord abundantly bless all of you and your families!

Abstract

The increased application of digital terrestrial microwave radio links in communication networks has renewed attention in techniques of estimating the probability of multipath fading distributions. Nevertheless, the unpredictable variation of the wireless transmission medium remains a challenge. It has been ascertained that the refraction of electromagnetic waves is due to the inhomogeneous spatial distribution of the refractive index, and causes adverse effects such as multipath and diffraction fading. The knowledge of the characteristics of such causes of these fading phenomena is essential for the accurate design of terrestrial line of sight (LOS) links of high performance and availability. Refractivity variation is random in space and time and cannot be described in a deterministic manner and has to be considered as a random variable with probabilistic characteristics.

In this dissertation, radiosonde soundings data is used in characterizing the atmospheric conditions and determining the geoclimatic factor K used in predicting the distribution of multipath fading for five locations in South Africa. The limitations of radiosonde measurements are lack of time resolution and poor spatial resolution. The latter has been reduced by spatial interpolation techniques in our study, specifically, the Inverse Distance Weighting (IDW) method. This is used in determining the point refractivity gradient not exceeded for 1 % of the time from which the geoclimatic factor is estimated. Fade depth and outage probability due to multipath propagation is then predicted from the International Telecommunications Union Recommendations (ITU-R) techniques. The results are compared with values from Central Africa. The results obtained using the ITU-R method are also compared with region-based models of Bennett-Vigants of USA and Morita of Japan.

Three spatial interpolation techniques (Kriging, Thin-Plate Spline and Inverse Distance Weighting) are then used in interpolating the geoclimatic factor K in places where radiosonde data is not available. The estimated values have been used to develop contour maps for geoclimatic factor K for South Africa. Statistical assessment of these methods is done by calculating the root mean square error (RMSE) and the mean absolute error (MAE) between a set of control points and the interpolated results. The best performing method is used to map the seasonal geoclimatic factor K for the entire study region. The estimated values of geoclimatic factor will improve accuracy in predicting outage probability due to multipath propagation in LOS links in the region which is a key contribution of this work.

Contents

Declaration 1 - Plagiarism	ii
Declaration 2 - Publications	iii
Acknowledgements	v
Abstract	vi
Table of Contents	vii
List of Figures	x
List of Tables	xiii
1 Introduction	1
1.1 Motivation	1
1.2 Research Questions	3
1.3 Objectives	3
1.4 Methodological Approach	3
1.5 Significance of the Study	4
1.6 Scope of Dissertation	4
1.7 Dissertation Organization	4
2 Tropospheric Propagation and Link Design: A Survey	5
2.1 Introduction	5
2.2 Tropospheric Propagation	5
2.2.1 Atmospheric Mechanisms	5
2.2.2 Refractivity Gradient	6
2.2.3 Effective Earth Radius	7
2.2.4 Standard Propagation Mechanisms	9
2.2.5 Anomalous Propagation Mechanisms	10

2.3	Other Atmospheric Effects	13
2.4	Link design	13
2.4.1	Initial Planning and Site Selection	14
2.4.2	Path Profile	14
2.4.3	Free Space Path Loss	16
2.4.4	Link Budget	16
2.4.5	Fade Margin and Link Availability	17
2.4.6	Site Survey	17
2.5	Chapter Conclusion	18
3	Multipath Fading Predictions and Interpolation Techniques	19
3.1	Introduction	19
3.2	Multipath Fading Predictions	19
3.2.1	Morita Method	20
3.2.2	Barnett-Vigants Method	20
3.2.3	ITU-R Methods	22
3.3	Recent Clear-air Radioclimatological Studies in South Africa	25
3.3.1	Odedina and Afullo	26
3.3.2	Palmer and Barker	27
3.4	Spatial Interpolation Techniques	29
3.4.1	Kriging	29
3.4.2	Thin Plate Spline	32
3.4.3	Inverse Distance Weighting	33
3.4.4	Comparison of the three Interpolation Techniques	34
3.5	Chapter Conclusion	35
4	Statistical Estimation of Fade Depth and Outage Probability	36
4.1	Introduction	36
4.2	Study Area	36
4.3	Data Collection and Processing	38
4.4	Geoclimatic Factor Determination	38
4.5	Fade Depth Prediction	40

4.6	Results and Discussion	40
4.6.1	Refractivity and Refractivity Gradient	41
4.6.2	Geoclimatic Factor	45
4.6.3	Fade Depth and Outage Prediction	53
4.7	Validation and Comparison of Results	59
4.8	Chapter Conclusion	63
5	Mapping of Geoclimatic Factor K	64
5.1	Introduction	64
5.2	Applications of Spatial Interpolation Methods	64
5.2.1	Kriging	65
5.2.2	Thin Plate Spline	65
5.2.3	Inverse Distance Weighting (IDW)	66
5.3	Methodology	66
5.3.1	Data Collection	66
5.3.2	Data Processing	67
5.3.3	Error Analysis	67
5.4	Results and Discussion	68
5.5	Chapter Conclusion	79
6	Conclusion	80
6.1	Concluding Remarks	80
6.2	Future Work	81
	References	82

List of Figures

2.1	Variation of the ray curvature at different vales of k [1]	8
2.2	Optical LOS versus radio LOS [2]	8
2.3	Ducting conditions with radio waves trapped between trapping layer and Earth's surface [1]	11
2.4	Ducting conditions with radio waves trapped between two trapping layers [1]	12
2.5	Huygen's principle [3]	15
2.6	First Fresnel Zone Radius [1]	16
4.1	The Map of South Africa [4]	37
4.2	Cumulative Distribution Curve for $\frac{dN}{dh}$	39
4.3	Monthly variation of three coastal regions' Mean surface refractivity	42
4.4	Monthly variation of three coastal regions' Standard deviation for surface refractivity	42
4.5	Occurrence of super-refractivity conditions for three coastal regions in South Africa	43
4.6	Cumulative distribution of the monthly refractivity gradient for Durban . .	43
4.7	Cumulative distribution of the monthly refractivity gradient for Cape Town	44
4.8	Cumulative distribution of the monthly refractivity gradient for Port Elizabeth	44
4.9	Monthly variation of point refractivity gradient (dN_1) for Durban	45
4.10	Monthly variation of point refractivity gradient (dN_1) for Cape Town . . .	46
4.11	Monthly variation of point refractivity gradient (dN_1) for Pretoria	46
4.12	Monthly variation of point refractivity gradient (dN_1) for Bloemfontein . .	47
4.13	Monthly variation of point refractivity gradient (dN_1) for Polokwane.	47
4.14	Confidence intervals graph for the yearly average of point refractivity gradient for each of the five sites in South Africa	51
4.15	Seasonal variation of point refractivity gradient (dN_1)	53
4.16	Seasonal variation of geoclimatic factor K	53
4.17	Probability of time a specific fade depth A (dB) is exceeded for Durban . . .	54
4.18	Probability of time a specific fade depth A (dB) is exceeded for Cape Town	55

4.19	Probability of time a specific fade depth $A(\text{dB})$ is exceeded for Pretoria . . .	55
4.20	Probability of time a specific fade depth $A(\text{dB})$ is exceeded for Bloemfontein	56
4.21	Probability of time a specific fade depth $A(\text{dB})$ is exceeded for Polokwane .	56
4.22	Fade depth exceeded for 0.01 % of the time with varying frequency at fixed path length (48.25 km)	58
4.23	Fade depth exceeded for 0.01 % of the time with varying path length at fixed frequency (11 GHz)	58
4.24	Monthly Mean Received Signal Level for Jali-Gahengeri Link [5]	61
4.25	Monthly Mean Received Signal Level for Gahengeri-Kibungo Link [5]	61
4.26	Monthly Mean Received Signal Level for Nyakarambi-Nasho Link [5]	61
5.1	Contour plot for the geoclimatic factor K for February using inverse distance weighting	69
5.2	Contour plot for the geoclimatic factor K for February using thin-plate spline	69
5.3	Contour plot for the geoclimatic factor K for February using kriging (spherical)	70
5.4	Contour plot for the geoclimatic factor K for February using kriging (exponential)	70
5.5	Contour plot for the geoclimatic factor K for February using kriging (Gaussian)	71
5.6	Contour plot for the geoclimatic factor K for May using inverse distance weighting	71
5.7	Contour plot for the geoclimatic factor K for May using thin-plate spline .	72
5.8	Contour plot for the geoclimatic factor K for May using kriging (spherical)	72
5.9	Contour plot for the geoclimatic factor K for May using kriging (exponential)	73
5.10	Contour plot for the geoclimatic factor K for May using kriging (Gaussian)	73
5.11	Contour plot for the geoclimatic factor K for August using inverse distance weighting	74
5.12	Contour plot for the geoclimatic factor K for August using thin-plate spline	74
5.13	Contour plot for the geoclimatic factor K for August using kriging (spherical)	75
5.14	Contour plot for the geoclimatic factor K for August using kriging (exponential)	75
5.15	Contour plot for the geoclimatic factor K for August using kriging (Gaussian)	76

5.16	Contour plot for the geoclimatic factor K for November using inverse distance weighting	76
5.17	Contour plot for the geoclimatic factor K for November using thin-plate spline,	77
5.18	Contour plot for the geoclimatic factor K for November using kriging (spherical)	77
5.19	Contour plot for the geoclimatic factor K for November using kriging (exponential)	78
5.20	Contour plot for the geoclimatic factor K for November using kriging (Gaussian)	78

List of Tables

2.1	Atmospheric refractive conditions	7
3.1	Coefficient C_o values for various types of link in(3.15) [6]	23
3.2	Variuos valus of both latitude and longitude coefficients [6,7]	24
3.3	Coefficient C_o values for various types of link in(3.16) [6]	24
3.4	Comparison of characteristics of spatial interpolation techniques	34
4.1	Data Samples per Month in each Year used in Determining Point Refrac- tivity Gradient	41
4.2	Worst Month Values	48
4.3	Geoclimatic Factor K for Durban	48
4.4	Geoclimatic Factor K for Pretoria	49
4.5	Geoclimatic Factor K for Cape Town	49
4.6	Geoclimatic Factor K for Bloemfontein	50
4.7	Geoclimatic Factor K for Polokwane	50
4.8	Comparison of ITU-R and Estimated Values of Point Refractivity Gradient and Geoclimatic Factor K	52
4.9	Comparison of fade depth exceeded for various link availability in Durban .	59
4.10	Comparison of outage probability of a typical link in Durban, a coastal town in South Africa: ITU-R vs Barnett-Vigants/Morita	60
4.11	Link Parameters in Rwanda, Central Africa [5]	60
4.12	Point refractivity gradient and geoclimatic factor values for regions in Tanzania	62
4.13	Outage probabilities for three links in Rwanda	62
5.1	Discrete Observable Data used in Mapping and their Latitudes/Longitudes	67
5.2	Error analysis applied to interpolation techniques	68

Chapter 1

Introduction

1.1 Motivation

Terrestrial fixed radio links operating at microwave frequencies on line-of-sight (LOS) paths are flexible, dependable and cost-effective means of providing point-to-point communications. They are heavily employed in carrying large numbers of voice, video, wide-band data transmissions, high definition TV channels, and high quality audio among others [8, 9]. Their performance and availability characteristics must be above a certain threshold in order to offer high quality of service. This calls for high precision equipment and devices in addition to knowledge of the transmission medium. For terrestrial LOS links, the transmission medium is the troposphere, with varying climatic conditions which affect the propagation of radio waves [8]. Usually, service availability of 99.99 % for the worst month is the design goal for fixed links; this implies an outage not exceeding 53 minutes in a year [10].

The probability of link unavailability in terrestrial microwave communication systems (for clear air) is largely determined by the refractive index gradient of the wireless medium. Knowledge of characteristics of propagation contributes greatly to the design of line-of-sight links and to improvement of system performance and availability. It has been observed that seasonal or diurnal variations of refractivity gradients do affect the signal and cause refractive fading. These include diffraction fading, beam spreading, multipath fading, which results in Rayleigh fading in narrowband systems and Rayleigh plus selective fading in wideband systems; and blackout fading (ducting). In the absence of rain the link outages depend on clear air conditions which are determined by the state of atmospheric refractivity. The atmospheric refractivity varies with time and space more or less randomly and full details of it are out of reach in practice. Hence the statistics of atmospheric refractivity and related effects are of interest in link design [11, 12].

Multipath fading, which is a major factor in microwave systems design, is associated with strong negative gradients more so for fixed links operating below 10 GHz. Below 10 GHz, multipath outage increases rapidly with path length. It also increases with frequency, climatic factors and average annual temperature. Multipath effect can be reduced with higher fade margin. If the path has excessive path outage the performance can be improved by using one of the diversity methods. Apart from clear-air, precipitation (rain, fog, etc.) also attenuates radio signals. It is worth noting that above 10 GHz, precipitation attenuation dominates the microwave and millimetre bands. In areas with heavy precipitation, if possible, use frequency bands below 10 GHz [1, 2].

The main purpose of propagation modelling is often to determine the probability of satisfactory performance of communication systems. The task of the microwave link designer is to ensure that outages resulting from these variations are kept at a minimum, thus adequate system fade margins are implemented to ensure this is so. Therefore, in order to take into consideration the statistical nature of radio wave propagation, appropriate performance prediction models are utilized. Prediction models for deep fading range of the multipath fading distribution have been in existence for several years, most of which are based on empirical fits of Rayleigh-type distributions to the fading data on individual countries. They include Morita model for Japan, the Barnett-Vigants model for the United States of America, the Doble and the Pearson for United Kingdom, among others [13,14].

These models have a variable that takes into account the regional/climatic types of the zone of interest. This factor for ITU-R models is the geoclimatic factor K . The geoclimatic factor is indicative of the geographical and climatic characteristics of a given region in [15]; it is used in estimating the multipath fading distributions. Multipath fading is a short period outage and is responsible to the performance of a given link. Its effective mitigation scheme needs a thorough knowledge of its characteristics.

This study focuses on the characterization and modelling of such effects of clear air on multipath fading in communication links. The characterization of the seasonal variation of fading and the influence of meteorological parameters to it provides the way to optimize transmission performance by adapting the transmission equipment design and usage to the amount of fading anticipated at a given site/place and time of the year. On the other hand, the modelling of these effects help in determining the probability of occurrence of fade duration, inter-fade duration and fade slope in a given climatic region; hence in the evaluation of internal parameters of fade mitigation technique(FMT) control loop.

There is continued research in prediction modelling either from fading measurements or from climatological data. There are mainly two types of models: theoretical models and statistical models. The most widely used theoretical models are ray-tracing and parabolic equation method [16]. Ray-tracing is a geometrical optics method while parabolic equation is a full wave approach to a homogeneous wave equation solution. Ray-tracing method has been modelled by different authors [16,17] and parabolic equation method by [16,18,19] among others. In comparing the two methods, the parabolic equation method provides a more accurate prediction tool because it is able to cater for both diffraction and refraction phenomena. Even though the parabolic equation method is popular, a comparison of its model and actual fading measurements shows some discrepancy, which can be attributed to the fact that the medium of radio propagation is inhomogeneous and the two methods work better for homogeneous media [16,18,19]. A promising solution is to approximate the spatial distribution of the gradient from meteorological ground data using statistical methods [19].

1.2 Research Questions

This study seeks to evaluate the effects of gases on multipath fading in terrestrial links. Our focus is based on the observation that most previous studies have concentrated on effects of clouds, rain and dust particles without taking into account clear-air perspectives. Some of the research questions that will be addressed in this study include the following:

1. What are the characteristics of clear air or what does clear air constitute of?
2. How do these characteristics affect the radio signal propagation?
3. How can the effects of these characteristics on the multipath fading be modelled in order to achieve the desirable signal propagation quality?

1.3 Objectives

The objectives of this study entail the following:

1. Use meteorological data to estimate the geoclimatic factor K for different locations in South Africa, and investigate its variation with month, season and year.
2. Compare the predicted probabilities of outage through the ITU-R models with other region-based prediction models.
3. Characterize and model the effects of clear air parameters on multipath fading in terrestrial links at microwave frequencies.
4. Extend the values of the estimated geoclimatic factor to other regions through interpolation techniques.

1.4 Methodological Approach

1. Literature review: this is to establish the existing related contributions and theoretical basis of the study.
2. Data gathering: use of meteorological data to estimate the signal attenuation and multipath fading.
3. Data analysis: to characterize the data and formulate the correlations of effects of clear air at different regions and seasons.
4. System modelling of such effects on multipath fading in terrestrial links.
5. Comparison and validation of results with other well established models

1.5 Significance of the Study

A proper understanding of the effects of the atmosphere will lead to the design of LOS links of high availability and performance. Under-designed links lead to outages hence loss of valuable communication time; while over-designed links lead to wastage of resources and/or interference of the link to other channels. Accurate predictions of multipath fading distributions will help in determining the right value of fade margin for the intended link availability. The knowledge of characteristics of effects of multipath fading will also help in appropriate selection of fade mitigation techniques for LOS links.

1.6 Scope of Dissertation

This study does not seek to model the channel of communication but the predicaments that affects the propagation of radio waves in the channel. The effects of the atmosphere on electromagnetic radio waves is characterized and modelled with respect to clear air phenomena only without considering precipitation and other atmospheric effects.

1.7 Dissertation Organization

The rest of this dissertation is organized as follows:

Chapter two entails a review of how the lowest part of the atmosphere affects the propagation of radio waves in microwave Line of Sight (LOS) links. A brief review on the LOS design procedure is also outlined.

In Chapter three, evolution of the following three multipath fading distribution prediction methods are discussed: Morita of Japan, Barnett-Vigants of USA and the global ITU-R models. Three spatial interpolation techniques (Kriging, Inverse Distance Weighting and Thin-plate Spline) are discussed and their characteristics compared.

Chapter four provides the results of radioclimatological studies in relation to multipath fading in terrestrial links. Refractivity gradient values in the lowest 65 m above the ground are used to estimate point refractivity gradient from which the geoclimatic factor is calculated. These values of geoclimatic factor for various regions are used in prediction of time that a certain fade depth is exceeded using ITU-R methods. A comparison with other models is also made.

In Chapter five, three spatial interpolation techniques are used to extend the obtained geoclimatic factor to the whole of South Africa. Performance assessment is done to recommend the most accurate method for mapping geoclimatic factor in the study region.

Concluding remarks on the findings of the study are given in Chapter six. Recommendations for future work are also given in the same chapter.

Chapter 2

Tropospheric Propagation and Link Design: A Survey

2.1 Introduction

The chapter gives an overview of atmospheric effects on microwave links. Tropospheric propagation mechanisms under standard and non-standard atmospheric conditions are discussed. Clear air parameters that cause signal fading in LOS links are discussed. The chapter also deals with an overview of link design steps.

2.2 Tropospheric Propagation

The troposphere is the lowest part of the earth's atmosphere that extends from the Earth's surface to about 9 km at the poles and to 17 km the equator respectively. Within this region of the atmosphere, the temperature generally decreases with increase in height at approximately $7^{\circ}\text{C}/\text{kilometre}$. Tropospheric weather variations affect the propagation of radio waves. Temperature, pressure and humidity vary in time and space in the lower atmosphere and this causes the refractive index of the air also to change with space [20]. Understanding of radio propagation characteristics in the troposphere is then crucial in the performance evaluation of line-of-sight (LOS) terrestrial links. The variation of the refractive index in the horizontal distribution is normally assumed to be homogeneous and only the vertical distribution is considered to be of significance in the almost horizontally propagating radio waves [20, 21].

2.2.1 Atmospheric Mechanisms

When a radio wave propagates in free space (a vacuum), where there is no atmosphere, it will follow a straight path. However, when the beam is propagated in the atmosphere where it come-across variations in atmospheric refractivity along its trajectory, it tends to curve. Atmospheric refractivity not only affects the curvature of the radio ray but will also give some insight into the fading phenomenon. Refractivity effects vary widely with altitude, geographical location, and weather conditions. Refractivity effects can allow beyond-the-horizon communication (or interference), or produce obstruction and diffraction from terrain that seems to be beneath the LOS and also cause multipath fading [2, 12].

2.2.2 Refractivity Gradient

The radio refractive index is the ratio of velocity of propagation of a radio wave in free space to the velocity in a specified medium. At standard atmospheric environments, close to the earth's surface, the radio refractive index, n , has a value of about 1.000312. It's value is always greater than unity but by a small fraction. Therefore, a more convenient quantity, the atmospheric refractivity N (N-units) is usually used and it is given [12]:

$$N = (n - 1) \times 10^6 \quad (2.1)$$

Substituting the value for the ground refractive index ($n = 1.000312$) into (2.1) yields a N value of 312 N-units. From ITU-R P.453, N can be modelled as [22]:

$$N = \frac{77.6}{T} \left(P + 4810 \frac{e}{T} \right) \quad (2.2)$$

where P (hPa) is the total atmospheric pressure ,
 e (hPa) is the water vapour pressure ,
 T (Kelvin) is the air temperature.

The value of N varies with altitude since relative humidity, temperature, and pressure all vary with height. Pressure and humidity normally decreases exponentially with height. Humidity and temperature do, however, change under certain conditions resulting in variations of radio refractivity [12]. In general, the atmosphere displays an exponential decrease of N with height. For the average atmosphere, the refractivity can be written as [22]:

$$N(h) = N_o \exp(-h/h_o) \quad (2.3)$$

where $N_o = 312$ N-units for standard atmosphere and for altitudes below 1 km, $h_o \simeq 7$ km [12].

As a radio link engineer, refractivity gradient is of greater interest. Assuming that refractive index, n , of air is inhomogeneous with height for the first few tenths of a kilometre above the earth's surface and is homogeneous in the horizontal direction; it can be approximated as a linear gradient [12]. The refractivity gradient is thus defined as [12]:

$$G = \frac{dN}{dh} \quad (2.4)$$

From (2.1), $n = (1 + N \times 10^{-6})$ giving

$$\frac{dn}{dh} = \frac{dN}{dh} \times 10^{-6} \quad N \text{ units/km} \quad (2.5)$$

and from (2.3),

$$\frac{dN}{dh} = -\frac{N_o}{h_o} \exp(-1/7) \quad (2.6)$$

For heights less than 1 km, dN/dh is well estimated by its value at 1 km:

$$\frac{dN}{dh}(1km) = \frac{-312}{7} \exp(-1/7) = -38.64 \quad Nunits/km \quad (2.7)$$

Refractivity gradients vary with time and experiments have shown that it can change from being positive to steeply negative [3]. When the refractivity gradient displays average characteristics, it is called standard refraction and corresponds to the commonly quoted value of $G = -39$ N-units/km. When it becomes positive, it is known as sub-refraction and can cause diffraction loss. When the gradient becomes more negative than $G = -100$ N-units/km, it is called super-refractive and results in multipath fading. When it becomes more negative than $G = -157$ N-units/km, ducting condition occurs resulting in severe multipath, beam spreading, and even blackout conditions. These refractivity gradients and their corresponding propagation conditions are summarized in Table 2.1.

Table 2.1: Atmospheric refractive conditions

Atmospheric condition	N-gradient
Trapping	< -157 N/km
Superrefractive	-157 to -79 N/km
Normal	-79 to 0 N/km
Subrefractive	> 0 N/km

2.2.3 Effective Earth Radius

Due to refraction of the signal, the radio beam does not propagate in a straight line. The bending of the ray depends on the point gradient of refractivity that the ray experiences at each point along the path. If these point gradients are averaged along the path, then it can be assumed that the ray follows a curved trajectory. Just as the radio is not a straight line, the earth's surface over which it travels is also not flat. The earth is not round but an oblate spheroid; but for simplicity, it's assumed to be an arc with an average radius of 6371 km. We now have a situation where the clearance of the radio beam over the earth's surface is dependent on the relative distance between two curves.

An analysis for clearance is made convenient if one of the curves is assumed to be straight and the other given an extra curvature for compensation. The radio ray is imagined to be straight line relative to an effective earth's radius, which has been adjusted by the refractivity gradient. This radius is the real earth's radius which has been multiplied by an earth radius factor k that is dependent on the refractivity gradient [3]:

$$k = \frac{r}{r_o} \quad (2.8)$$

where k is the effective earth radius factor,
 r is the effective earth radius and,
 r_o is the true earth radius.

The ray curvature for various values of k is shown in Figure 2.1 [1]. The modified radius

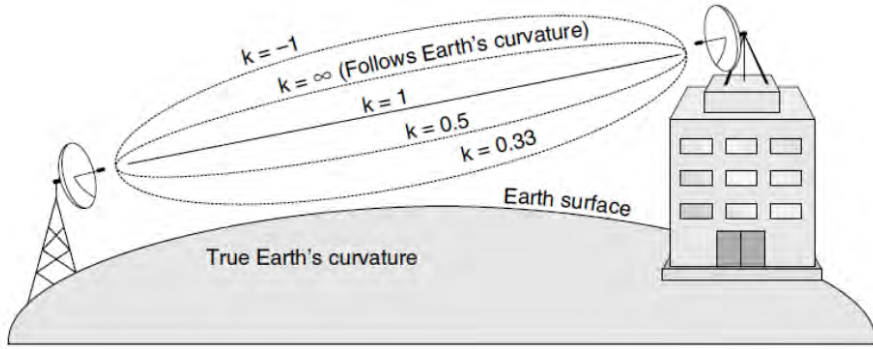


Figure 2.1: Variation of the ray curvature at different values of k [1]

can be found from the relationship [23]:

$$\frac{1}{r} = \frac{1}{r_o} + \frac{dn}{dh} \quad (2.9)$$

Common radio links, which are described as LOS, incorrectly propose that effective communications are restricted by optical horizon (i.e., $k = 1$). In most circumstances radio links are not restricted to LOS communication. Communications further than the optical horizon can often be realized by some 15 % (i.e., $k = 1.33$). Figure 2.2 shows this concept [2]. If we combine (2.8) and (2.9), then we can see that the k -factor is related to

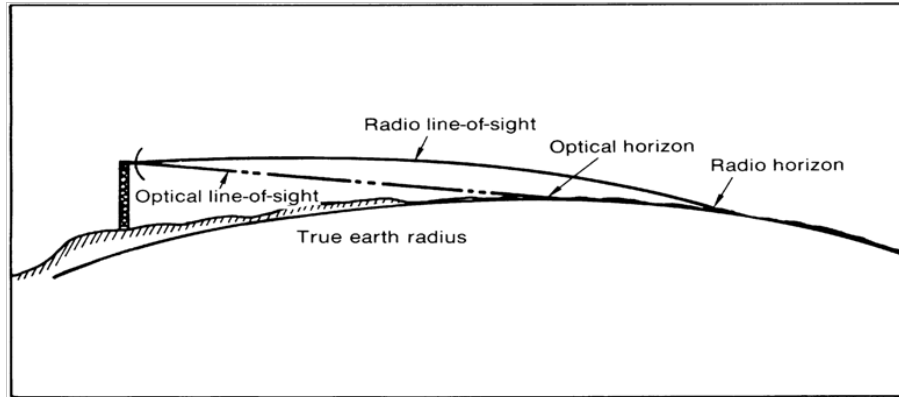


Figure 2.2: Optical LOS versus radio LOS [2]

the refractive index gradient by:

$$k = \frac{1}{(1 + r_o \frac{dn}{dh})} \quad (2.10)$$

where $\frac{dn}{dh}$ is the refractive index gradient. From (2.4) and (2.5), we get

$$\frac{dn}{dh} = \frac{dN}{dh} \times 10^{-6} = 10^{-6}G \quad (2.11)$$

If we substitute for the value of r_o (6371 km) and (2.11) into (2.10), we get

$$\begin{aligned} k &= \frac{1}{(1 + 0.006371G)} \\ &= \frac{157}{157 + G} \end{aligned} \tag{2.12}$$

The above equation shows the relationship between k-factor and refractivity gradient.

2.2.4 Standard Propagation Mechanisms

These are mechanisms that occur in the presence of a standard atmosphere i.e., when the refractivity gradient is characterized by -39 N-units/km (or $k = 4/3$). These propagation mechanisms include: free-space propagation, reflection, diffraction, scattering and tropospheric scatter [1, 24].

Free-space Propagation

In free space, the assumption is that the Earth's atmosphere has no effect on the radio wave. The transmission medium properties are assumed to be isotropic, homogeneous and loss-free [1]. It is characterized by increasing surface area of a sphere centred on the transmit antenna and radiating outwards. For this reason it is also known as *spherical spreading*. The field strength at any point is proportional to the inverse of square of the distance separating the transmit antenna and the receive antenna. The loss due to this mechanism is known as free-space path loss [24].

Reflection

When an electromagnetic radio wave strikes a smooth, large surface (larger than its wavelength), some or all of the energy is reflected from the surface and continues to propagate along a new path defined by the angle of reflection. The incident ray and the reflected ray makes equal grazing angle with the reflecting body and the strength of the reflected ray is influenced by the reflection coefficient [1]. This reflection coefficient is depended on the electrical properties of the reflecting medium, especially, the relative permittivity and the conductivity. The strength of the reflected ray depends also on the frequency, polarization, angle of incidence and the reflecting surface roughness [1, 24]. These reflected rays can add constructively or destructively with the direct ray at the receive antenna causing multipath propagation.

Diffraction

Diffraction arises when the radio wave propagating between the transmitter and the receiver meets an obstruction body which is impenetrable. The energy tends to follow

the curved surface of the obstructing object and allows propagation beyond the line of sight. It is characterized by exponential loss of energy with increasing distance (linear increase of propagation loss in dB with distance) [1, 24]. Diffraction occurs when the refractivity gradient is positive (low k -factor values). Beyond the horizon propagation is made possible due to Huygen's Principle explained later in Section 2.4.2 and also by ducting i.e when superractivity condition exists in the atmosphere [1, 25].

Scattering

This phenomenon occurs when the propagating radio wave meets objects in the transmission medium equal or smaller than its wavelength. This causes the radio wave to be reflected in different directions. As the frequency increases, the wavelength becomes shorter, and the reflecting objects seem rougher resulting in diffused reflections. Small imperfections in the atmosphere as a result of inhomogeneous refractive structure, also causes the energy to scatter. This mechanism is called tropo-scatter and is very useful in communications where high power transmitters and high gain transmitter and receiver antenna can be used to reduce attenuation due to this mechanism, more so in satellite systems [1, 24].

2.2.5 Anomalous Propagation Mechanisms

Anomalous propagation takes place when the refractivity gradient varies from that of the standard atmosphere leading to conditions such as sub-refractive, super-refractive and ducting (trapping) phenomena.

Sub-refractivity

This is when the atmosphere is such that the refractivity increases with height, resulting in refractivity gradient that is more positive than the standard refractivity gradient. The radio wave bends upwards away from the Earth. This tends to shorten the radio horizon [1].

Super-refractivity

For super-refractive gradients (between -157 and -79 N/km), the radio wave deflects downwards but with a rate less than the Earth's curvature but at a rate more than that of standard atmosphere. The degree of bending is influenced by the strength of super-refractive condition. Since the radius of the ray is less than the Earth's curvature, the ray leaving the antenna at small angles of elevation will experience total internal reflection in the atmosphere and will bounce back to the earth at some distance from the transmitter. On reaching the Earth's surface and being refracted from it, the waves can hop large distances thereby giving abnormally large ranges outside the LOS due to numerous reflections.

Due to these numerous reflections, the signal reaching the receiving antenna can add constructively or destructively thereby increasing and decreasing the signal strength respectively depending on the time delay and phase of the signals [25]. The condition is normally associated with abnormal temperature and humidity variation near the surface of the Earth. When temperature increases with height (temperature inversion) and/or the water vapour decreases with height, the refractivity gradient becomes more negative than that of the standard atmosphere [1]. The refractivity gradient can become more negative until a *critical gradient* is reached at which two radii of curvature are equal. here the radio wave will propagate at a constant height above the ground and will travel parallel to the Earth's surface [1].

Trapping (Ducting)

When the gradient continues to be more negative than that of the critical gradient, the radius of the ray curvature will become smaller than that of the Earth. This refractive condition is called as trapping or ducting because the radio wave is confined in a narrow region of the troposphere. A more convenient modified refractivity M is normally used for describing ducting profiles. Trapping tends to extend the radio horizon. The modified refractivity M defined by

$$M = N + 0.157h \quad (2.13)$$

where h (m) is the elevation. Negative gradient of M indicates presence of ducting and is used in classifying ducting gradients [26]. Radio waves can be trapped between trapping layer and the earth's surface (Figure 2.3) or the radio wave can be trapped between two trapping layers as shown in Figure 2.4.

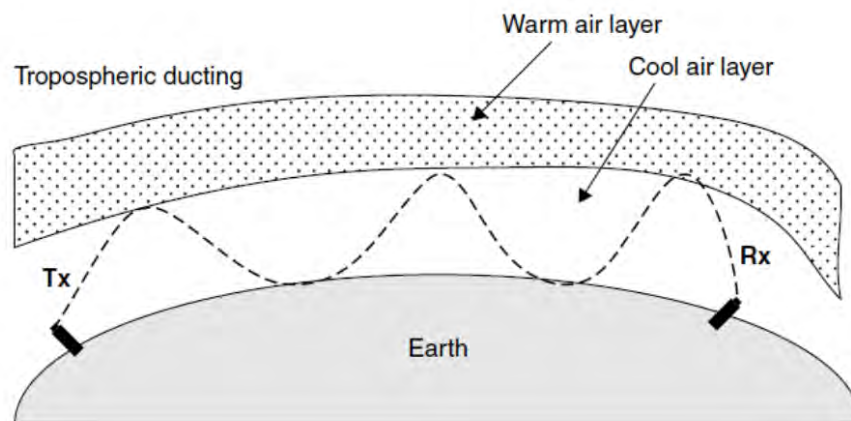


Figure 2.3: Ducting conditions with radio waves trapped between trapping layer and Earth's surface [1]

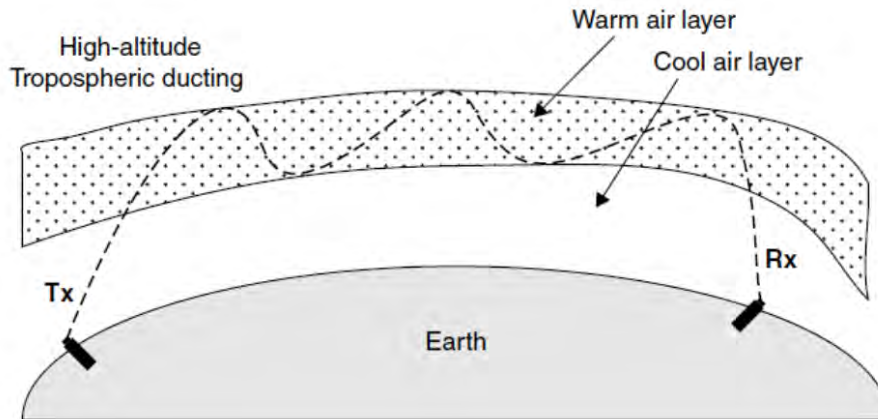


Figure 2.4: Ducting conditions with radio waves trapped between two trapping layers [1]

Ducts may be created by various meteorological conditions giving rise to either surface-based ducts, or elevated ducts, or evaporation ducts [1].

Surface-based ducts: If the conditions are such that ducting layer is formed at the Earth's surface, a surface-based duct is formed. Surface-based ducts occur when the value of modified refractivity at the top of trapping layer is lower than the value at the Earth's surface. Their effects are not sensitive to frequency and they provide for over the horizon communications or detection ranges of frequencies exceeding around 100 MHz [24].

Elevated Ducts: Elevated ducts are created in a similar way to surface-based ducts. Here the radio wave is repeatedly bent downwards by the trapping layer and then bent upwards by one or more refractive layers below the trapping layer. The thickness of these ducts varies from zero to few hundreds of meters, and the frequencies as low as 100 MHz are affected. Propagation effects include enhanced signals near or in the elevated ducts, and at times there can be absence of radio wave above the ducts [24].

Evaporation Ducts: Evaporation ducts are virtually everywhere above the oceans and above large water bodies. It is created by rapid decrease in water vapour content with height near the water's surface. Normally, the air nearby to the water bodies is saturated with water vapour due to evaporation. Therefore, the relative humidity near the surface is close to 100 %, and decreases rapidly with altitude till ambient condition is achieved, and is influenced the prevailing climatic conditions. This drop in relative humidity with height causes formation of a trapping layer. The height at which the minimum value of modified refractivity M is reached defines the duct height and is a measure of the duct strength. These heights normally vary between zero and forty meters. The propagation effects of evaporation ducts include extending the ranges in surface to surface radio systems and radar communications. They are known to be leaky to frequencies beyond 3 GHz [24].

It should be noted that equatorial regions are more vulnerable to formation of ducts. The probability of formation of ducts in temperate regions is low and that the probability of duct formation follows seasonal variation. Techniques for alleviating/combating other types of fading like increased fade margin and other diversity techniques have little or no

influence on combating blackout fading as a result of trapping layers [1].

2.3 Other Atmospheric Effects

There are other atmospheric attenuation which are not dealt with in this study. Atmospheric gaseous absorption especially water vapour and oxygen should not be confused with refractive and rain effects. Their effects like refraction also vary with altitude, location and path slant angle. Their attenuation contribution can be given by [12]:

$$A = \Upsilon_a d \quad (2.14)$$

where A is the attenuation in dB, d is the path length in kilometres and Υ_a is the atmospheric specific attenuation in dB/km. The atmospheric specific attenuation given is the sum of both due to water vapour and oxygen i.e., [12]:

$$\Upsilon_a = \Upsilon_o + \Upsilon_w \quad (2.15)$$

where Υ_w and Υ_o are specific attenuation due to water vapour and oxygen respectively. Fog and clouds attenuation is given by [12]:

$$\Upsilon_c = K_l M \quad (2.16)$$

where Υ_c (dB/km) and K_l (dB/km)/(g/m³) are the specific attenuation and the specific attenuation coefficient of the cloud respectively, and M (g/m³) is the liquid water density of the cloud. The last atmospheric effect that we will mention is due to rain, and modelling of its attenuation effect on communication links is detailed in [7] and dominates more at frequencies above 10 GHz.

2.4 Link design

It is important to design a communication system for the proposed location and to estimate, with relative confidence, the system performance prior to fabrication and deployment. Poor planning may lead to over-design and hence wasted resources or under-design leading to reduced system performance. It is therefore, imperative to know beforehand the factors influencing the performance of each individual link. These parameters include received signal strength, noise, and further channel losses separately from attenuation, such as interference or multipath. The design of such a link entails mainly four iteration steps: initial planning and site selection, drawing of a path profile, path analysis and lastly, site survey [2].

2.4.1 Initial Planning and Site Selection

Microwave LOS link may comprise of a single or several hops. In the initial planning stage, we need to know the need of the proposed link i.e., whether it is for private communication link, an addition to existing link or it is part of a telecommunication grid as a support route or as an extension of the support. The interest of a communication link is to provide a channel for point A and B on the earth's surface. Point A and B may be short, needing a single link or long, requiring many links. At this stage there is need to ascertain that there is available land with access for site construction and no construction restrictions i.e. airport or military restrictions.

Accurate topographic maps are used for route selection to avoid "difficult" paths; which are likely to be prone to multipath fading due to anomalous propagation mechanisms. These maps are also used in drawing up the path profile explained in the next subsection. The likelihood of the link being in the coastal regions, or reflective deserts or over large water bodies need to be known before hand. The LOS design engineers must also verify that the proposed link will be compatible with the existing communication systems. Frequency planning and interference issues are also dealt with at this stage [2].

2.4.2 Path Profile

Path profile is defined as a geographical representation in two dimensions of the path followed by the radio beam between the two ends of a link. Path profiles help in determining the height and location of the transmitting and receiving antennas at each of the links. It insures that the link is free from obstacles, and is not exposed to transmission losses from radio phenomena such as multipath reflections. Obstructions along a path may block the radio waves partially or wholly resulting in diffraction fading/loss. It should be noted that end points of a link should have unbarred radio line of sight. However, this at times is not practically possible and it has been proven that if 60 % of the path is clear of obstruction, then, the effect of the earth can be ignored and the path loss can be approximated by the free-space loss [3].

Radio line of sight needs more clearance than optical line of sight to satisfy for the microwave signal characteristics [2]. In order to guarantee that loss due to obstructions in the line is reasonably small under all probable values of k-factor variations, it is necessary that a path profile be drawn that shows the antenna heights and terrain heights adjusted to account for the k-factor variation. The particular area that has the least clearance from a direct ray drawn between the two antennas is called the dominant obstacle.

To estimate the extent of clearance needed for this condition, we apply the theory of Fresnel zones. It is based on introducing an infinitely thin screen into the direct path of an electromagnetic wave-front and analysing the bending around the screen. According to Huygen's principle (illustrated in Fig. 2.5), a wave-front can be well-thought-out as an infinite secondary wavelets radiating energy in in a similar way as the primary source, thus

generating a secondary wave-front [3]. The received field strength at the receiving antenna

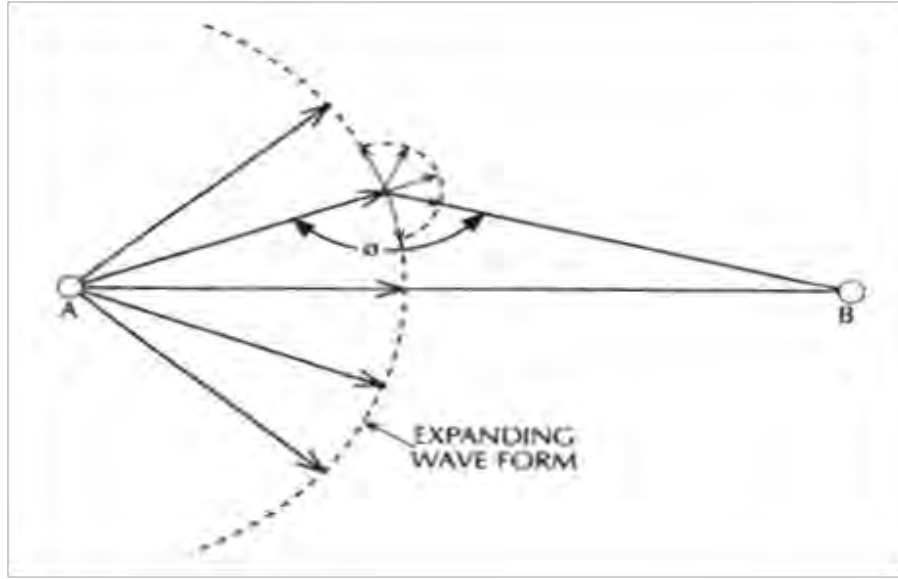


Figure 2.5: Huygen's principle [3]

is thus, the summation of infinite number of tiny wavelets produced by the transmit antenna. Elements off the main axis of the microwave beam, forming the direct path between the two antenna apertures, thus contribute to the overall received field; if they are blocked, the receive field strength will be affected. The phase delays of these off-axis components also affect the received signal.

Under free-space propagation, this complex arrangement results in the normal condition of the field strength decreasing with the square of the distance from the transmitting antenna. However, if a screen is introduced that blocks off some portion of the wave front, the pattern results in areas of minima and maxima as the screen blocks more and more of the wave-front. This is seen visually in optics where a screen with a hole in it blocks a light source, resulting in a diffraction pattern of light and dark concentric circles. The boundary points are where the path difference between the direct ray and a ray from a secondary wavelet is multiples of half-wavelengths. According to the theory of Fresnel zones, these points are defined by a series of ellipsoids with two antennas at the loci. This is shown in Figure 2.6.

The earth curvature for a certain hindrance point is estimated by (2.16), where h is in metres [2]:

$$h = \frac{d_1 d_2}{12.75k} \quad (2.17)$$

The Fresnel zone clearance maybe estimated by (2.17), where R_1 is the first Fresnel radius in metres, d_1 (m) and d_2 (m) are the distances of the obstacles from transmitting and receiving antennas respectively and F is the frequency in GHz [2]:

$$R_1 = 17.3 \sqrt{\frac{d_1 d_2}{(d_1 + d_2)F}} \quad (2.18)$$

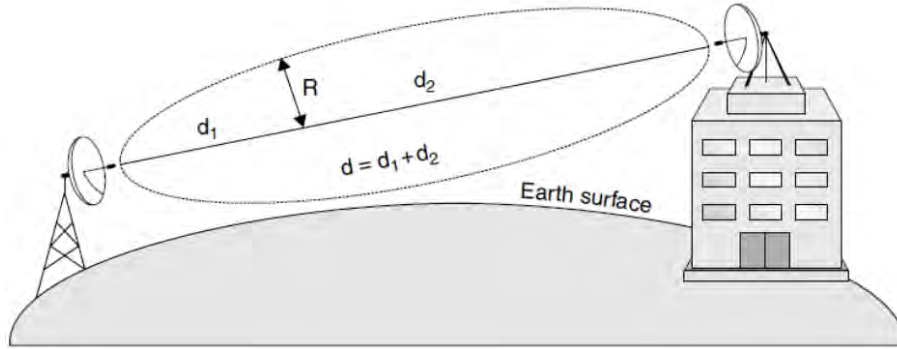


Figure 2.6: First Fresnel Zone Radius [1]

2.4.3 Free Space Path Loss

In line of sight radio systems, losses are mainly due to free-space path loss. As the electromagnetic wave propagates between two geometrically separate points, its energy strength reduces with distance even if the path is clear of obstacles [1]. This attenuation is directly proportional to the square of distance and frequency. This loss is ever present in any communication link and its effect must always be taken into account during LOS designs. This loss can be modelled by Friis free space path loss model given by [1]:

$$L_{FSL} = \left(\frac{4\pi d}{\lambda}\right)^2 \quad dB \quad (2.19)$$

where d in meters is the distance between transmitting antenna and receiving antenna and λ in meters is the operating wavelength .

This free-space loss between two isotropic antennas is derived from the total output power from a transmitter and the received power at the receiver and can be expressed in decibels as in equation 2.19. Frequency and distance are in GHz and km respectively [1]:

$$L_{FSL} = 92.45 + 20 \log(d_{km}) + 20 \log(f_{GHz}) \quad dB \quad (2.20)$$

2.4.4 Link Budget

A microwave terrestrial LOS link designer starts the design process by performing a link budget analysis. This entails a calculation involving the gains of antennas and path losses. The path losses here include the free space loss, path losses due to atmospheric effects including multipath and miscellaneous losses due to couplings at the receiver and transmitters. This is used to estimate the maximum distance of the link for successful operation [1]. These losses are normally calculated in decibels so that all elements become terms to be added and subtracted. The analysis must take into consideration the effective isotropic radiated power (EIRP) from the transmitter and all the losses just before the

receiver. At the receiver, the designer needs to also consider receiver sensitivity. Below the receiver threshold noise level, no signal can be recovered. Therefore, the designer must be able to cater for this receiver noise level for satisfactory performance to be achieved [12].

2.4.5 Fade Margin and Link Availability

Fade margin, also called link margin is a measure of how much margin is available in the communications link between the functional point and the point where the link can no longer be available. It is gotten by relating the received signal to the receiver sensitivity [12]. The link margin is related to the outage probability, since below the receiver sensitivity, there is outage hence no availability.

$$\text{Link margin} = \text{Received power} - \text{Receiver sensitivity} \quad (2.21)$$

The received power is generally influenced by the characteristics of the transmission medium. In a wireless medium, multipath fading plays a major role. When the reflected ray reaches the receiver at the same time as the directed ray, then, they can either add destructively or constructively resulting in signal attenuation and signal enhancement respectively [1,12]. Multipath fading normally gives rise to short-term outages, hence, has the highest impact on error performance. Multipath fading gives rise to two kinds of signal degradation: frequency selective and flat fading. Flat fading is as a result of thermal noise and interference [1].

Link paths that are prone to multipath should be avoided. Multipath is more prone near coastal regions, over-water surfaces and in flat terrain like the reflective deserts. One way of improving on received power is to increase the transmit power, but even this has a limit not to cause interference to other adjacent channels. The transceiver designer's aim is to close the link for the stated distance and needed availability as efficiently as probable, while the link designer's aim is to use the existing transceiver to fulfil a specific communication prerequisite. Thus, there is always a trade-off between distance and availability for the link [1].

2.4.6 Site Survey

Once the path profile has been completed, the designer should verify the results by a field survey of the sites at each end of the path and the intervening terrain. Of primary importance is verification of site locations and conditions that, indeed, the terrestrial LOS criteria developed on the profile have been met [12]. The designer should particularly be watchful of new structures that have been built since the preparation of the topographic maps used to construct the profile. The topographic maps may also contain errors and the site survey will confirm the details as shown in these maps [12].

2.5 Chapter Conclusion

In this chapter, we have analysed the effects of atmosphere on electromagnetic radio waves propagating in the lower troposphere. The bending of radio waves is mainly dependent on the atmosphere refractive index variation in the lowest part of the atmosphere. The refractive index variation is small and a more convenient parameter, refractivity is used. Refractivity is a function of temperature, relative humidity, and pressure, which of themselves vary with space and time. Knowledge on their effects on radio wave allows a more accurate design of LOS links. The chapter also gives an outline of microwave link design and the parameters that are key to its performance and availability.

Chapter 3

Multipath Fading Predictions and Interpolation Techniques

3.1 Introduction

A main concern for microwave system customers is how frequently and for what duration a system might be out of service. Several numerical models and analysis techniques have been established to forecast and quantify the outage and availability over a period of time. Performance forecasting largely depends on the assessment of two main propagation mechanisms: multipath fading and/or attenuation due to rain. Multipath fading modelling prediction methods have been derived that estimate the probability of outage at a single frequency. In this chapter we discuss some of these techniques. A review of recent work on radioclimatological studies in Southern Africa is also briefly outlined. Lastly, three spatial techniques (Kriging, Thin-plate spline and Inverse distance weighting) used in extending or estimating un-observed variables at a position or location using observed variables at known position or locations are discussed.

3.2 Multipath Fading Predictions

Clear air fading phenomena due to extreme refractive layers in the troposphere consist of beam spreading, antenna decoupling, surface multipath and atmospheric multipath [7]. Multipath fading is due to changes in the atmosphere which are of themselves random, hence, the prediction of fading occurrence and/or distribution can only be described by statistical methods. ITU-R [7] provides techniques for estimating the proportion of time that a fade depth is surpassed in the average year. It further recommends prediction approaches based on specific climatic and geographical environments. Region-based techniques for deep fading predictions have been available for a number of countries for several years. They include the Barnett-Vigants model for the United States of America, and the Morita model for Japan, among others [6, 27, 28].

These techniques for forecasting the proportion of time that a certain fade depth is exceeded are a function of frequency, path distance and geoclimatic factor, with the ITU-R method having an additional variable of path inclination. The ITU-R suggests that region-based methods are likely to be more accurate than the ITU-R technique in these estimations because of the effect of the geoclimatic factor. They further recommend that

in determining the geoclimatic factor, fading data in the region of interest should be used in the estimation. However, where fading data is not available, it provides a procedure of estimating the geoclimatic factor K based on refractivity gradients in the region of interest [7]. We begin our discussion with the regional techniques before outlining the origin and current version of the global technique. Their performances are compared in the next chapter.

3.2.1 Morita Method

Morita and Kakita developed their probability of occurrence of fade based on power-law. They were able to show the effect of path distance on the number of hours comprising deep fading based on 4 GHz microwave links in Japan. The probability of fade occurrence (P_R) is given by [29]:

$$P_R = Kd^\alpha \quad (3.1)$$

where K and α are constants, and d is the path length in kilometres. They fixed the number of measured hours with deep fading but did not show plainly how the measured time related with fade depth. Morita later added reliance on frequency, f , by analysing new data for various frequencies. He was able to fit the distance, d , dependency first and later frequency reliance by carrying out partial regression analysis. He also presented geoclimatic variability by proving factors for three regions namely: plains, coastal and mountainous regions [29]. The new empirical formula for P_R was then given by [27]:

$$P_R = 100Kd^{3.5}f^{1.2} \times 10^{-A/10} \quad (3.2)$$

where d and f are as defined earlier, A is the fade depth in dB and K for different regions is given as follows [27]:

$$K = \begin{cases} \frac{9.9 \times 10^{-6}}{\sqrt{h_1+h_2}} & \text{for coastal regions} \\ 10^{-7} & \text{for plain regions} \\ 3.9 \times 10^{-8} & \text{for mountainous regions} \end{cases} \quad (3.3)$$

where h_1 and h_2 are respectively the transmit and receive antenna heights above the sea level, and give the average path height in meters.

3.2.2 Barnett-Vigants Method

According to Barnett [30], multipath propagation creates a major constraint to the microwave radio systems' performance. Frequency and/or space diversity must be employed to provide satisfactory commercial operation. He ascertained that probability of deep multipath fading is linear with frequency, cubic in path length and varies with meteorological-geographical factors. He analysed multipath fading data in Ohio (USA) and provided statistics for the total time of fade, the number of fades, their average duration,

and the fade duration distribution as a function of fade depth. He realized that the intensity of multipath fading varies greatly, even during normally active summer months; in some days there would be extensive multipath fading while on others, there would be none [30]. He was able to compute the probability for multipath fading distribution as given by [30]:

$$r = c\left(\frac{f}{4}\right)(D^3)(10^{-5}) \quad (3.4)$$

where r is the multipath occurrence factor,

D (miles) is the path length ,

f (GHz) is the frequency and,

c is the terrain factor given by [30]:

$$c = \begin{cases} 1 & \text{average terrain} \\ 4 & \text{over-water and gulf coast} \\ 0.25 & \text{mountains and dry climate} \end{cases} \quad (3.5)$$

He asserted that the time (probability) distribution of the envelope of a microwave signal subject to multipath fading depends upon the path length, path geometry, terrain clearance, type of terrain, and meteorological conditions in a complex manner. However, an estimate of the fade depth distribution can be made for the typical microwave paths for heavy fading time of the year i.e. the so called worst month fading [30]. The estimate of r indicates that a for path of above-average length, maintenance of the per-hop fading outage requires compensation for the additional free space loss ($\propto D^2$) and for increases of multipath ($\propto D^3$), which combines to impose a D^5 (15 dB/octave) length dependence [30].

Vigants modified c in Barnett's model to cater for a terrain roughness parameter quantifying common knowledge that paths over irregular terrain faded less than those paths over fairly flat landscape, presumably since unwavering atmospheric layer forming is less possible to take place over irregular landscape [31]. Again, flat terrain/landscape is prone to multipath fading. Smooth surfaces increase the probability of multipath propagation due to multiple reflections. Terrain irregularity is estimated from terrain elevations above reference level gotten from the path profile at one mile (1.6 km) intervals, with the ends of the paths omitted. Modified for roughness, c becomes [31]:

$$c = \begin{cases} 2(w/50)^{-1.3} & \text{average terrain} \\ (w/50)^{-1.3} & \text{over-water and gulf coast} \\ 0.25(w/50)^{-1.3} & \text{mountains and dry climate} \end{cases} \quad (3.6)$$

where w is terrain roughness factor. Appropriate values of w vary from 20 feet (6 m) (flat) to 140 feet (43 m) (irregular); values of 20 feet (6 m) and 140 feet (43 m) should be used when estimated values of w are less than 20 feet (6 m) or larger than 140 feet (43 m), roughness of 50 feet (15 m) has been defined as normal [31]. The modified Barnett-Vigants

model can then be conveniently expressed as [32, 33]:

$$P_w = 6.10^{-7} c f d^{3.0} 10^{-A/10} \times 100 \quad (3.7)$$

where c is as defined earlier but given as in Figure A.1 and A.2 in the Appendix A of [33]. Barnett-Vigants model was developed from fading data of a 11 GHz relay of 28.5 miles (46 km). It was further noted to perform fairly well for both 4 GHz and 6 GHz relays with path lengths of up to 20 - 40 miles (32 - 64 km). Beyond these parameters the model does not hold [31, 34].

3.2.3 ITU-R Methods

Olsen and Tjelta [6], in the cited paper have detailed the origin/background of ITU-R P530 methods for predicting the likelihood that a certain fade depth is exceeded in the average year. They explained that the ITU-R P530 models as they are in their current version originated from that of International Radio Consultative Committee (CCIR) for Northwest Europe [6]. A summary of this is given here and the reader is referred to [6] for more details.

The ITU-R provides two techniques for multipath fading distribution predictions. Method 1 for estimating deep fading comprises three link variables: frequency, path length and the magnitude of path inclination. Method 2 comprises the three link variables in method 1 plus an additional variable, average grazing angle. In both techniques, there is an additional variable caters for the variability of climate and terrain, the geoclimatic factor K . Method 1 in its original version is expressed as [6]:

$$p = K d^{3.6} f^{0.89} (1 + |\varepsilon_p|)^{-1.4} \times 10^{-A/10} \quad (\%) \quad (3.8)$$

where p is the probability that a certain fade depth A (dB) is exceeded in the worst month of the average year, d (km) is the path distance, f (GHz) is the operating frequency and, ε_p is the path inclination with its magnitude given by [6]:

$$|\varepsilon_p| = \frac{|h_e - h_r|}{d} \quad (3.9)$$

where h_e (m) and h_r (m) are transmit and receive antenna elevations above the sea level and d is as defined earlier. The fade depth A in dB can be obtained from [6]:

$$A = G - 57 + 36 \log d + 8.9 \log f - 14 \log(1 + \varepsilon_p) - 10 \log p \quad (dB) \quad (3.10)$$

where G is the logarithmic geoclimatic factor and the geoclimatic factor K can be obtained from [6]:

$$G = 10 \log K + 57 \quad (dB) \quad (3.11)$$

The second method in its original version is given by [6]:

$$p = Kd^{3.3}f^{0.93}(1 + |\varepsilon_p|)^{-1.1}\phi^{-1.2}.10^{-A/10} \quad (\%) \quad (3.12)$$

where all variables are as defined earlier, with additional average grazing angle ϕ (mrad) is the angle between the ray beam and the surface. The fade depth A exceeded in the average year is given by [6]:

$$A = G - 46 + 33 \log d + 9.3 \log f - 11 \log(1 + |\varepsilon_p|) - 12 \log \phi - 10 \log p \quad (dB) \quad (3.13)$$

where G is also as defined earlier and the geoclimatic factor K is given by [6]:

$$G = 10 \log K + 46 \quad (dB) \quad (3.14)$$

The average grazing angle can be obtained as detailed in [6]. From the steps outlined above, the geoclimatic factor K is determined from fading data in the reverse order, i.e., after obtaining the probability of time that a certain fade depth A is exceeded, we find the logarithm of the expression of outage probability and end up with the geoclimatic factor K . Nevertheless, since in most cases adequate fading data is unavailable, the estimation of the geoclimatic factor K is based on the statistics of the refractivity gradient profiles [6, 7]. The prediction for the geoclimatic factor K in the above methods can be obtained from [6]:

$$K = 10^{-C_o}p_L^{1.5} \quad (3.15)$$

where C_o is the coefficient for the various types of link given in Table 3.1 and, p_L is the proportion of time that the refractivity gradient in the lowest 100 m is more negative than -100 N units/km. The values of p_L can be found in [22] and its earlier version. The values are for February, May, August and November to cater for the four seasons in a given year. [6], gives detailed analysis on how the expression for the geoclimatic factor above came about and is not of interest of this study. In the revised versions of Method

Table 3.1: Coefficient C_o values for various types of link in(3.15) [6]

Type of Link	Method 1	Method 2
Overland links not in mountainous regions	6.5	5.4
Overland links in mountainous regions	7.1	6.0
Overland links	6.0	4.9

1 and 2, the geoclimatic factor is estimated from [6]:

$$K = 10^{-C_o+0.1(C_{Lat}+C_{Lon})}p_L^{1.5} \quad (3.16)$$

C_o and p_L are as defined earlier, C_{Lat} and C_{Lon} are the latitude and longitude coefficients respectively. The coefficient values C_o of is as given in Table 3.3 and the coefficients values of C_{Lat} and C_{Lon} are as given in Table 3.2.

Table 3.2: Variuos value of both latitude and longitude coefficients [6, 7]

	Coefficient value (dB)	Continental latitude/longitude
C_{Lat}	0	for $\xi \leq 53^\circ\text{N}$ or S
	$-53 + \xi$	for 53°N or S $< \xi < 60^\circ\text{N}$ or S
	7	for $\xi \geq 60^\circ\text{N}$ or S
C_{Lon}	3	for longitudes of Europe and Africa
	-3	for longitudes of North and south America
	0	for all other longitudes

Table 3.3: Coefficient C_o values for various types of link in(3.16) [6]

Types of Links	Method 1	Method 2
Overland links with lower antenna heights < 700 m above sea level	6.5	5.4
Overland links with lower antenna heights > 700 m above sea level	7.1	6.0
Links over medium-sized bodies of water, coastal areas near such water bodies or regions of many lakes	5.9	4.8
Links over large water bodies, or coastal regions near such water bodies	5.5	4.4

The Study Group 3 of ITU has continued to revise the ITU-R P530 models since the first version of 1978 [35]. We will highlight the differences in the recent versions with regard to estimation/prediction of the geoclimatic factor and the probability of time that a certain fade depth is exceeded in the average year. In [36], version ITU-R P530-8, the geoclimatic factor K is given by [36]:

$$K = 5.010^{-7} \times 10^{-0.1(C_o + C_{Lat} + C_{Lon})} p_L^{1.5} \quad (3.17)$$

and the proportion of time that a certain fade depth is exceeded is given by (3.8). In ITU-R P530-9 [37], there is a great change in both the expressions of the geoclimatic factor K and the probability of fade depth exceeded. Again, two methods are introduced; for detailed planning and for quick planning applications. For detailed planning applications, the value of K can be estimated from [37]:

$$K = 10^{-3.9 - 0.003 * dN_1} S_a^{-0.42} \quad (3.18)$$

where dN_1 is the point refractivity gradient in the lowest 65 m of the atmosphere not exceeded for 1 % of an average year and, S_a is the terrain roughness factor. S_a can be defined as the standard deviation of terrain heights (m) within $110 \text{ km} \times 110 \text{ km}$ area with a 30 s resolution [36]. The p_w , probability of time a certain fade depth A is exceeded is given by [37]:

$$p_w = K d^{3.2} (1 + |\varepsilon_p|)^{-0.97} \times 10^{0.032 * f - 0.00085 * h_L - A/10} \quad (\%) \quad (3.19)$$

For quick planning use, the corresponding values of K and p_w can be estimated from

(3.20) and (3.21) respectively [37]:

$$K = 10^{-4.2-0.0029*dN_1} \quad (3.20)$$

$$p_w = Kd^{3.0}(1 + |\varepsilon_p|)^{-1.2} \times 10^{0.033*f-0.001*h_L-A/10} \quad (\%) \quad (3.21)$$

From versions ITU-R P.530-9, ITU-R P.530-10, ITU-R P.530-11 and ITU-R P.530-12, the expression for the geoclimatic factor and the worst month probability of unavailability remains unchanged. However, from version ITU-R P.530-12 to ITU-R P.530-13, there is a drastic change in the estimation of these two parameters. There is no change again in expressions of these values from version ITU-R P.530-13 and ITU-R P.530-14. For detailed planning, the geoclimatic factor and probability of unavailability in the worst month is given by [7, 38]:

$$K = 10^{-4.4-0.0027*dN_1}(10 + S_a)^{-0.46} \quad (3.22)$$

$$p_w = Kd^{3.4}(1 + |\varepsilon_p|)^{-1.03} f^{0.8} \times 10^{-0.0007*6h_L-A/10} \quad (\%) \quad (3.23)$$

For quick planning applications the expressions are given as [7, 38]:

$$K = 10^{-4.6-0.0027*dN_1} \quad (3.24)$$

$$p_w = Kd^{3.1}(1 + |\varepsilon_p|)^{-1.29} f^{0.8} \times 10^{-0.00089*h_L-A/10} \quad (\%) \quad (3.25)$$

It should be noted that in all these expressions for predicting the probability that a certain fade depth is exceeded in the worst month of an average year, the magnitude of ε_p is as given earlier in (3.9). Equations (3.23) and (3.25), and the associated equations (4) and (5) for the geoclimatic factor K , were derived from multiple regressions on fading data for 251 links in various geoclimatic regions of the world with path lengths d in the range of 7.5 to 185 km, frequencies f in the range of 450 MHz to 37 GHz, path inclinations $|\varepsilon_p|$ up to 37 mrad, lower antenna altitudes h_L in the range of 17 to 2 300 m, refractivity gradients dN_1 in the range of -860 to -150 N-unit/km, and area surface roughnesses S_a in the range of 6 to 850 m. Equations (3.23) and (3.25) are also expected to be valid for frequencies to at least 45 GHz [7].

3.3 Recent Clear-air Radioclimatological Studies in South Africa

In this section, we briefly outline the recent studies on clear air radioclimatological work. It has been done mainly by two groups; one group was based in University of KwaZulu-Natal, Durban and the other in the University of Pretoria. Their main focus has been

on determination of distribution of k -factor in the region. This factor (k -factor) is useful in determining the heights of transmitting and receiving antennas to provide for path clearance in LOS links. This is to avoid diffraction loss due to diffraction fading, also known as k -factor fading.

3.3.1 Odedina and Afullo

Afullo and Odedina have modelled the effective Earth radius factor for Southern Africa by considering radioclimatological data for Maun, Botswana and Durban, South Africa. They presented two models for determining the probability density function (PDF) of the effective Earth radius factor as a means of predicting the k -factor variation [14, 39, 40]. The first model is a curve fitting one based on the bell-shaped variation of the plotted k -factor. Here they compared the measured PDF and the modelled prediction to obtain the best approximation by use of integral of square error (ISE) method. The second model used the kernel estimate for the pdf with a focus of biweight kernel, triangular kernel and the Gaussian kernel. They compared the kernels using ISE criterion and observed that biweight kernel gives the best estimate [14, 40].

In their approach in determining the k -factor, they related the radius of curvature of the ray, and the variation of refractivity, N , with height, h . If v is the velocity of wave propagation, then [14]:

$$\frac{dv}{dh} = \frac{v}{\rho} \quad (3.26)$$

where h is the height above ground level. Given ϵ_r , the relative permittivity of the troposphere at a height h , ρ can be estimated by [35, 40]:

$$\rho = \frac{v}{dv/dh} = \frac{-2\epsilon_r}{d\epsilon_r/dh} \approx \frac{-2}{d\epsilon_r/dh} \quad (3.27)$$

The relative permittivity ϵ_r is also related to refractivity with the following equation:

$$n = \sqrt{\epsilon_r}; \quad N = (n - 1) \times 10^6 \quad (3.28)$$

The radius of the curvature of the path is a function of the change in dielectric constant with elevations and exhibits hourly, daily and seasonal variation [14, 39, 40]. The k -factor is estimated from [40]:

$$k = \frac{1}{1 - a/\rho} = \left[\frac{1}{1 + a \frac{d\epsilon_r/dh}{2}} \right] \quad (3.29)$$

where a is the actual radius of the earth, then the effective earth radius is given by:

$$\rho = \left[\frac{a}{1 - 0.04665e^{0.005577*N_s}} \right] \quad (3.30)$$

where N_s is the surface refractivity. The sea-level refractivity, N_o , can be obtained from

a nearby weather bureau from which:

$$N_s = N_o e^{-0.1057 * h_s} \quad (3.31)$$

where h_s is the altitude above sea level (km) of the line-of-sight radio link. Equations (3.30) and (3.31) are used to determine k -factor as a function of height. Their results showed that k distribution is bell-shaped and the following approximate pdf was proposed:

$$f^*(k) = A e^{-\alpha(k-\mu_k)^2} \quad (3.32)$$

From which they applied curve fitting technique as described in [14, 39, 40] to come up with the best approximate model. They also used kernel estimation [40] to determine the best approximate model, estimate, from which they were able to ascertain that the kernel estimate gave better performance than the curve-fitting estimate [40].

In [41], Odedina and Afullo, used Digital Terrain Maps and link measurements to estimate the percentage/probability of time that a certain fade depth is exceeded in the average year. The modelling was done using the ITU-R method for both detailed link design and quick planning applications. They were able to confirm that the detailed link design method is more accurate than the quick planning method in estimation of fade depth exceeded. The link measurements used were obtained from a 6.73 km link set up between Westville Campus and Howard College Campus of the University of KwaZulu-Natal. They then developed analytical expressions/models for probability of exceedance for each of the months in the year in which link measurements were taken. They compared their results with the region-based models, i.e., Vigants and Morita models. Their findings are presented in [28].

3.3.2 Palmer and Barker

Palmer and Baker [42], proposed a model for estimating the average monthly cumulative distribution of the effective Earth radius factor for South Africa for eight locations where radiosonde sounding data had been collected. They were able to confirm that the k -factor consists of both dry and wet terms and the cumulative distribution can be represented by [42]:

$$\Psi_{eff}(k \geq k^c) = \Psi_{dry} \times \Psi_{wet} \quad (3.33)$$

where

$$\Psi_{dry} = \exp(-(k-1)^2)/(2\sigma_{dry}^2) \quad (3.34)$$

and

$$\Psi_{wet} = \exp(-(k-k_{ref})^2)/((2\sigma_{wet}^2)) \quad (3.35)$$

where σ_{dry} and σ_{wet} represent the variance of k in each of these terms. They further manipulated equations to develop a regression formula of the form:

$$\ln\sqrt{(1/\Psi)} = m_1 k + m_2 \text{Abs}(k - k_{ref}) + C \quad (3.36)$$

where m_1 , m_2 and C are regression coefficients.

This was found to compress the resultant values of k too much near to unity, causing substantial change in sensitivity of the method for these values. They resolved to resort to the basic form used originally in their earlier research, given by [43]:

$$\sqrt{\ln(1/\Psi)} = m_1k + m_2Abs(k - k_{ref}) + C \quad (3.37)$$

The regression analysis results showed only marginally worse from those of (3.36) but did preserve the wanted sensitivity for the values of the k -factor near to unity [42]. Their results showed that the model is only suitable for coastal plains from heights of a few hundred metres upwards. This was due to ocean climate effects at the coastal stations and they proposed for a further study to determine a more accurate model [42].

Palmer and Baker also used surface based measurements to estimate the long term yearly mean value of k -factor [44]. The effective earth radius factor can be expressed in terms of height derivative of $N, \Delta N / \Delta h$ as:

$$k = [1 + (\frac{\Delta N}{\Delta h})/50\pi]^{-1} \quad (3.38)$$

The refractivity gradient can be assumed to be linear in the first kilometre and an approximation of refractivity gradient as a variable of height is suggested in [44], and is given by:

$$(\frac{\Delta N}{\Delta h})/50\pi = a \times \{[\frac{h}{h_t}]^{2/3} - 1\} \quad (3.39)$$

where a is an invariant value of the normal refractivity gradient at sea level and the pseudo height of the tropo-pause in the above equation for linear model is given by:

$$h_t = \{ \frac{3}{2} - [\frac{X}{90}]^{\frac{2}{3}} \} \times 12 \text{ km} \quad (3.40)$$

where X is the geographical latitude of the observing station.

The model is referred to as the double elliptic model for the reason that of it has dependency on both the geographical latitude and the height above sea level. From this model Palmer and Baker were able to create contours of the average long-term refractivity gradient and k -factor for Southern Africa. However from the stations observed, Alexander Bay (located in the Northern Cape of South Africa) had a discrepancy between the measured and approximated value of the long-term k -factor and is worth exploring [44]. Palmer and Baker further suggested a double cumulative probability distribution model for estimating the probability that a particular value of the propagation k -factor will be exceeded [45]. The method is prolonged by a simple height regression analysis in order to estimate the cumulative performance of the k -factor at diverse ground level elevations in the summer rainfall area of South Africa during various months. The model provides an indication of high k -factor values in expressions of the occurrence probability [45].

3.4 Spatial Interpolation Techniques

Spatially continuous data or spatially continuous planes over a region of interest are needed by scientists to make acceptable analyses. However, such data are generally not obtainable and normally very difficult and costly to obtain. Additionally, environmental data collected from the field are usually in discrete form. Therefore, the values of an element at un-sampled locations/sites must be predicted to produce spatially continuous data. Spatial interpolation techniques make available tools for approximating the values of unobserved variable at un-sampled locations using data from discrete observables [46].

There is no single preferred method for data interpolation. Choice of method depends on actual data, level of accuracy required, the time and/or computer resources available, quality of secondary information, data variance, grid size or resolution and surface type [46, 47]. In this study, we describe three methods: kriging, thin-plate spline and inverse distance weighting. Techniques that create continuous surfaces consist of various methods that may consist of regression analyses and distance-based weighting averages. The difference amongst these methods is the measures used in choosing weight values in relation to distance [48].

3.4.1 Kriging

There are very many types of kriging, but here we discuss the so called *ordinary kriging*. Kriging uses linear summation of values at observable points to approximate values at un-observable points. It is popular because it is an exact interpolator i.e. the predictor for an input that has previously known matches the observed output. The predicted value Z_{po} is given by Eqn. (3.41) where Z_{oi} are the observable values and κ_i are the Kriging weights [49, 50]:

$$Z_{po} = \sum_i^N \kappa_i \cdot Z_{oi} \quad (3.41)$$

with the constraint that;

$$\sum_i^N \kappa_i = 1 \quad (3.42)$$

Kriging assumes that the nearer the input data are, the more they are related to their outputs. Kriging is modelled through a covariance procedure that is second-order stationary, which implies that the first two statistical moments (the means and the covariance) are constants [49, 51]. The weights are determined by imposing that the statistical error be zero i.e.

$$E(Z_{po} - Z_{tu}) = 0 \quad (3.43)$$

and minimum variance

$$E[(Z_{po} - Z_{tu})^2] = \textit{minimum} \quad (3.44)$$

where Z_{tu} is the true but unknown value.

Equation (3.44) is then substituted in the variance equation and minimized and solved by using Lagrange multiplier ν resulting in a linear system of $N + 1$ equations with $N + 1$ unknowns [50]:

$$\sum_i^N \kappa_i \omega(x_i, x_j) + \nu = \omega(x_i, x_o) \quad (3.45)$$

where $\omega(x_i, x_o)$ is the semi-variance between the unobserved and the observed data points, $\omega(x_i, x_j)$ is the semi-variance between the data points x_i and x_j and, κ_i is the kriging weighting.

$\omega(x_i, x_j)$ corresponds to a spatial correlation structure of the random field described by the semi-variogram [50]:

$$\omega(x_i, x_j) = \omega_{ij} = \frac{1}{2}(Z_x - Z_{x+h}) \quad (3.46)$$

where Z_x is the known value at position x and Z_{x+h} is the known value at another position within a distance h . The length of separation vector h is called lag distance. The semi-variogram offers valuable information for interpolation; determining spatial patterns, sampling density, and spatial simulation [51]. After obtaining the kriging weights κ_i , the kriging variance is given by [50]:

$$\sigma^2(x_o) = \sum_i^N \kappa_i \omega_{ij} + \nu(x_o) \quad (3.47)$$

Under the assumption of a local Gaussian distribution of 95 % confidence interval, the predicted kriging estimate is

$$Z_{po} = Z_{tu} \pm 2\sigma \quad (3.48)$$

The kriging approximation can be represented in matrix form as:

$$CW = V \quad (3.49)$$

where C is the spatial covariance matrix, modelled through semi-variogram and given by:

$$C = \begin{bmatrix} 0 & \omega(x_1, x_2) & \dots & \omega(x_1, x_N) & 1 \\ \omega(x_2, x_1) & 0 & \dots & \omega(x_2, x_N) & 1 \\ \vdots & \vdots & \vdots & \vdots & \vdots \\ \omega(x_N, x_1) & \omega(x_N, x_2) & \dots & 0 & 1 \\ 1 & 1 & \dots & 1 & 0 \end{bmatrix} \quad (3.50)$$

where W is the matrix vector of kriging weights and the Lagrange multiplier given by:

$$W = \begin{bmatrix} \kappa_1 \\ \kappa_2 \\ \vdots \\ \kappa_N \\ \nu \end{bmatrix} \quad (3.51)$$

and V in the right-hand side is the vector matrix between observed and the un-observed locations or places given by:

$$V = \begin{bmatrix} \omega(x_1, x_0) \\ \omega(x_2, x_0) \\ \vdots \\ \omega(x_N, x_0) \\ 1 \end{bmatrix} \quad (3.52)$$

The Semi-variogram

Semi-variogram is a mathematical function that indicates the spatial autocorrelation in observations measured at sample points or locations. It is represented in a graph that shows the semi-variance in measure with distance between the sampled locations. It characterizes the spatial continuity or smoothness of a set of data [52]. From the semi-variance cloud graph, we develop a model that describes the variability of the measure with location. The model developed also acts as a prediction tool for estimating the value of a measure at an un-observed position or location. The model is usually chosen from mathematical functions that match the shape of the semi-variance cloud graph [52]. The shape of the model influences the prediction, more so if the curve near the origin differs significantly. Some of the commonly used variogram models include; spherical, exponential and Gaussian. Any semi-variogram is characterized by three properties:

Sill (s): The distance at which the semi-variance approaches a flat region i.e. it is stated as the range or span of the regionalized variable.

Range (a): The range or span defines the neighbourhood within which all the data points are related to each other.

Nugget (c): The nugget is the intercept of the semi-variogram with the vertical axis of the semi-variance values.

The Spherical Model shows a progressive decrease of spatial autocorrelation until some distance beyond which the autocorrelation diminishes to zero. The model can be estimated by [52]:

$$\omega(h) = \begin{cases} c + (s - c)(1.5(\frac{h}{a}) - 0.5(\frac{h}{a})^3) & \text{if } h \leq a \\ s & \text{otherwise} \end{cases} \quad (3.53)$$

The *Exponential Model* shows that spatial autocorrelation decreases exponentially with increasing distance, completely diminishes only at infinite distance. It can be represented by the following function [52]:

$$\omega(h) = c + (s - c)(1 - \exp(\frac{-3h}{a})) \quad (3.54)$$

The *Gaussian Model* is represented by the function [52]:

$$\omega(h) = c + (s - c)(1 - \exp(\frac{-3h^2}{a^2})) \quad (3.55)$$

3.4.2 Thin Plate Spline

Thin-plate spline is a deterministic interpolation technique with a local stochastic component that represents two dimensional curves on three dimensional planes [48]. The thin-plate spline derives its name from the physical situation of bending of a thin surface. It minimizes the bending energy of a thin plate clamped at data points [53]. It is popular because of its efficiency, and capability to produce precise estimates with a marginal number of guiding covariates. It is flexible on how appropriately they fit the data points. Thin-plate spline function can change from a surface that accurately interpolates data, to an increasing smooth function and in certain circumstances a plane subject to the user defined smoothing factor. Its accuracy, therefore depends on its smoothing parameter, hence the essential feature of thin-plate splines is on optimizing this smoothing constraint [9]. A thin plate spline can be represented by the model [9]:

$$p_i = u(y_{1i}, \dots, y_{di}) + \epsilon_i \quad i = 1, \dots, n \quad (3.56)$$

where n is the number of data samples ,
 u is the gradually changing continuous function and
 ϵ_i is the realization of the random variable ϵ .

The function u is assumed to be a continuous long range variable in the process measured by p_i , with independent zero mean and a variance σ^2 . The task in thin plate splines interpolation is to find the process u by a suitable continuous function. A thin plate smoothing spline is produced by minimizing the optimization problem in (3.57) [53]:

$$\frac{1}{n} \sum_{i=1}^n (p_i - v_i)^2 + \Lambda J_m^d(f) \quad (3.57)$$

over functions $v \in \Gamma$, where Γ is a space of functions of m -derivatives in d -dimensions, Λ is a fixed smoothing factor and J_m^d is a measure of roughness of the function v in terms of m^{th} order partial derivatives. v_i are values of the fitted function at the i^{th} data point. The smoothing factor is determined by minimizing the generalized cross validation function

(GCV) and the J_m^d is given by [9] (for $m = d = 2$):

$$J_2^2 = \int_{-\infty}^{\infty} v_{y_1 y_1}^2 + 2v_{y_1 y_2}^2 + v_{y_2 y_2}^2 dy_1 dy_2 \quad (3.58)$$

The corresponding Λ to the spline function v that can represent the process u can be found by minimizing the GCV given by [9]:

$$\frac{1}{n} \frac{(p - M(\Lambda)p)^T (p - M(\Lambda)p)}{(Tr(I - M(\Lambda))/n)^2} \quad (3.59)$$

where $M(\Lambda)$ is the matrix that converts the vector of the data values into the vector model approximated values, hence [9]:

$$p = M(\Lambda)p \quad (3.60)$$

where p is the predicted values' vector. Λ is optimized by minimising the GCV that gives an approximate of the unknown variance of the errors, given by [9]:

$$\sigma^2 = \frac{(p - M(\Lambda)p)^T (p - M(\Lambda)p)}{Tr(I - M(\Lambda))} \quad (3.61)$$

3.4.3 Inverse Distance Weighting

Like other spatial interpolation method, Inverse Distance Weighting (IDW) is used in data analysis to estimate a set of observations related with a set of sampled points or places to a set of un-sampled points or places where observations are not available. The rationale of spatial interpolation is that points closer to each other tend to have similar values than those far apart [54]. Approximations of virtually all spatial interpolation techniques can be denoted as weighted averages of sampled data and they all share the same general approximation method, as follows [47]:

$$Z'(x_o) = \sum_{i=1}^n \lambda_i Z(x_i) \quad (3.62)$$

where Z' is the approximated value at the point of interest x_o , Z is the known value at the sampled point x_i , λ_i is the weighting parameter and, n denotes the number of sampled points used for approximation.

Techniques that use distance based weighting of the data assume that each datum has a local influence that reduces as the distance increases until a point at which the influence is negligible. The inverse distance weighting or inverse distance weighted (IDW) method estimates the values of an attribute at un-sampled points using a linear addition of values at sampled points weighted by an inverse function of the distance from the point of interest to the sampled points. The weighting bias can be represented by (3.63), where d_i is the

distance between x_o and x_i , p is a power parameter, and n is as defined previously [47]:

$$\lambda_i = \frac{1}{\sum_{i=1}^n \frac{1}{(d_i)^p}} \quad (3.63)$$

with the constraint that,

$$\sum_{i=1}^n \lambda_i = 1 \quad (3.64)$$

The main factor influencing the accuracy of IDW is the value of the power parameter and if p is 2, then the method is called Inverse Distance Square. The other factor influencing the accuracy is the number of sampled points used in estimations which is also chosen arbitrarily [47]

3.4.4 Comparison of the three Interpolation Techniques

Here is a brief comparison of the discussed characteristics of the three interpolation techniques. Inverse Distance Weighting interprets spatial correlation in a literal manner. A surface produced with Inverse Distance Weighting will not surpass the well-known value range or pass through any of the sample points. Inverse Distance Weighting is a good interpolator for occurrences whose distribution is strongly interconnected with distance, such as noise. In certain cases, the precision of an Inverse Distance Weighting surface can be enhanced by using line layers as barriers. The Spline interpolation technique integrates a curvilinear model as part of the estimation. A surface created with Spline can surpass the known value range, but must pass through all of the sample points. Kriging is one of the most intricate interpolators. It measures the associations between all of the sample points and then calculates the cell value. A surface generated with Kriging can surpass the known value range, but does not pass through any of the sample points. Table 3.4 summarizes their characteristics.

Table 3.4: Comparison of characteristics of spatial interpolation techniques

Method	Deterministic/ stochastic	Local/ global	Exact interpolator	Limitations	Computing load	Assumptions
Kriging	Stochastic	Local with global semi- variograms	Yes	Accuracy depends on semi-variogram model, data density and search radius	Moderate	Statistical stationary and intrinsic hypothesis
Thin-plate spline	Deterministic with local stochastic component	Local	Yes, within smoothing limits	Goodness of fit pos- sible, but fitted sur- face should be perfectly smooth	Small	Underlying surface is smooth everywhere
Inverse Distance Weighting	Deterministic	Local	Not exact, but can be forced	No error assessments.	Small	Underlying surface is smooth

3.5 Chapter Conclusion

All the fading prediction models discussed here are based on empirical fits of Rayleigh-type distribution of fading data and take into effect the geoclimatic factor of a given region. The geoclimatic factor which caters for climatic characteristics and geographical characteristics of a given location of interest [15]. It has also been seen that the fade distribution is dependent also on frequency and link distance. Therefore, for a given microwave link (with known distance) at a specific operating frequency, the fade distribution is seen to vary depending on the geoclimatic factor. ITU-R P.530 [36], in estimating the probability of fade distribution, also takes into account path inclination of the given link into consideration. This factor is calculated from the antenna heights and link distance (3.9). We can then conclude that for a given microwave link, the multipath fading distribution is to a greater extent dependent on the geoclimatic factor of the region of interest. Determining this factor then, to a link design engineer, should be of great interest to be able to predict accurately the fading distribution of a system and propose appropriate fade mitigation techniques for the link in question.

Chapter 4

Statistical Estimation of Fade Depth and Outage Probability

4.1 Introduction

In this chapter, the probability that a fade depth of a certain magnitude will take place and hence the probability of outage is estimated based on the effect of the geoclimatic factor derived from atmospheric refractivity gradient. The refractivity gradient is estimated from the radiosonde data obtained from South Africa Weather Service (SAWS). The radiosonde soundings are usually made twice per day and allow for estimation of vertical refractivity profiles derived from their temperature, pressure and humidity measurements. However, radiosonde data suffer from two major drawbacks, namely; poor spatial resolution, and, lack of time resolutions, hence the data has limited capability to represent diurnal variation [55, 56]. Surface measurements from stations give a better resolution than radiosondes, more so in space. Diurnal patterns can be achieved from surface data taken three to four times a day. The limitation here is lack of values above the surface for vertical refractivity profile approximations. This drawback can be minimized by use of sensors positioned at ground level for surface measurements and at specific altitudes above the ground from which radio refractivity and refractivity gradients can be determined [55]. When a number of stations needs to be considered then the cost of the latter method rises tremendously. This leaves the radiosonde soundings as the best bargain for radioclimatological analysis supported with validation schemes for the resulting data. In this study, we have used radiosonde data to estimate fade depth and outage probability in Southern Africa region.

4.2 Study Area

South Africa is located in the southern part of the continent of Africa. It experiences four seasons in a year with slight variations in the regions. The summer season is from mid-October to mid-Feb, with hot sunny weather and thunderstorms in the afternoon; apart from Western Cape which gets its rain in winter. Autumn is from mid-Feb to April, winter from May to July, and spring coming in from August to mid-October. South Africa is bordered by the Indian Ocean and Atlantic Ocean on the southern part of the country. It is divided into nine regions: Western Cape (with Cape Town as the main city) is typically Mediterranean, with temperature ranging from 5°C to 22°C. Eastern Cape is mainly Savannah and lies between subtropical climate of KwaZulu Natal and the Mediterranean of



Figure 4.1: The Map of South Africa [4]

Western Cape. Its temperature ranges from 7°C in winter and 26°C in summer. KwaZulu Natal with Durban as the main city is generally warm with temperature ranging from 16°C to 33°C . Gauteng is mainly temperate with mild climate, neither humid nor too hot with Pretoria as the main city. The Northern Province of South Africa is mostly subtropical with Polokwane as the main city. Free State region with Bloemfontein as the main city has Steppe climate with temperature ranging from as low as 1°C in winter to 32°C in summer. North West province forms part of the Kalahari Desert with temperatures from 2°C to 34°C . Mpumalanga is known as a region of two halves; subtropical Lowveld plains and high-lying grassland savannah of the Highveld escarpment. Lastly, the Northern Cape is mainly semi desert with a small section of Green Kalahari [4, 57, 58]. Figure 4.1 shows the map of South Africa and neighbouring countries of Lesotho, Swaziland, Botswana and Namibia [57].

4.3 Data Collection and Processing

Radioclimatic data used in this study was collected from South Africa Weather Service (SAWS), collected over a period of ten years (2001-2010) from radiosonde soundings. The data received was in Notepad format. We then exported this data to Excel for ease of manipulation. Data for a three year (2004-2006) period was then filtered out from the whole data. The radiosonde data has values of temperature, humidity and pressure at different heights among other parameters.

For determining point refractivity gradient, the values of temperature, humidity and pressure at surface level and 65 m above the surface are filtered out from the data for further processing. Since radiosonde soundings do not give data at certain specific heights, we used $65 \text{ m} \pm 10\%$ for the 65 m height. For determining refractivity gradient, surface and 100 m values of the above mentioned parameters were filtered out from the raw data for both night and day values as the radiosonde sounding reports these values twice per day at different heights. Processing of the data was then done in Excel for determination of both refractivity gradient and point refractivity gradient, from which cumulative distribution functions of point refractivity gradient is estimated.

It should be noted that SAWS data also contains wind speed and wind direction which are not of our interest and are filtered out when processing the data.

4.4 Geoclimatic Factor Determination

Geoclimatic factor is estimated from the statistics of distribution of refractivity gradient. We first compute refractivity as given in Chapter 2 with equation 2.2, given here for convenience as [2, 15]:

$$N = (n - 1) * 10^6 = \frac{77.6}{T} (P + 4810 \frac{e}{T}) \quad (4.1)$$

where all the parameters are as earlier defined in Chapter 2. The water vapour pressure e is related to the relative humidity H as a percentage and air temperature t ($^{\circ}\text{C}$) with the following expression [2]:

$$e = \frac{6.1121H}{100} \exp \frac{17.502t}{t + 240.97} \quad (4.2)$$

The refractivity gradient which show the relationship of how refractivity changes with height is of greater interest to the LOS link designers. Multipath fading can only occur if this refractivity gradient in the atmosphere varies with height [10]. The atmospheric refractivity in the lower atmosphere (65m above ground level) is estimated from (4.1) at various heights. Partial water vapour is determined from (4.2). Refractivity gradient is estimated from (4.3) where N_1 and N_2 are the refractivity at heights h_1 and h_2 respectively [59]:

$$\frac{dN}{dh} \approx \frac{N_2 - N_1}{h_2 - h_1} \quad (4.3)$$

The cumulative distribution of $\frac{dN}{dh}$ is then determined from the frequency of occurrence. This is done by calculating $\frac{dN}{dh}$ for each of the months, then determining the frequency of occurrence of these values within given ranges of data. The probability of occurrence is determined from the frequency of occurrence after which a CDF is calculated. A plot is then made for ranges of data against the calculated CDFs. From the cumulative distributions, the point refractivity gradient not exceeded for 1 % of each of the months is then determined. In case where the 1 % of the refractivity gradient is not available from the distribution curves, a spatial interpolation technique approach is used to estimate the value. The interpolation technique applied in the study is the inverse distance weight technique described in the previous section. The technique is chosen because it is simple and direct to use with minimum computer memory resource required. Again it is possible to optimize its accuracy with ease. The geoclimatic factor (for quick planning) can be calculated from the approach given in ITU-R P530-14 [7]:

$$K = 10^{-4.6-0.0027dN_1} \quad (4.4)$$

where dN_1 is as defined previously in Chapter 3. The cumulative distribution for $\frac{dN}{dh}$ is shown in Figure 4.2, from which the point refractivity gradient is read and where the value is not available, Inverse Distance weighting described in Chapter 3 is used to estimate this value.

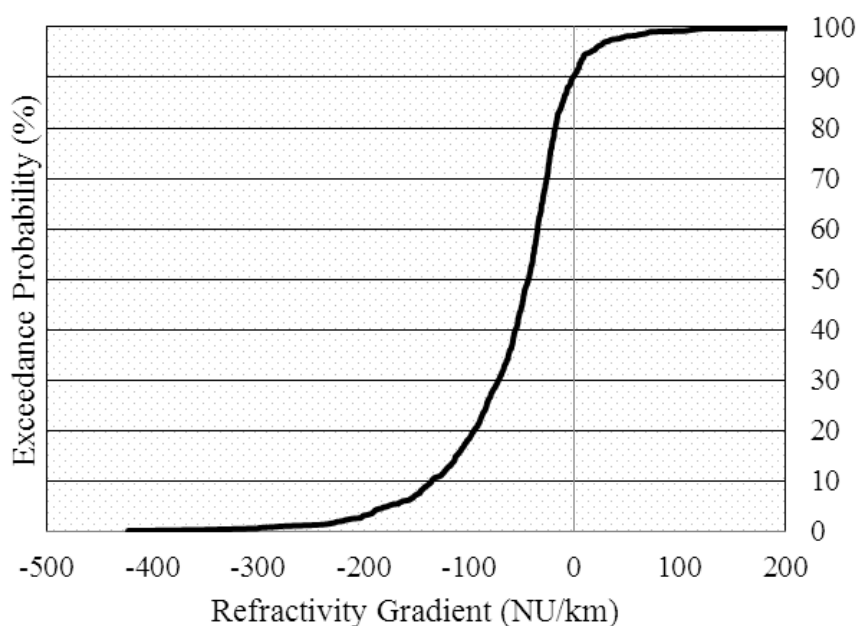


Figure 4.2: Cumulative Distribution Curve for $\frac{dN}{dh}$

4.5 Fade Depth Prediction

Fade depth is the ratio, stated in decibels, of a reference signal power to the signal power for the duration of a fade [60]. ITU-R [7] provides methods for estimating single frequency fading distribution at deep fade depths in the average worst month for both quick planning and for detailed planning purposes. They both involve three steps: estimating the geoclimatic factor K , then calculating the path inclination and lastly calculating the proportion of time that a certain fade depth A (dB) is exceeded in the average worst month. Geoclimatic factor determination has been described in section 4 above. Path inclination (ε_p) can be determined from transmit and receive antenna elevations h_e (m) and h_r (m), above sea level and the hop length d (km) from equation 3.9, again given here for convenience [7]:

$$|\varepsilon_p| = \frac{|h_e - h_r|}{d} \quad (4.5)$$

For quick planning purpose, the third step can then be estimated from (4.6), where p_w is the proportion of time that fade depth A (dB) is exceeded in the average worst month, h_L is the altitude of the lower antenna, f (GHz) is the frequency, d and K are path length and geoclimatic factor, respectively.

$$p_w = Kd^{3.1}(1 + |\varepsilon_p|)^{-1.29}f^{0.8} \times 10^{(-0.00089*h_L - A/10)} \quad (4.6)$$

Due to the ever varying nature of the propagation medium, the knowledge of the probability of a fade depth of a particular amount to occur, will lead directly to the probability of outage, assuming the given fade depth leads to the received signal falling below the squelch level [10]. In this study, we have used ITU-R method for quick planning which has an overall standard deviation of error in predictions of 5.9 dB. The accuracy in predictions will improve if the ITU-R method for detailed link design, which requires terrain data, were used. The overall standard deviation of error for detailed applications method is 5.7 dB [7].

4.6 Results and Discussion

Radiosonde data collected from SAWS for three years (2004 to 2006) is used in the analysis. Table 4.1 shows the number of samples per month used in determining the point refractivity gradient. Radiosonde balloons are launched twice per day at around 10am in the morning and 11pm in the night. However, in some cases in various months data was available only once per day. In some isolated circumstances, data is reported thrice per day hence showing the non-uniformity is the monthly samples used in the analysis. It is worth noting that radiosonde soundings do not report climatic parameters (i.e. temperature, humidity and pressure) at definite heights. Therefore, the value of dN_1 is estimated using (4.3) where N_1 is considered at the h_1 value closest to 65 m height, so that h_1 falls within $65 \pm 10\%$ m [59].

Table 4.1: Data Samples per Month in each Year used in Determining Point Refractivity Gradient

		Jan	Feb	Mar	Apr	May	Jun	Jul	Aug	Sep	Oct	Nov	Dec	Total
Durban	2004	36	37	45	42	45	47	48	50	51	43	48	48	540
	2005	55	50	56	57	52	61	50	45	43	44	52	44	609
	2006	62	55	62	56	62	63	62	61	60	61	61	59	724
Cape Town	2004	57	60	61	59	61	61	60	62	61	64	63	60	729
	2005	61	57	60	62	61	61	60	63	62	59	59	60	725
	2006	57	59	61	60	56	62	60	61	61	58	60	62	717
Pretoria	2004	56	57	61	58	62	59	55	56	61	62	61	56	704
	2005	61	58	66	59	56	60	61	55	62	62	58	60	720
	2006	62	58	61	61	60	62	63	60	63	59	60	61	730
Bloemfontein	2004	35	29	36	58	64	61	66	64	62	35	32	42	584
	2005	37	34	38	57	60	55	67	59	63	60	59	60	649
	2006	60	59	64	63	33	36	31	39	34	32	31	33	515
Polokwane	2004	36	43	43	18	28	28	25	24	27	50	60	57	439
	2005	48	50	47	19	32	25	28	30	31	38	67	60	475
	2006	61	62	58	59	36	30	32	32	30	38	32	33	503

4.6.1 Refractivity and Refractivity Gradient

The mean monthly surface refractivity statistics for each location is given in Figure 4.3. The figure show that surface refractivity varies with seasons in the year with high values experienced in summer months when the temperatures are high and lowest in winter months when temperature is low. Durban shows high values of surface refractivity followed by Port Elizabeth and Cape Town record the lowest values.

Durban's highest mean value (about 370 NU) is for the month of February and the lowest is recorded in June, during winter. Figure 4.4 shows the standard deviations for each of the months in each location, from which we can deduce that refractivity not only varies with season but also exhibits variation within each of the months. Surface refractivity is an important parameter in radio climatology since it aids in determining refractivity gradient at other heights and also in determining the refractivity at sea level (refractivity exponential model) [61]

The percentage of occurrence of super refractivity is shown in Figure 4.5. Durban exhibits the highest super refractivity condition with the month of March being the worst month with occurrence around 29 % of the time. The lowest occurrence is again recorded in June with 11 % of the time for Durban. The high value of occurrence of super refractivity for Durban can be attributed to the ever changing climatic conditions in Durban. Cape Town exhibits the highest occurrence in the months of January and October (both summer months) with 21 % of the time and lowest in June with 10.5 % of the time. The trend is different for Port Elizabeth with the highest being in the month of May, 21 % of the time and the lowest being in July with 13.5 % of the time.

Figures 4.6, 4.7, and 4.8 show cumulative distribution of refractivity gradients for three coastal regions. Figure 4.6 shows the distribution for Cape Town from which we can deduce that ducting conditions (dN/dh less than -157 N/km) exist for around 5 % of the time for the month of May being the highest. For Durban (Figure 4.7), the highest time percentage

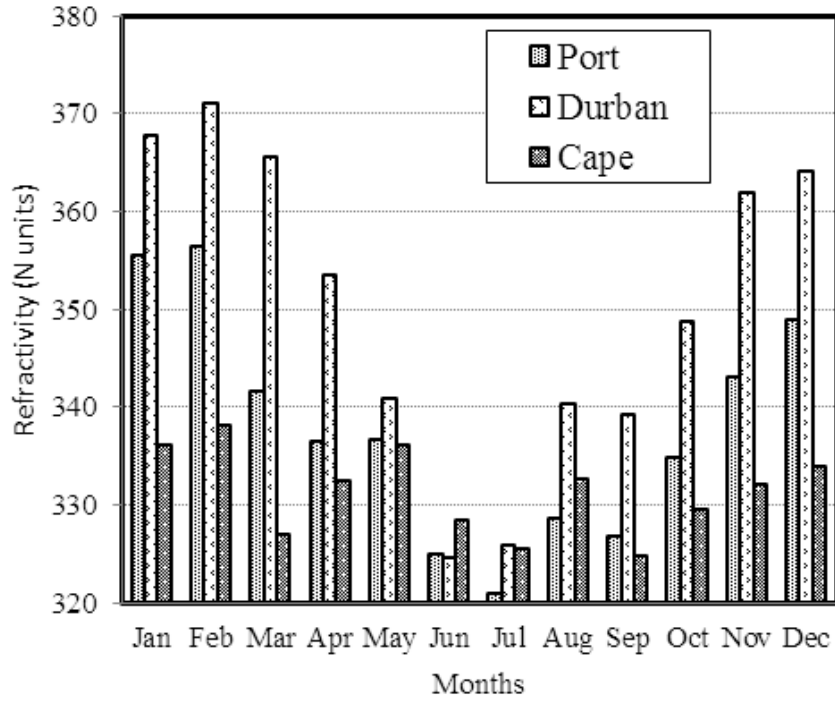


Figure 4.3: Monthly variation of three coastal regions' Mean surface refractivity

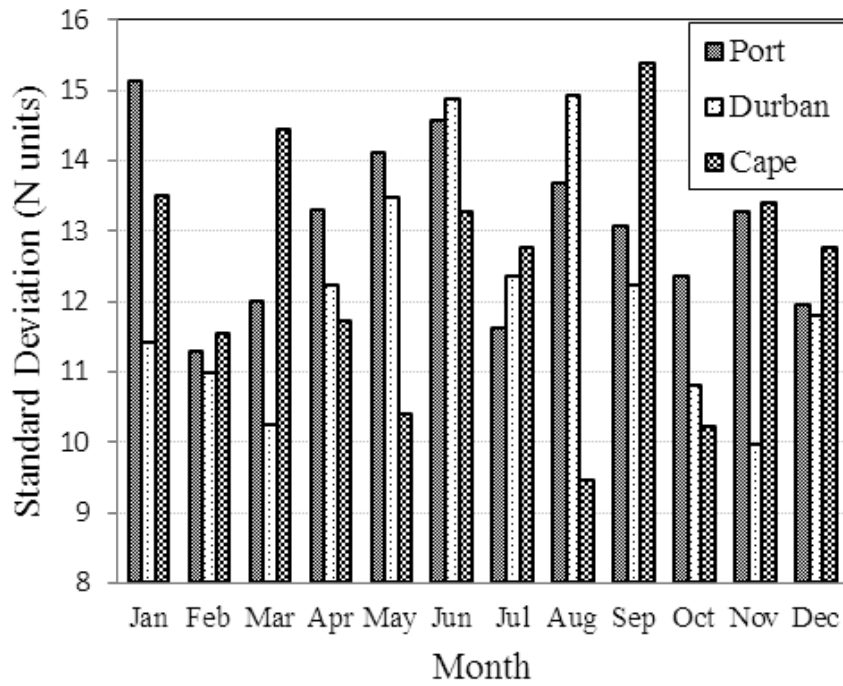


Figure 4.4: Monthly variation of three coastal regions' Standard deviation for surface refractivity

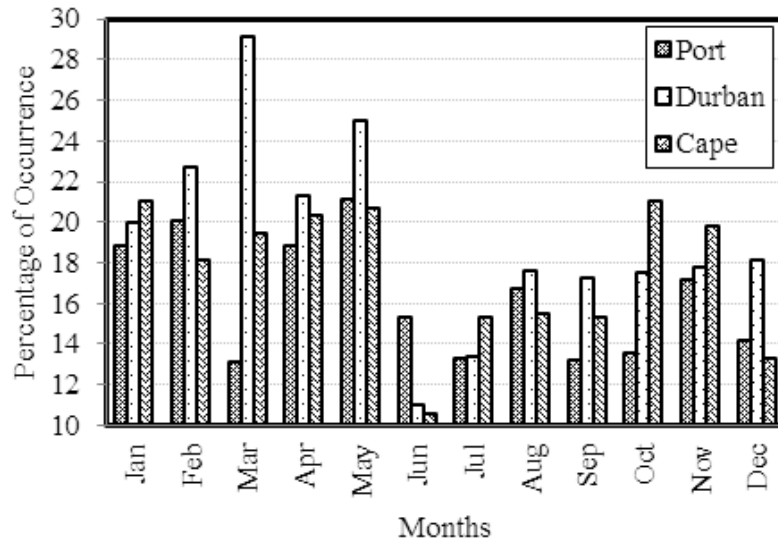


Figure 4.5: Occurrence of super-refractivity conditions for three coastal regions in South Africa

of duct occurrence is in August at about 6 %. Figure 4.8 shows the distribution for Port Elizabeth with 4 % of time duct occurrence experienced in November.

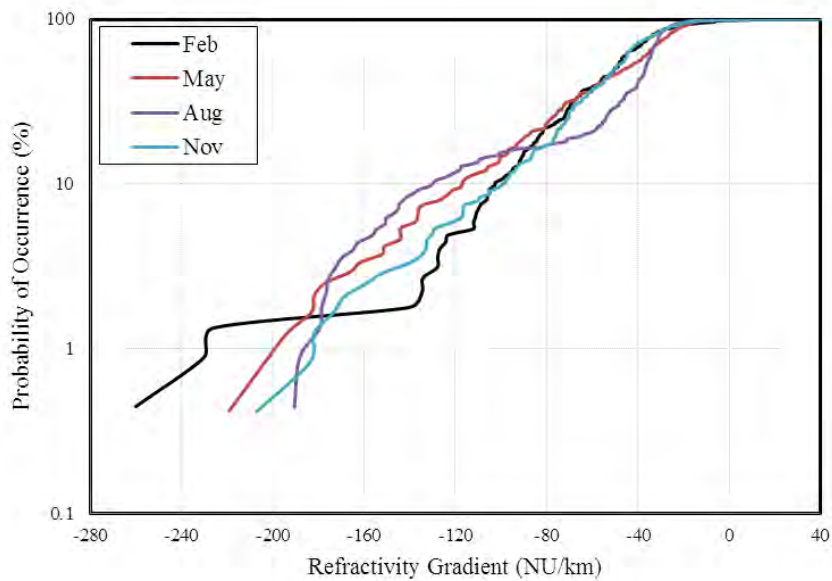


Figure 4.6: Cumulative distribution of the monthly refractivity gradient for Durban

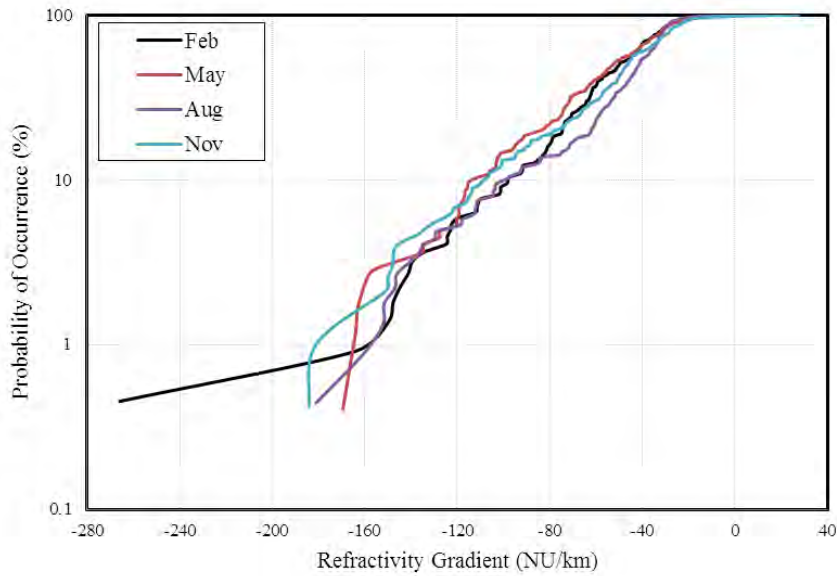


Figure 4.7: Cumulative distribution of the monthly refractivity gradient for Cape Town

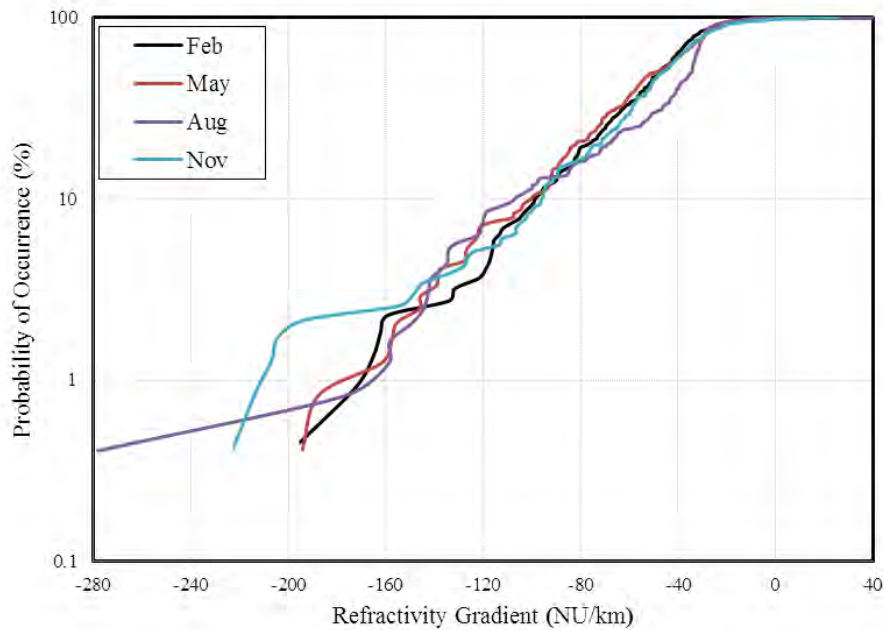


Figure 4.8: Cumulative distribution of the monthly refractivity gradient for Port Elizabeth

Duct occurrence along the coastal regions is due to variation of water vapour pressure as a result of variation of humidity in the air. Normally air in close vicinity to the surface of large water bodies is more humid (about 100 %) due to evaporation and denser and it decreases with increase in altitude. However, sea breeze at times drives the dense air from the surface and replaces it with a less humid air. This with the continuous change in sea-air temperature causes the refractivity gradient to vary rapidly hence resulting in the anomalous propagation.

4.6.2 Geoclimatic Factor

Generally, for the design of radio communication systems, the essential statistics of the effects of propagation relate to that of the worst month. The worst month is the month in a year in which the a pre-specified threshold for any performance is surpassed for the longest period of time. It must also be noted that the worst month is not necessarily the same month for all the threshold levels [62]. Figures 4.9 – 4.13 show monthly variations of point refractivity gradient for the three years and their averages. Results indicate that the worst cases fall in the summer months apart from Cape Town that has the worst cases in winter. This seems to follow the same trend seen in Section 4.2, where all the regions had their rainy season in summer apart from Cape Town having its rainy season in winter.

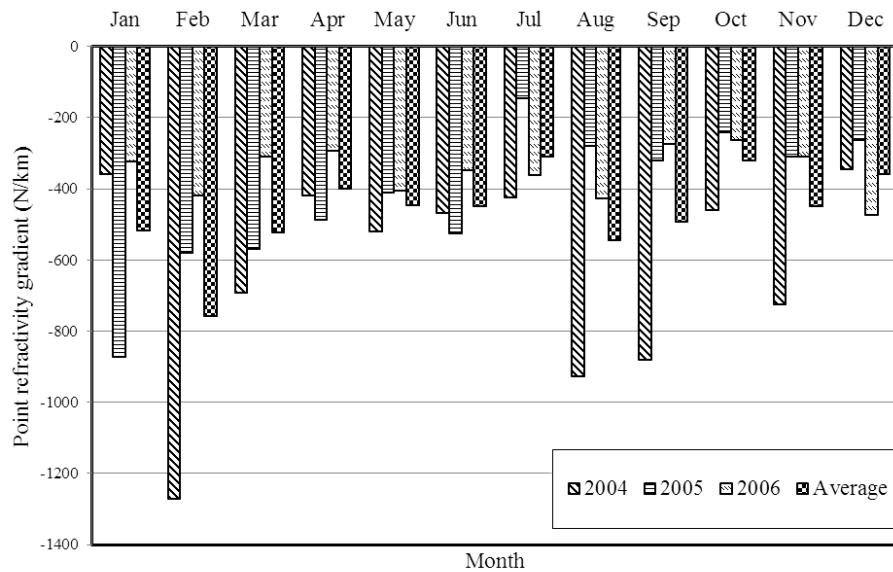


Figure 4.9: Monthly variation of point refractivity gradient (dN_1) for Durban

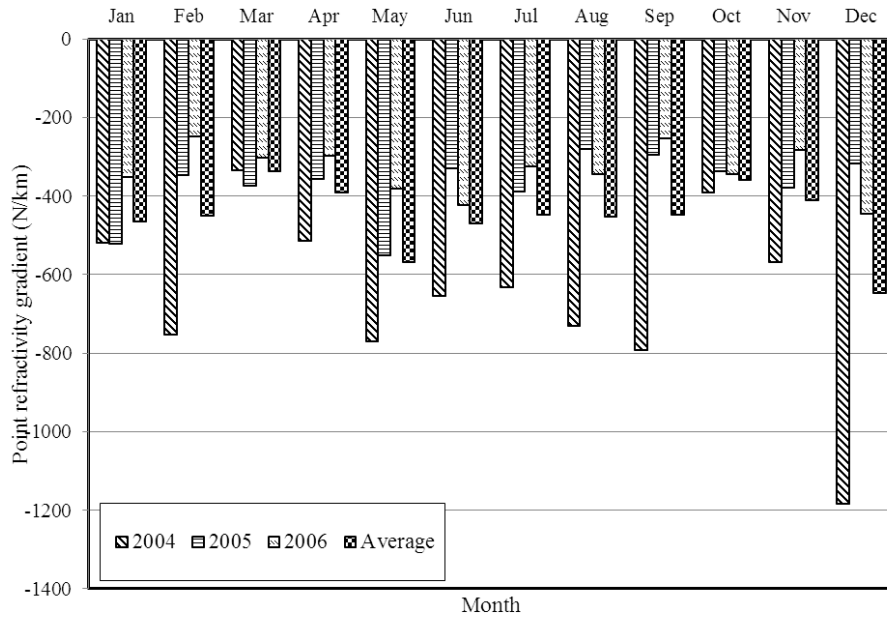


Figure 4.10: Monthly variation of point refractivity gradient (dN_1) for Cape Town

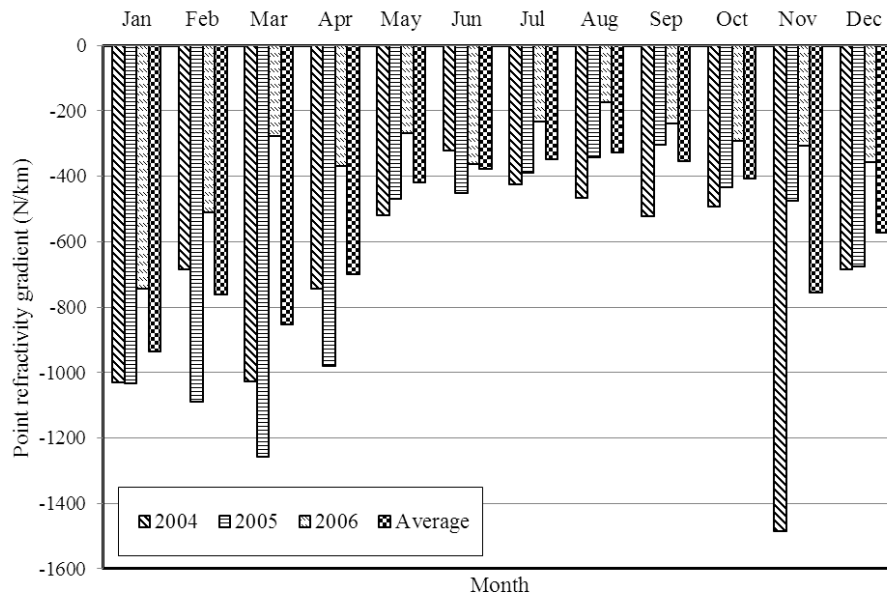


Figure 4.11: Monthly variation of point refractivity gradient (dN_1) for Pretoria

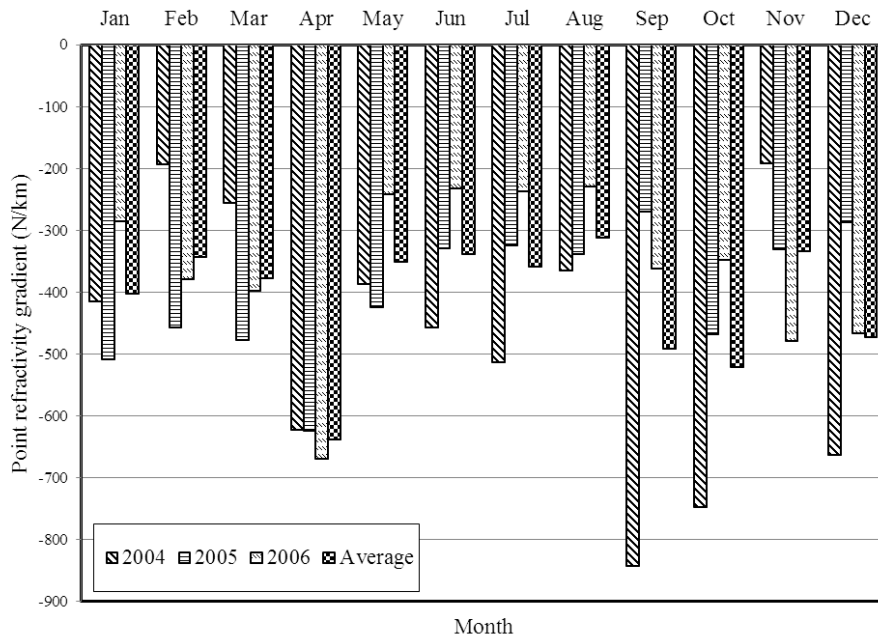


Figure 4.12: Monthly variation of point refractivity gradient (dN_1) for Bloemfontein

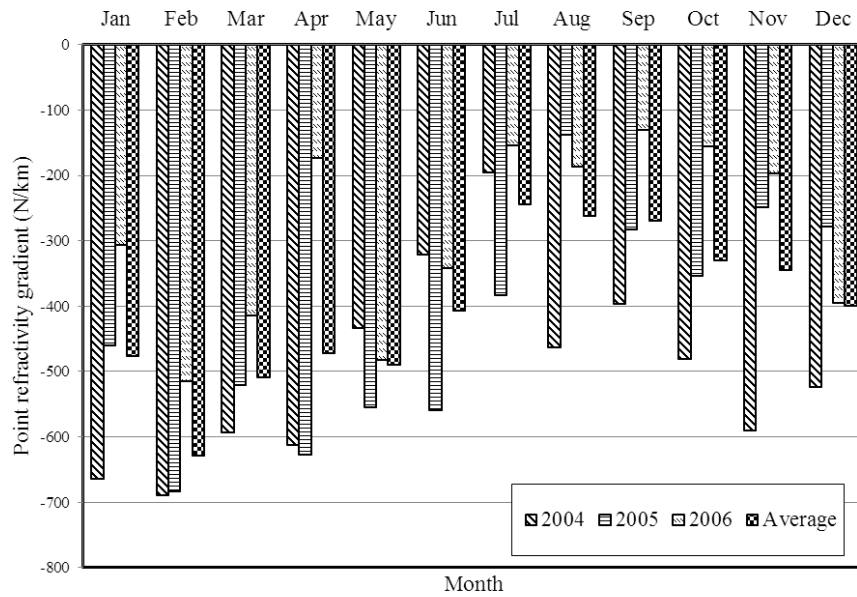


Figure 4.13: Monthly variation of point refractivity gradient (dN_1) for Polokwane.

Table 4.2 provides the summary of the worst month for the regions with point refractivity gradient values and their corresponding geoclimatic factor K values. Tables 4.3 – 4.7 tabulate the values of geoclimatic factor K for each of the months for the three year period under study in the five locations in South Africa. As expected the values of geoclimatic factors are inverse to those of point refractivity gradients. It should be noted that, in estimating the average values of the geoclimatic factor, we first average the point

refractivity gradient values and then we apply (4.4) to approximate the geoclimatic factor values.

Table 4.2: Worst Month Values

	Worst Month	Point Refractivity Gradient	Geoclimatic Factor K
Durban	February	-756	2.77×10^{-3}
Cape Town	December	-649	1.42×10^{-3}
Pretoria	January	-935	8.42×10^{-3}
Bloemfontein	April	-638	1.33×10^{-3}
Polokwane	February	-629	1.25×10^{-3}

Table 4.3: Geoclimatic Factor K for Durban

	Durban			
	2004	2005	2006	Average
Jan	2.31×10^{-4}	5.66×10^{-3}	1.88×10^{-4}	6.27×10^{-4}
Feb	6.82×10^{-2}	9.22×10^{-4}	3.36×10^{-4}	2.77×10^{-3}
Mar	1.86×10^{-3}	8.58×10^{-4}	1.70×10^{-4}	6.48×10^{-4}
Apr	3.39×10^{-4}	5.19×10^{-4}	1.56×10^{-4}	3.01×10^{-4}
May	6.30×10^{-4}	3.23×10^{-4}	3.13×10^{-4}	3.99×10^{-4}
Jun	4.61×10^{-4}	6.57×10^{-4}	2.19×10^{-4}	4.05×10^{-4}
Jul	3.51×10^{-4}	6.14×10^{-5}	2.38×10^{-4}	1.72×10^{-4}
Aug	7.94×10^{-3}	1.42×10^{-4}	3.53×10^{-4}	7.35×10^{-4}
Sep	5.98×10^{-3}	1.82×10^{-4}	1.37×10^{-4}	5.31×10^{-4}
Oct	4.35×10^{-4}	1.12×10^{-4}	1.29×10^{-4}	1.84×10^{-4}
Nov	2.28×10^{-3}	1.71×10^{-4}	1.72×10^{-4}	4.06×10^{-4}
Dec	2.13×10^{-4}	1.29×10^{-4}	4.71×10^{-4}	2.34×10^{-4}

Table 4.4: Geoclimatic Factor K for Pretoria

Pretoria				
	2004	2005	2006	Average
Jan	1.52×10^{-2}	1.55×10^{-2}	2.55×10^{-3}	8.42×10^{-3}
Feb	1.77×10^{-3}	2.21×10^{-2}	6.06×10^{-4}	2.87×10^{-3}
Mar	1.48×10^{-2}	6.27×10^{-2}	1.41×10^{-4}	5.07×10^{-3}
Apr	2.57×10^{-3}	1.12×10^{-2}	2.51×10^{-4}	1.93×10^{-3}
May	6.30×10^{-4}	4.63×10^{-4}	1.34×10^{-4}	3.39×10^{-4}
Jun	1.86×10^{-4}	4.17×10^{-4}	2.41×10^{-4}	2.65×10^{-4}
Jul	3.52×10^{-4}	2.18×10^{-4}	1.07×10^{-4}	2.20×10^{-4}
Aug	4.56×10^{-4}	2.12×10^{-4}	7.45×10^{-5}	1.93×10^{-4}
Sep	6.45×10^{-4}	1.66×10^{-4}	1.11×10^{-4}	2.28×10^{-4}
Oct	5.42×10^{-4}	3.72×10^{-4}	1.54×10^{-4}	3.14×10^{-4}
Nov	2.57×10^{-1}	4.84×10^{-4}	1.68×10^{-4}	2.76×10^{-3}
Dec	1.77×10^{-3}	1.68×10^{-3}	2.32×10^{-4}	8.85×10^{-4}

Table 4.5: Geoclimatic Factor K for Cape Town

Cape Town				
	2004	2005	2006	Average
Jan	6.25×10^{-4}	6.44×10^{-4}	2.24×10^{-4}	4.51×10^{-4}
Feb	2.71×10^{-3}	2.18×10^{-4}	1.17×10^{-4}	4.11×10^{-4}
Mar	2.00×10^{-4}	2.56×10^{-4}	1.64×10^{-4}	2.03×10^{-4}
Apr	6.17×10^{-4}	2.32×10^{-4}	1.61×10^{-4}	2.84×10^{-4}
May	3.03×10^{-3}	7.73×10^{-4}	2.71×10^{-4}	8.59×10^{-4}
Jun	1.48×10^{-3}	1.94×10^{-4}	3.48×10^{-4}	4.64×10^{-4}
Jul	1.28×10^{-3}	2.82×10^{-4}	1.89×10^{-4}	4.09×10^{-4}
Aug	2.35×10^{-3}	1.44×10^{-4}	2.15×10^{-4}	4.18×10^{-4}
Sep	3.49×10^{-3}	1.58×10^{-4}	1.21×10^{-4}	4.06×10^{-4}
Oct	2.87×10^{-4}	2.05×10^{-4}	2.15×10^{-4}	2.33×10^{-4}
Nov	8.57×10^{-4}	2.67×10^{-4}	1.45×10^{-4}	3.21×10^{-4}
Dec	3.93×10^{-2}	1.80×10^{-4}	4.01×10^{-4}	1.42×10^{-3}

Table 4.6: Geoclimatic Factor K for Bloemfontein

	Bloemfontein			
	2004	2005	2006	Average
Jan	3.32×10^{-4}	5.92×10^{-4}	1.48×10^{-4}	3.08×10^{-4}
Feb	8.39×10^{-5}	4.32×10^{-4}	2.66×10^{-4}	2.13×10^{-4}
Mar	1.24×10^{-4}	4.90×10^{-4}	2.99×10^{-4}	2.63×10^{-4}
Apr	1.20×10^{-3}	1.21×10^{-3}	1.61×10^{-3}	1.33×10^{-3}
May	2.78×10^{-4}	3.53×10^{-4}	1.13×10^{-4}	2.23×10^{-4}
Jun	4.30×10^{-4}	1.94×10^{-4}	1.06×10^{-4}	2.07×10^{-4}
Jul	6.13×10^{-4}	1.90×10^{-4}	1.10×10^{-4}	2.33×10^{-4}
Aug	2.44×10^{-4}	2.06×10^{-4}	1.05×10^{-4}	1.74×10^{-4}
Sep	4.74×10^{-3}	1.34×10^{-4}	2.39×10^{-4}	5.34×10^{-4}
Oct	2.61×10^{-3}	4.63×10^{-4}	2.19×10^{-4}	6.42×10^{-4}
Nov	8.32×10^{-5}	1.97×10^{-4}	4.92×10^{-4}	2.01×10^{-4}
Dec	1.55×10^{-3}	1.49×10^{-4}	4.56×10^{-4}	4.73×10^{-4}

Table 4.7: Geoclimatic Factor K for Polokwane

	Polokwane			
	2004	2005	2006	Average
Jan	1.55×10^{-3}	4.39×10^{-4}	1.69×10^{-4}	4.86×10^{-4}
Feb	1.83×10^{-3}	1.75×10^{-3}	6.13×10^{-4}	1.25×10^{-3}
Mar	1.00×10^{-3}	6.40×10^{-4}	3.30×10^{-4}	5.96×10^{-4}
Apr	1.14×10^{-3}	1.24×10^{-3}	7.38×10^{-5}	4.70×10^{-4}
May	3.71×10^{-4}	7.29×10^{-4}	5.01×10^{-4}	5.28×10^{-4}
Jun	1.85×10^{-4}	8.08×10^{-4}	2.11×10^{-4}	3.16×10^{-4}
Jul	8.46×10^{-5}	2.72×10^{-4}	6.54×10^{-5}	1.15×10^{-4}
Aug	4.47×10^{-4}	5.92×10^{-5}	7.99×10^{-5}	1.28×10^{-4}
Sep	2.95×10^{-4}	1.45×10^{-4}	5.65×10^{-5}	1.34×10^{-4}
Oct	5.00×10^{-4}	2.26×10^{-4}	6.58×10^{-5}	1.95×10^{-4}
Nov	9.82×10^{-4}	1.17×10^{-4}	8.56×10^{-5}	2.14×10^{-4}
Dec	6.48×10^{-4}	1.41×10^{-4}	2.94×10^{-4}	3.00×10^{-4}

Figures 4.9 – 4.13 have shown monthly variation of point refractivity gradient for three years in each of the five locations. Figure 4.14 shows yearly averages for the point refractivity gradient with corresponding error bars to indicate the confidence intervals of our estimates. The average for the three years is also shown for each of the locations. It's evidenced that point refractivity gradient also varies annually. In our study, the results show that the year 2004 has the lowest value of point refractivity gradient and the value becomes less negative in the succeeding years. The standard error (SE) for each year was calculated from: $SE = s/\sqrt{n}$, where s is the sample standard deviation

and n is the number of samples. From the values of SE , confidence intervals (CI) which shows the range in which the “true” value of the estimates fall were calculated from: $CI = m \pm 1SE$, where m is the mean of point refractivity gradient of each of the years. Monthly variation of point refractivity gradient depends on season with worst months occurring mainly in summer. However, annual variation seems to follow some cycle which needs to be determined and we are processing data for more years to ascertain this hypothesis.

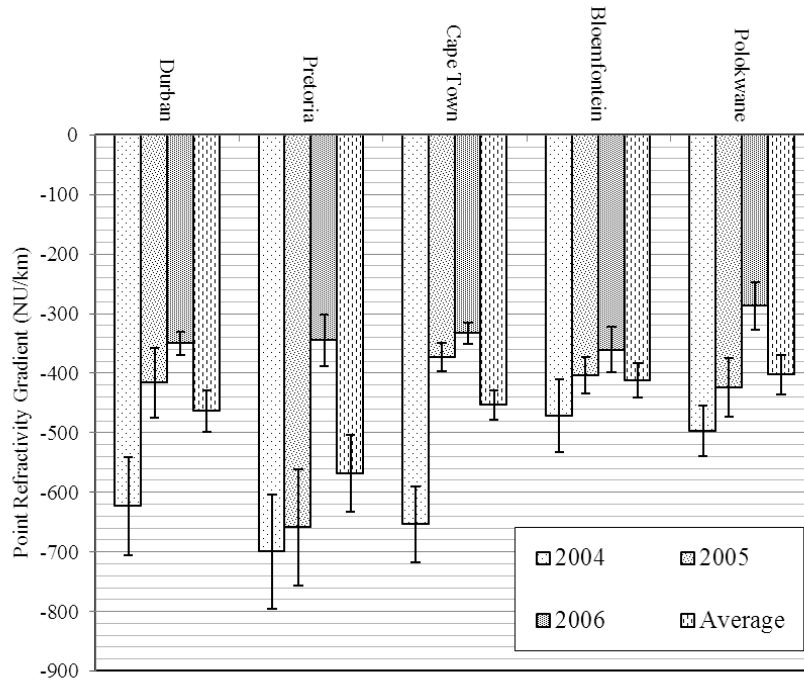


Figure 4.14: Confidence intervals graph for the yearly average of point refractivity gradient for each of the five sites in South Africa

The ITU-R P.453-9 [22] normally recommends seasonal estimation of point refractivity gradient: February to cater for January to March, May to cater for April to June, August to cater for July to September and lastly November for October to December. Our seasonal values are provided in Figure 4.15 with their corresponding geoclimatic factor K values in Figure 4.16. These figures also indicate that for all the regions, the worst month falls in February which is summer apart from Cape Town and Bloemfontein with the worst month being May. In addition to seasonal variability, the geoclimatic factor K also varies with region/climatic types as expected. The results compare well with work done earlier in Durban [15,28,63] and [41] in which the worst month for Durban was found to be February followed by August. In [15], where one year radiosonde data is used in the analysis, the average point refractivity gradient was found to be -572.38 N-units/km. In [63], the average point refractivity gradient for Durban was found to be -523 N-units/km with ten months radiosonde data. This fits within our confidence interval for the year 2004 for Durban which ranges from -705.63 NU/km to -541.75 NU/km (see Figure 4.14) with an average of -623.69 NU/km. However, the succeeding years values are not within a close range.

This seems to confirm our earlier hypothesis that annual variation follow some cycle. In our case, the average value for three years is -459.865 N-units/km. The difference in the values is likely due to the size of data used in the analysis and the height resolutions of radiosonde soundings.

Table 4.8 is a comparison of the estimated values of geoclimatic factor K and point refractivity gradient values with the ITU-R value [22] for Southern Africa. The results imply that the ITU-R value (-400 N-units/km) under estimates the geoclimatic factor K and it does not consider the worst month situation. Moreover, ITU-R assumes one value of point refractivity gradient for the whole of South Africa, which should never be the case. Geoclimatic factor which is a function of point refractivity gradient is representative of both topology and climatic conditions of a region. South Africa has more than one climatic type scattered across its regions, hence, it is not a good assumption that it can have one value of point refractivity across all its regions. The average values in Table 4.8 are calculated from the mean of the various locations in South Africa. These values are still lower than the ITU-R value. This can be attributed to the difference in data used in estimation and again, the study shows that the value for South Africa is not constant throughout the region.

Table 4.8: Comparison of ITU-R and Estimated Values of Point Refractivity Gradient and Geoclimatic Factor K

	Point Refractivity Gradient (NU/km)		Geoclimatic Factor K	
	Mean	Worst Month	Mean	Worst Month
Durban	-463	-599 (Feb)	4.48×10^{-4}	1.04×10^{-3}
Cape Town	-454	-476 (May)	4.21×10^{-4}	4.84×10^{-4}
Pretoria	-568	-850 (Feb)	5.58×10^{-4}	4.97×10^{-3}
Bloemfontein	-412	-443 (May)	3.25×10^{-4}	3.95×10^{-4}
Polokwane	-403	-538 (Feb)	3.07×10^{-4}	7.13×10^{-4}
Average	-460	-581	4.38×10^{-4}	9.32×10^{-4}
ITU-R	-400		3.02×10^{-4}	

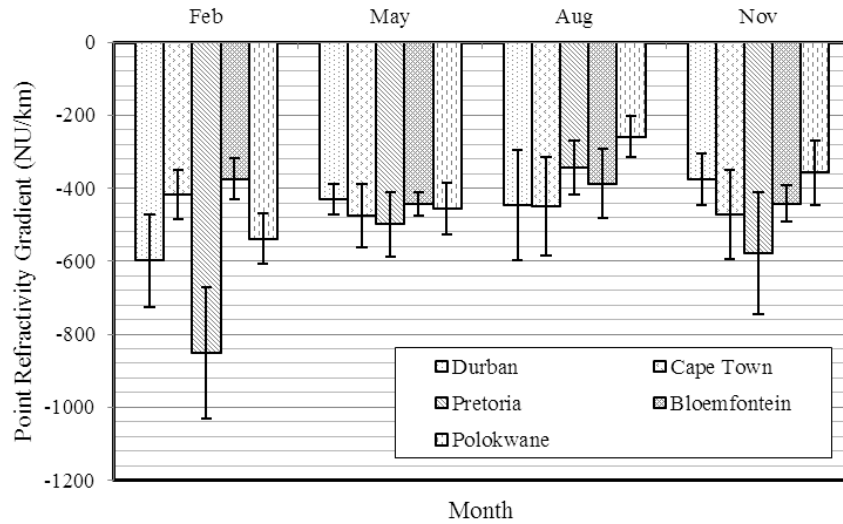


Figure 4.15: Seasonal variation of point refractivity gradient (dN_1)

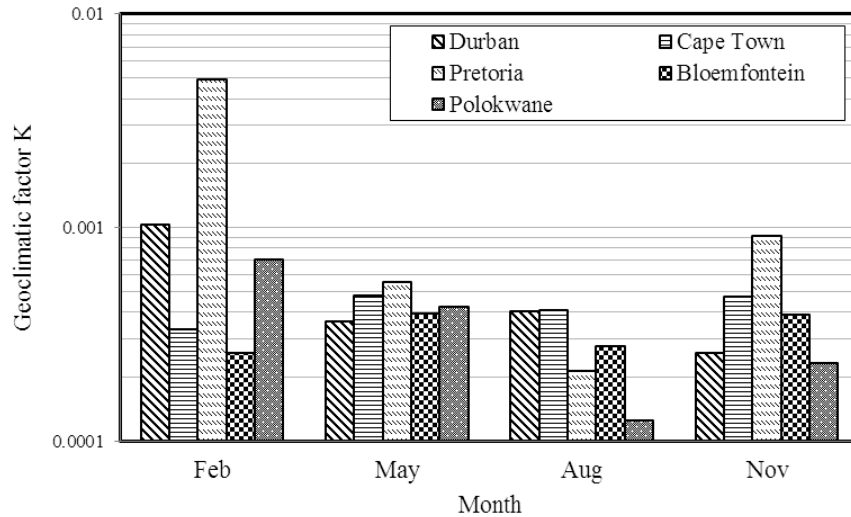


Figure 4.16: Seasonal variation of geoclimatic factor K

4.6.3 Fade Depth and Outage Prediction

The understanding of fading phenomena is very important in the design and performance of wireless systems. Microwave link attenuation due to multipath is not a permanent occurrence and its probability of occurrence needs to be known for a reliable terrestrial link [10]. It has been mentioned earlier that multipath fading is a random phenomenon which can only be described statistically. The ITU-R method described in Section 4.5 is used in estimating the probability of time that a certain fade depth is exceeded. Prediction of fading phenomena can be made at a fixed value of fade depth or estimated at a certain percentage of outage. The values of geoclimatic factor K as determined in the previous sub-section are used in the prediction of the probability of time a certain fade depth is exceeded. Equation (4.6) requires link parameters and in our analysis, we have used the

following parameters for the two coastal towns (Durban and Cape Town): $f = 11$ GHz, $h_e = 124$ m , $h_r = 76$ m and $d = 48.25$ km.

Figure 4.17 shows seasonal variation of the percentage of time various values of fade depth are exceeded for Durban. Figure 4.18 shows the same for Cape Town. It can be seen that for both cases, the proportion of time that a certain fade depth varies from season to season. For this reason, ITU-R [7] suggests planning around the worst month. In considering the worst month for both the locations, Durban has higher percentages of occurrence than Cape Town even though both are coastal towns. This can be attributed to their difference in climatic types and this stresses the need to determine the geoclimatic factor for each region for more accurate predictions.

Figures 4.19 – 4.21 show probability in percentages, that a certain fade depth is exceeded for Pretoria, Bloemfontein and Polokwane respectively. For these inland locations, the link parameters used were adjusted to take their altitudes into effect but still maintaining the path inclination constant as for the coastal towns. This is to make sure that the variation in probability of time that a certain fade depth is exceeded is due to the geoclimatic factor of the area. For Durban, Pretoria and Polokwane, the worst month is in February (summer) which compares well with the work of Dabideen et al [63] in which the highest probability of duct occurrence was found to be in February. ITU-R [22] also confirms the same for the probability of duct occurrence. Duct occurrence has high correlation with multipath fading [63].

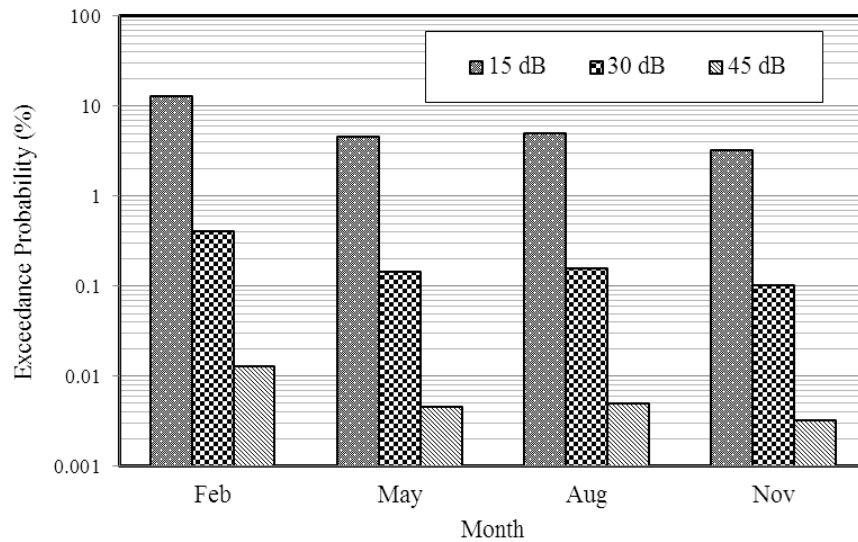


Figure 4.17: Probability of time a specific fade depth A (dB) is exceeded for Durban

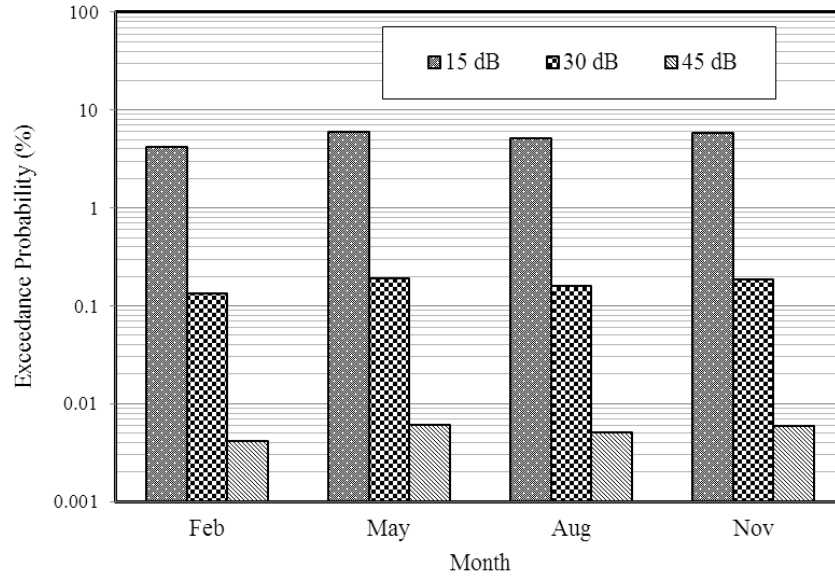


Figure 4.18: Probability of time a specific fade depth $A(\text{dB})$ is exceeded for Cape Town

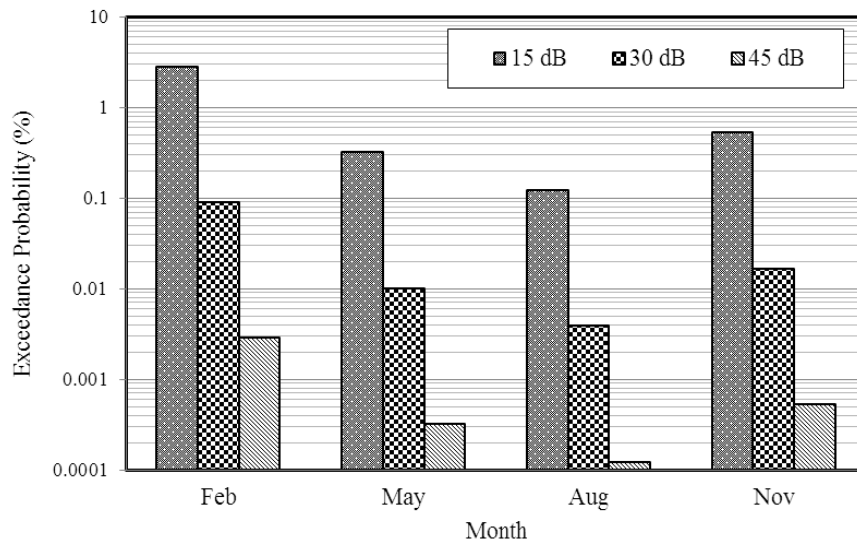


Figure 4.19: Probability of time a specific fade depth $A(\text{dB})$ is exceeded for Pretoria

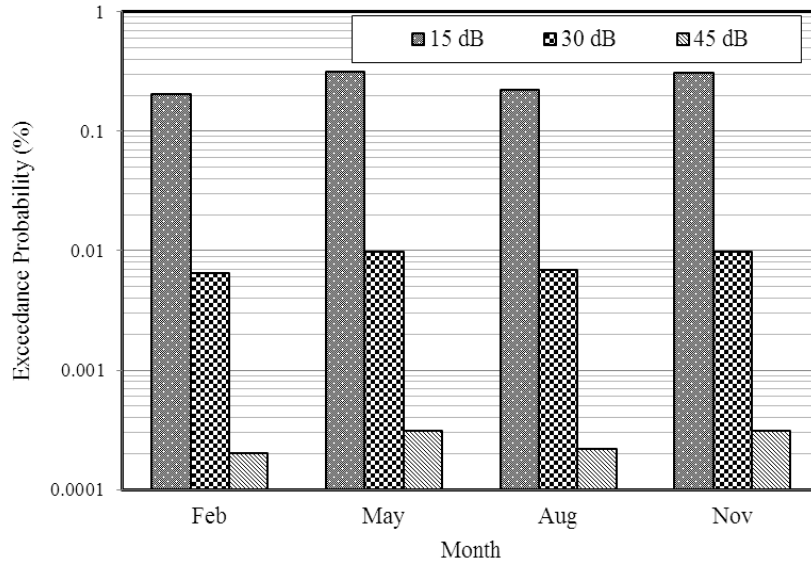


Figure 4.20: Probability of time a specific fade depth A (dB) is exceeded for Bloemfontein

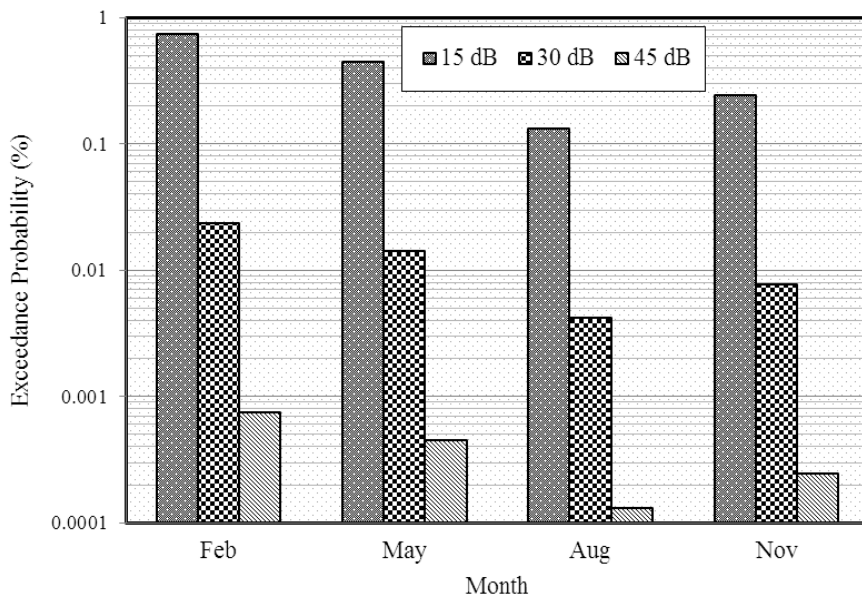


Figure 4.21: Probability of time a specific fade depth A (dB) is exceeded for Polokwane

Multipath propagation can either result in multipath fading or signal enhancement. The fade depth exceeded for 0.01 % of the time is required in predicting system availability for a certain percentage of time [7]. In our study, we determine this value of fade depth exceeded for 0.01 % of time with same link parameters as before but with varying frequency as shown in Figure 4.22 at a fixed hop length for both Durban and Cape Town. In Figure 4.22, R^2 is the coefficient of determination, x is the link frequency and y is the $A_{0.01}$. We again determine this value at a single frequency with varying path length. This is displayed in Figure 4.23. R^2 and y is as defined earlier and x is the path length. Figure

4.22 shows that the fade depth exceeded increases rapidly with increase in frequency up to about 5 GHz after which the increase is less sharp with increasing frequency. Figure 4.23 shows that path length determines a lot the value of fade depth exceeded for 0.01 % of the time. Longer path lengths experience higher values of fade depth exceeded. This can be attributed to the fact that for long distance, multipath is more pronounced because of multiple reflections due to bending of radio beam by the more negative refractivity gradient. The fade depth exceeded for 0.01 % of time can be approximated by logarithmic fits with very high coefficient of determination. For Figure 4.22, the fade depth for 0.01 % ($A_{0.01}$) link unavailability can be modelled as a power law with link frequency as the variable given by:

$$A_{0.01} = 3.4797 \ln f + 37.723 \text{ (dB)} ; R^2 = 0.9997 \text{ for Durban} \quad (4.7)$$

and

$$A_{0.01} = 3.4505 \ln f + 34.436 \text{ (dB)} ; R^2 = 0.9994 \text{ for Cape Town} \quad (4.8)$$

The corresponding root mean square error (RMSE) for the above equations is 0.244845 for Durban and 0.242782 for Cape Town. Similarly, for Figure 4.23, the fade depth for 0.01 % ($A_{0.01}$) link unavailability can be modelled as a power law with path distance as the variable given by:

$$A_{0.01} = 17.566 \ln d - 21.714 \text{ (dB)} ; R^2 = 0.9996 \text{ for Durban} \quad (4.9)$$

and

$$A_{0.01} = 17.574 \ln d - 25.067 \text{ (dB)} ; R^2 = 0.9996 \text{ for Cape Town} \quad (4.10)$$

The corresponding root mean square error (RMSE) for the above equations is 0.059243 for Durban and 0.076368 for Cape Town. The biggest challenge with modelling the probability of multipath fading distributions is that it is frequency selective and path dependent. Therefore, the fading distribution can only be modelled for single frequency with varying path distance or at a fixed path distance with varying frequency.

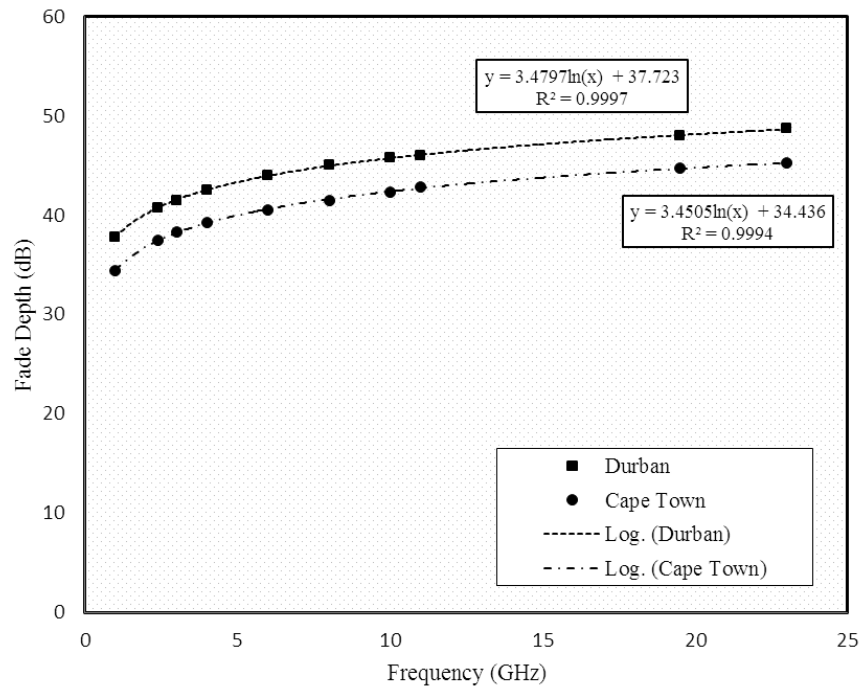


Figure 4.22: Fade depth exceeded for 0.01 % of the time with varying frequency at fixed path length (48.25 km)

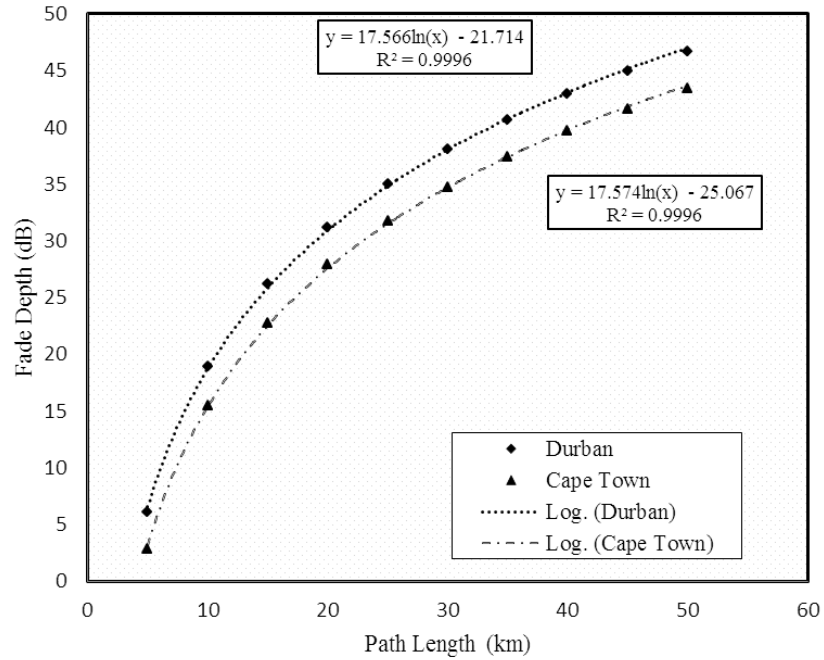


Figure 4.23: Fade depth exceeded for 0.01 % of the time with varying path length at fixed frequency (11 GHz)

4.7 Validation and Comparison of Results

The average worst month value for Durban from the three year radiosonde data is used to compare the outage probability with that obtained earlier in Durban by Dabideen et al [63] and, Odedina and Afullo [28]. The first link is between Sherwood and Umlazi in Durban with the following link parameters: $f = 11$ GHz, $h_e = 159$ m, $h_r = 243$ m, and $d = 25$ km. The measured fade depth exceeded for a certain proportion of time, for various hop availability is modelled via both ITU-R P530-12 and ITU-R P530-14 models, with geoclimatic factor K as determined as described in the previous sections. These values are compared with values obtained by Dabideen et al [63], in which they computed their probabilities of exceedance using ITU-R P530-10. This is shown in Table 4.9 below.

Table 4.9: Comparison of fade depth exceeded for various link availability in Durban

Outage (%)	Availability (%)	$A_{ITU-RP530-10}$	$A_{ITU-RP530-12}$	$A_{ITU-RP530-14}$
1	99	16	16.22	16.4
0.1	99.9	26	26.22	26.4
0.01	99.99	36	36.22	36.4
0.001	99.999	46	46.22	46.4

We compute the outage probability for the above link with other models i.e., we compare the outage probability for the fade depth gotten from ITU-R P530-14 for 0.01% unavailability with other Barnett-Vigants and Morita models. The results show that, in Durban, the outage probability can be predicted with the Barnett-Vigants model for coastal region. Table 4.10 provides a comparison of outage probability from ITU-R method with the region-based methods; Barnett-Vigants method and Morita method of USA and Japan respectively. From the table with the same fade depth, Barnett-Vigants method gives an outage probability of 0.0094 % for coastal region. The same model for other region performs poorly for Durban. This can be attributed to the fact that Durban is also a coastal region. Morita model for coastal provides an outage probability of 0.0157 %, and hence over estimates the outage probability for Durban.

Table 4.10: Comparison of outage probability of a typical link in Durban, a coastal town in South Africa: ITU-R vs Barnett-Vigants/Morita

Model	Region	Outage Probability (%)
ITU-R P530-14		0.0100
	Coastal	0.0094
Barnett-Vigants	average	0.0024
	Mountainous	0.0006
	Coastal	0.0157
Morita	Plains	0.0032
	Mountainous	0.0012

The second link is between Westville Campus and Howard College Campus of University of KwaZulu-Natal with the following link parameters: $f = 19.5$ GHz, $h_e = 202$ m, $h_r = 165$ m and $d = 6.73$ km. From the link measurement analysis by Odedina and Afullo [28], [22], the received signal level differs from the expected value of -41 dBm by 1-4 dB, which they attribute to clear air factors when the transmit power is 100 mW (20 dBm). The received signal values are much higher than the receiver noise level that varies from -79.5 dBm to -82 dBm [28]. From the mean received signal, the outage probability for the link equals 0.00019 % and 0.00014 % estimated using ITU-R P530-12 and ITU-R P530-14 respectively. This implies that the average received signal is much higher than the squelch level; therefore the link availability is quite good even with low fade margin. From ITU-R models, $A_{0.01}$ for the link is found to be 19.78 dB and 18.43 dB for ITU-R P530-12 and ITU-R P530-14 respectively. The comparison of fade depth for $A_{0.01}$ for the two links confirms that fading due to multipath is more pronounced over long path lengths, as shown in the examples for Rwanda below.

Measurements from three links in Rwanda, Central Africa, are used to estimate outage probability. Average received signal for each month is computed from which the fade margin is estimated. This is used in ITU-R models for predicting the likelihood that a certain fade depth is surpassed in a given link. Table 4.11 below shows typical link parameters and their expected received signal levels. Figures 4.24 – 4.26 show the monthly mean received signal levels in dBm for each of the links; transmitting power is 0.28 watts (24.5 dBm) in all the cases. The variations in signal levels can be attributed to atmospheric multipath propagation [5]

Table 4.11: Link Parameters in Rwanda, Central Africa [5]

Link	d (km)	h_e (m)	h_r (m)	f (GHz)	Rx (dBm)
Jali-Gahengeri	34.54	2084.64	1767	8	-56.57
Gahengeri-Kibungo	33.41	1663	1777	8	-40.47
Nyakarambi-Nasho	17.14	1901	1764	8	-42.50

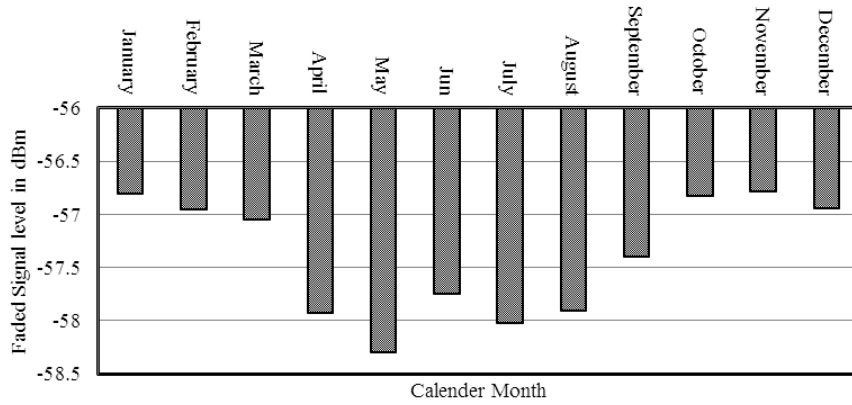


Figure 4.24: Monthly Mean Received Signal Level for Jali-Gahengeri Link [5]

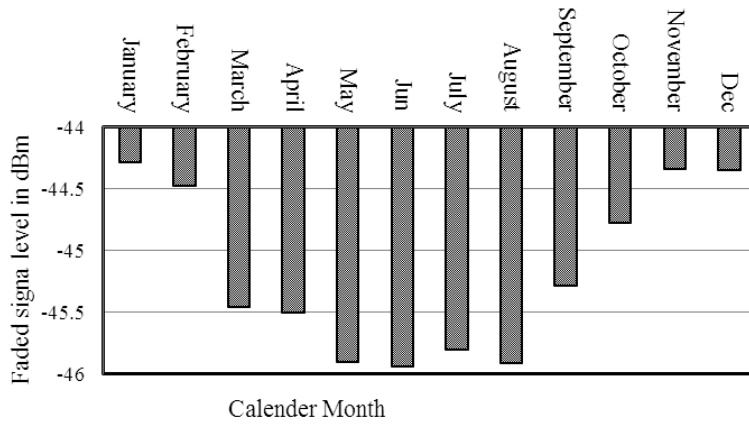


Figure 4.25: Monthly Mean Received Signal Level for Gahengeri-Kibungo Link [5]

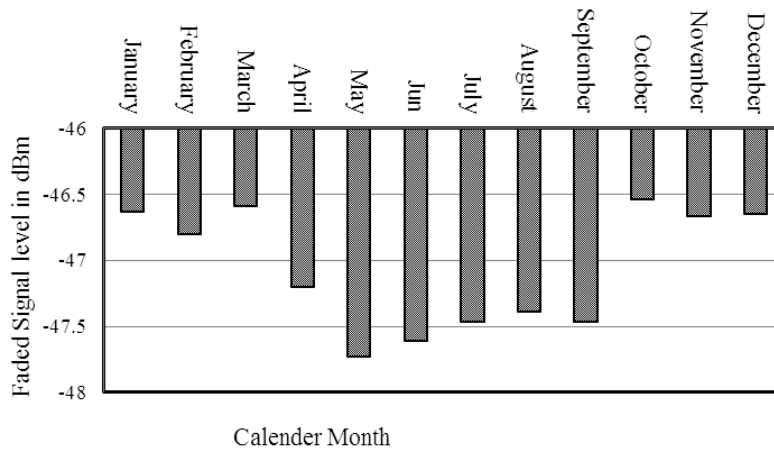


Figure 4.26: Monthly Mean Received Signal Level for Nyakarambi-Nasho Link [5]

Djuma [5] used ten year surface measurements data from meteorological service from Tanzania bordering Rwanda to estimate point refractivity gradients for four regions. The value for the region closest to Rwanda (Bukoba) was used in estimating outage probabilities

for links in Rwanda. The worst month values for various regions are tabulated in the Table 4.12 below [5]. The worst months are in summer seasons and compare well with South African worst months which are generally in summer months as tabulated earlier in Table 4.2.

The estimated geoclimatic factor K is used with link parameters in Table 4.11 to compute the fade depth exceeded for 0.01 % of the time. The results are shown in Table 4.13. They further estimated outage probabilities for the three links by determining the fade margin from mean received value and receiver noise level. Outage occurs when the received signal level is below the receiver noise level. Fade margin levels obtained from link measurements are 13.11 dB, 25.33 dB and 23.46 dB for Jali-Gahengeri, Gahengeri-Kibungo and Nyakarambi-Nasho, respectively. Corresponding outage probabilities are also tabulated in Table 4.13. Receiver threshold noise levels for all the links is -70.5 dBm.

Table 4.12: Point refractivity gradient and geoclimatic factor values for regions in Tanzania

	Point Refractivity Gradient (NU/km)	Geoclimatic Factor K	
		ITU-R P530-12	ITU-R P50-14
Bukoba (Feb)	-588	3.20×10^{-3}	9.72×10^{-4}
Mwanza (Jan)	-644	4.65×10^{-3}	1.38×10^{-3}
Kigoma (Dec)	-589	3.22×10^{-3}	9.78×10^{-4}
Musoma (Mar)	-901	2.59×10^{-2}	6.80×10^{-3}

Table 4.13 shows that the outage probabilities of the three links in Rwanda are lower than those in Durban with shorter path lengths. This is partly due to lower frequency used in Rwanda and partly due to a more hilly terrain of Rwanda compared to Durban. This can be confirmed by comparing Jali-Gahengeri and Gahengeri-Kibungo links with close link distance. Jali-Gahengeri link which is more hilly (higher surface roughness factor), needs a lower fade margin than for Gahengeri-Kibungo link even though the Gahengeri-Kibungo link used higher gain antennas than the Jali-Gahengeri link. Transmitting/receiving antenna gains used are 41 dBi and 30.8 dBi for Gahengeri-Kibungo link and Jali-Gahengeri link respectively [5].

Table 4.13: Outage probabilities for three links in Rwanda

	ITU-R P530-12		ITU-R P530-14	
	$A_{0.01}$ (dB)	Outage (%)	$A_{0.01}$ (dB)	Outage (%)
Jali-Gahengeri	14.06	0.01248	16.05	0.01971
Gahengeri-Kibungo	19.52	0.00263	21.74	0.00438
Nyakarambi-Nasho	< 10	0.00018	< 10	0.00026

4.8 Chapter Conclusion

In this Chapter, multipath fading has been examined in relation to the prevailing climatic conditions in five regions of South Africa. Cumulative distribution of refractivity gradient in the lowest 65 m above the ground was determined, from which the point refractivity gradient was estimated. However, in cases where the value was not observable, the Inverse Distance Square (IDS) method has been used to approximate the value. The point refractivity gradient estimated for the regions was found to be more negative than the ITU-R value for South Africa. The ITU-R value of point refractivity gradient for the region is -400 N units/km while the estimated value derived from three year radiosonde data was found to be -460 N units/km.

Results show that refractivity gradient varies for different locations in South Africa and each region/location need to be considered individually for accurate predictions. The worst month values of point refractivity gradient for Durban, Pretoria and Polokwane are -599 N units/km, -850 N units/km and -538 N units/km respectively, all occurring in the month of February. The worst month values point refractivity gradient for Cape Town and Bloemfontein occur in May and are -476 N units/km and -443 N units/km respectively. The geoclimatic factor K for the various regions has then been predicted from the various values of point refractivity gradient. It was confirmed that the geoclimatic factor which caters for geographical and climatic conditions in multipath fading distribution varies with the month, season and year. The value is also region-based and hence there is need to determine the value for regions of interest for more accurate prediction of fading phenomena. The results also indicate that the worst month varies annually and it generally occurs in the summer months in most of South Africa apart from Mediterranean region (Cape Town) and Steppe region (Bloemfontein) where it occurs in autumn (May).

Outage probability in Durban is compared to three links in Rwanda. It is confirmed that even though the geoclimatic factor of the two regions are close, outage probability in Rwanda which is hillier than Durban is lower. A comparison for outage probability found from ITU-R method for a typical link in Durban was also made with those from Barnett-Vigants method and Morita method for the same fade depth. It was found that Barnett-Vigants method for coastal regions performs better than Morita for coastal region in the case of Durban link.

Chapter 5

Mapping of Geoclimatic Factor K

5.1 Introduction

A deep fading estimation technique is the most significant component of practically all methods for estimating outage due to multipath on terrestrial microwave LOS links. Most of these methods are created on experimental fits of Rayleigh-type distributions to the fading data for different nations and are categorised in terms of climatic environments. ITU-R provides a global method for predicting the percentage of time that a certain fade depth is exceeded in the average worst month. Apart from link variables, the ITU-R method, has additional variable, the geoclimatic factor K . This variable takes into account the inconsistency of climate and topography. It is suggested that the geoclimatic factor K be estimated from fading data from the neighbourhood links of the intended link if such data exist. Nevertheless, in most cases such data is unavailable; estimation methods based on refractivity gradient measurements are suggested.

In this chapter, geoclimatic factor K derived from radiosonde data for five locations in South Africa are used to estimate and map the values for all the regions in South Africa. Three spatial interpolation techniques: Kriging, Inverse Distance Weighting and Thin-Plate Spline, are used in estimating the geoclimatic factor in places where data is not observable. Statistical assessment of these methods is done by calculating the mean absolute error (MAE) and the root mean squared error (RMSE) between a set of control points and the interpolated results. The best performing method estimated values is used to map the seasonal geoclimatic factor K for the entire study region. The estimated values of geoclimatic factor will improve accuracy in predicting multipath outage in LOS links in the region.

5.2 Applications of Spatial Interpolation Methods

Spatial interpolation techniques have been applied in varied fields of study to create a continuous surface data for informed decisions. It has found applications in climatology [9, 48], in electromagnetic field estimation [47,49], in radioactive contamination [50], aerospace engineering [51], in optics [53], among others. The challenge is always the choice of the best interpolation method to be used and the best performance analysis criteria [46,47]. In this study we employ the three most used techniques: Inverse distance weighting (IDW), Kriging and Thin-plate spline. The background information and characteristics of these methods has been discussed earlier in Chapter 3, Section 3.4. The symbols used here are

as defined earlier in Section 3.4. In this chapter, we apply these techniques as outlined herein.

5.2.1 Kriging

The procedure used in implementing kriging is as follows [51, 52]:

1. Calculate the empirical semi-variogram by the following steps:
 - i Determine the euclidean distance i.e., $d_{ij} = \sqrt{(x_i - x_j)^2 + (y_i - y_j)^2}$, where x_{ij} and y_{ij} are coordinates of data points.
 - ii Compute the semi-variance from the data set. It is recommended that for large data, one need to group the pairs of locations, referred as binning.
 - iii Plot the average semi-variance against distances of the bins onto a graph
2. Fitting the model i.e., drawing a line that offers the best fit of the semi-variogram cloud graph. This is done using least square fit such that the difference between each point and the line is as low as possible.
3. Create the matrices - the matrices here are those of spatial covariance used for estimating the kriging weights (see Chapter 3, Section 3.4.1)
4. The last step is to estimate the unknown values by multiplying the weights of each measured value times the value, and then adding the products together.

5.2.2 Thin Plate Spline

The accuracy of Thin-plate spline is dependent on the smoothing parameter. The smoothing parameter separates the continuous surface from noise [9]. The algorithm for implementing thin plate spline is as follows [9, 53]:

1. Estimate the optimized smoothing parameter by minimizing the general cross validation (GCV) given by (3.59).
2. Estimate the continuous spline function F from (3.57) that best represent the process g in (3.56).
3. The predicted values is then found from (3.60).

5.2.3 Inverse Distance Weighting (IDW)

The IDW method is the most simple and very direct method to implement among the three, since only distance separating data points is involved in estimating the weights. It is given as follows [46, 47]:

1. The first step is to determine the euclidean distance, using the equation similar to one used in kriging
2. Estimate the weights, i.e., $\lambda_i = \frac{1}{\sum_{i=1}^n \frac{1}{(d_i)^p}}$. The optimised power parameter p is determined by the following procedure:
 - i Each measured point is removed from the data set and compared with the predicted value for that location.
 - ii RMSE is calculated from the values of observed and approximated value from step (i).
 - iii A number of RMSE is plotted for several power parameters for the same data set.
 - iv A curve is fitted from the plot in (iii) and the power parameter that provides the minimum RMSE is used as the optimised value.
3. Lastly estimate the unknown value at a position or location from $Z'(x_o) = \sum_{i=1}^n \lambda_i Z(x_i)$.

The parameters are as defined earlier in Chapter 3.

5.3 Methodology

5.3.1 Data Collection

Seasonal geoclimatic factor estimated from the procedure given in the previous chapter is used in interpolation and mapping of geoclimatic factor for the whole of South Africa. Table 5.1 shows five stations with their geographical locations expressed in latitudes and longitudes. The four month values were derived from three year radiosonde sounding taken twice per day and represent the four seasons exhibited in South Africa. The sounding data were reported after every ten seconds which gives a fairly good height resolutions.

Table 5.1: Discrete Observable Data used in Mapping and their Latitudes/Longitudes

	Latitude	Longitude	February	May	August	November
Pretoria	25.707	28.229	4.97×10^{-3}	5.58×10^{-4}	2.13×10^{-4}	9.15×10^{-4}
Durban	29.850	31.017	1.04×10^{-3}	3.65×10^{-4}	4.07×10^{-4}	2.60×10^{-4}
Cape Town	33.917	18.417	3.35×10^{-4}	4.84×10^{-4}	4.11×10^{-4}	4.73×10^{-4}
Bloemfontein	29.133	26.200	2.58×10^{-4}	3.95×10^{-4}	2.79×10^{-4}	3.93×10^{-4}
Polokwane	23.900	29.450	7.13×10^{-4}	4.28×10^{-4}	1.25×10^{-4}	2.32×10^{-4}

5.3.2 Data Processing

Data processing, analysis and representation was carried out using PAST version 2.16 (July 2012) and MATLAB version 2010a. PAST is a free software tool distributed under GNU/GPL licence. It is a data analysis package that includes common statistical, plotting and modelling functions. Interpolation of data was done using PAST and plotting of contours was done in MATLAB.

5.3.3 Error Analysis

Since there is no preferred interpolation method, the choice of the appropriate method for a certain task is made based on its accuracy [47] among other factors. One of the methods used in method assessment is error analysis. There are very many measures of fit for error analysis; in our study, we have applied the root mean square error (RMSE) and the mean absolute error(MAE). RMSE gives measure of inaccuracy though is sensitive to outliers as it emphasises a lot of weight to large errors while MAE is less sensitive to extreme values. However, they are amongst the best measures of performance of a model because they give a summary of the average difference in units of estimated and observed values [46].

Control sites where discrete data exist are used in performance analysis by removing these observed values from data to be processed and then using interpolation techniques to predict these observed values (i.e., cross validation). Error calculation is then done using (5.1) and (5.2). The method that gives the minimum values of error is assumed to be the best performing method. Pr_j is the predicted value and Ob_j is the observed value at various control sites, and n is the number of control sites. The control points are chosen randomly for large data points; however, where data points are few, all points become control points.

$$RMSE = \frac{1}{n} \sum_{j=1}^n (Pr_j - Ob_j)^2 \quad (5.1)$$

$$MAE = \frac{1}{n} \sum_{j=1}^n |Pr_j - Ob_j| \quad (5.2)$$

Table 5.2: Error analysis applied to interpolation techniques

Measure of fit		IDW	Spline	Kriging		
				Spherical	Exponential	Gaussian
Feb	RMSE	1.59×10^{-3}	5.58×10^{-3}	2.36×10^{-3}	2.28×10^{-3}	2.45×10^{-3}
	MAE	1.16×10^{-3}	5.37×10^{-3}	1.81×10^{-3}	1.73×10^{-3}	1.92×10^{-3}
May	RMSE	5.10×10^{-5}	2.04×10^{-4}	7.69×10^{-5}	7.44×10^{-5}	8.13×10^{-5}
	MAE	4.04×10^{-5}	1.96×10^{-4}	6.28×10^{-5}	6.06×10^{-5}	6.82×10^{-5}
Aug	RMSE	1.68×10^{-5}	8.95×10^{-5}	2.60×10^{-5}	2.60×10^{-5}	3.36×10^{-5}
	MAE	1.41×10^{-5}	7.98×10^{-5}	2.35×10^{-5}	2.40×10^{-5}	3.19×10^{-5}
Nov	RMSE	2.29×10^{-4}	6.48×10^{-4}	3.32×10^{-4}	3.23×10^{-4}	3.40×10^{-4}
	MAE	1.64×10^{-4}	5.84×10^{-4}	2.38×10^{-4}	2.33×10^{-4}	2.47×10^{-4}

5.4 Results and Discussion

Part of the results have been published elsewhere [64], and this chapter gives a comprehensive details of these results. The interpolation process was carried out using Inverse distance weighting, Thin-plate spline and ordinary Kriging. Three models of variogram were used in Kriging: Spherical, Exponential and Gaussian. Each of the season's values were interpolated and contour plots given for each season .i.e. Figure 5.1 – 5.5, show the contour plots for February, Figures 5.6 – 5.10, show plots for May. Figures 5.11 – 5.15, show the plots for August and the plots of November are shown in Figures 5.16 – 5.20 . It should be noted that the algorithms calculate the raster layer, considering all pixels within the rectangle defined by the latitudes and longitudes and may at times fall out of the intended South African region. It is therefore important for one to know the longitudes and latitudes for the region/place of interest.

Some contours show geoclimatic factor to be zero, which cannot be the case. These points are far away from the discrete data points, hence the influence of the discrete data points tends to zero, giving this abnormality. The worst case is seen in Figure 5.2, where even within the study area, negative values geoclimatic factor are seen. Similar case is seen in Figure 5.5.

Table 5.2 shows the measures of fit carried out. From the results, it can be seen that the lowest MAE and RMSE is recorded by Inverse distance weighting method for all the seasons. Hence we can conclude that IDW is the best performing method in this study. This is then followed by Kriging. Kriging performance is influenced by the variogram model used. For our data set, the exponential model has the lowest error among the three variogram models, followed by spherical model. At some points the error between the exponential model and spherical model is negligible. The Gaussian model fit seems to be the worst performing kriging model. The worst performing techniques is Thin-plate spline. The performance of Thin-plate spline can be attributed to the nature of our data. Thin-plate spline works well with data sets with gently varying surfaces (data sets having low variance).

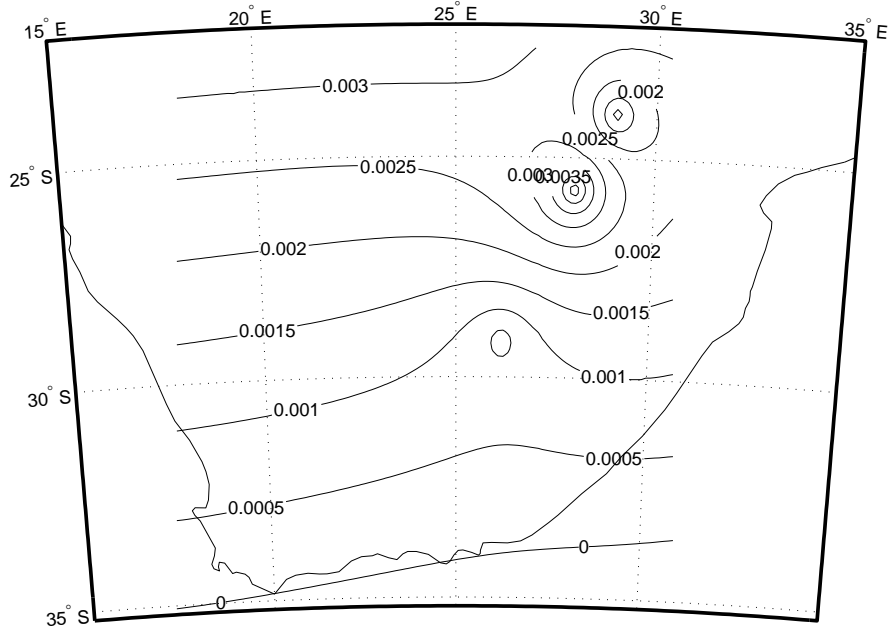


Figure 5.1: Contour plot for the geoclimatic factor K for February using inverse distance weighting

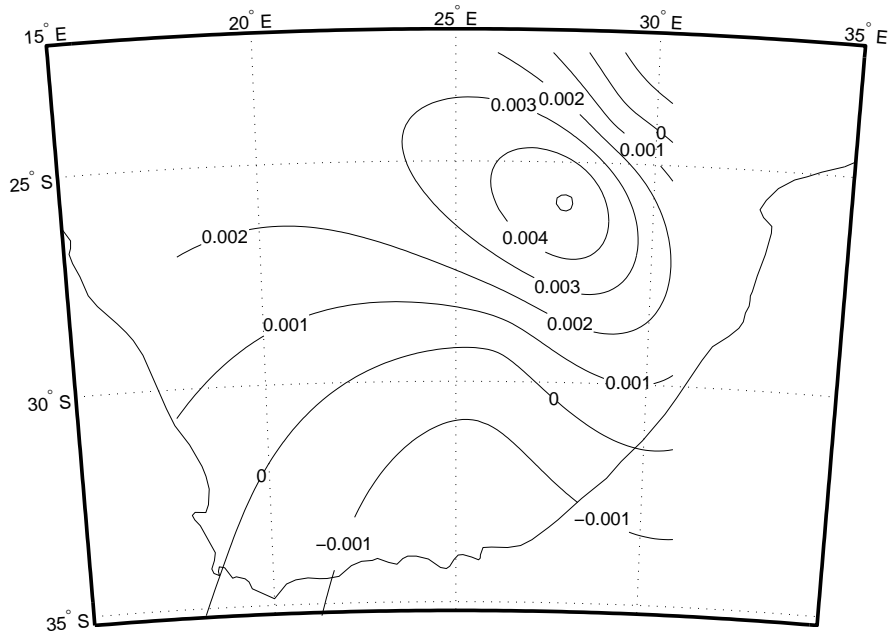


Figure 5.2: Contour plot for the geoclimatic factor K for February using thin-plate spline

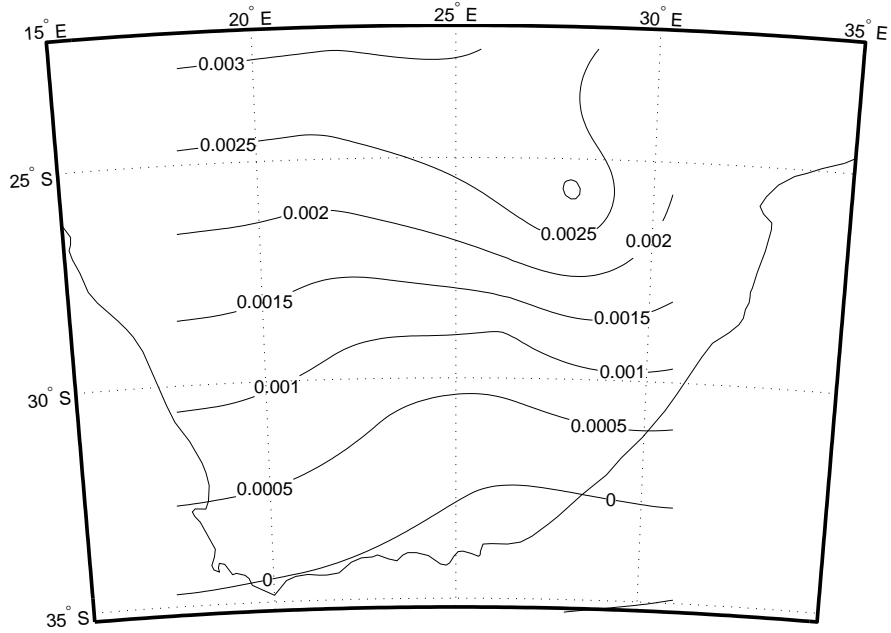


Figure 5.3: Contour plot for the geoclimatic factor K for February using kriging (spherical)

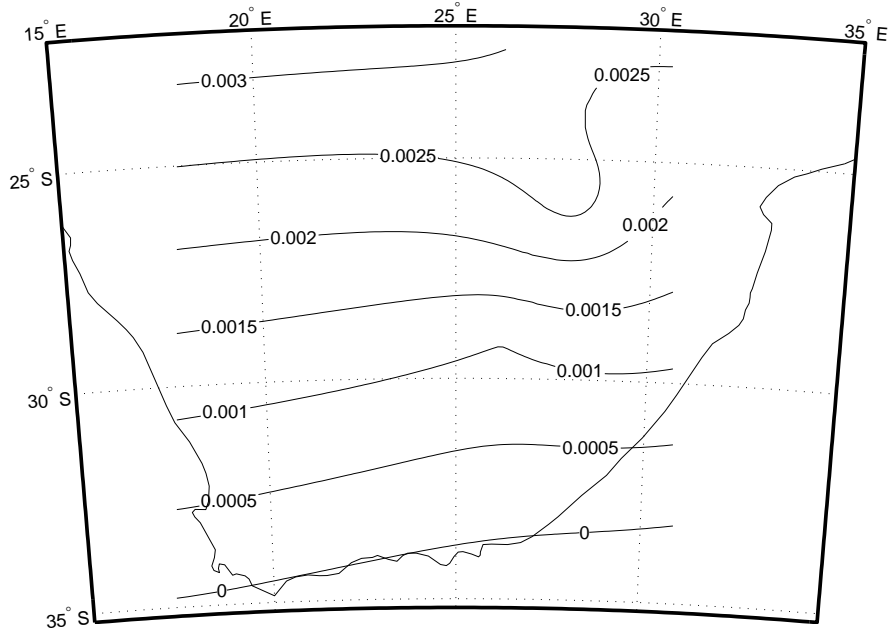


Figure 5.4: Contour plot for the geoclimatic factor K for February using kriging (exponential)

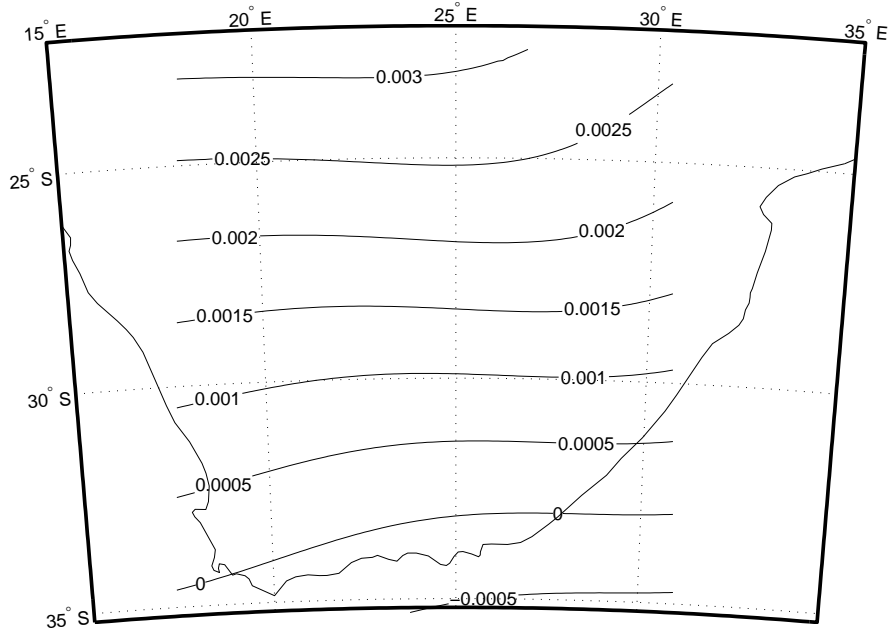


Figure 5.5: Contour plot for the geoclimatic factor K for February using kriging (Gaussian)

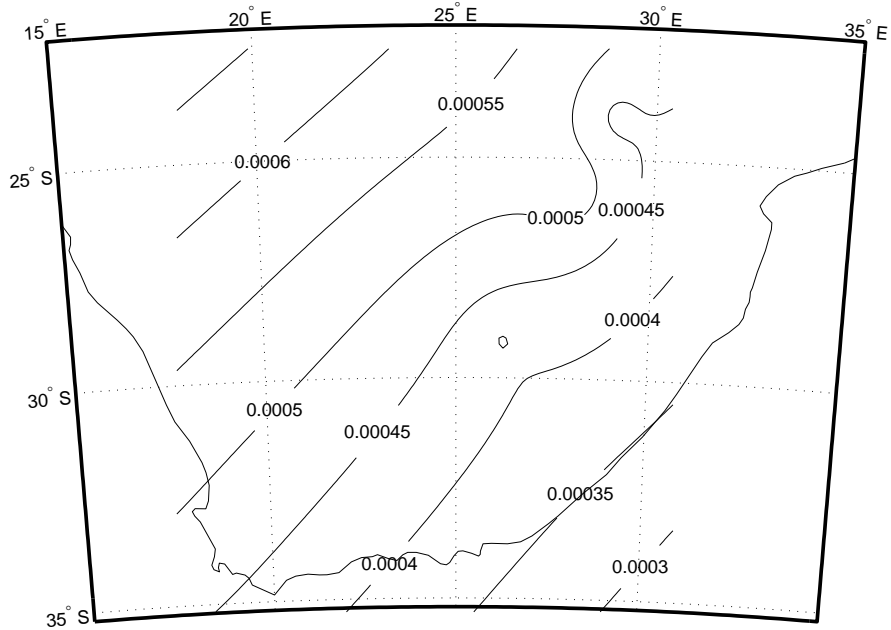


Figure 5.6: Contour plot for the geoclimatic factor K for May using inverse distance weighting

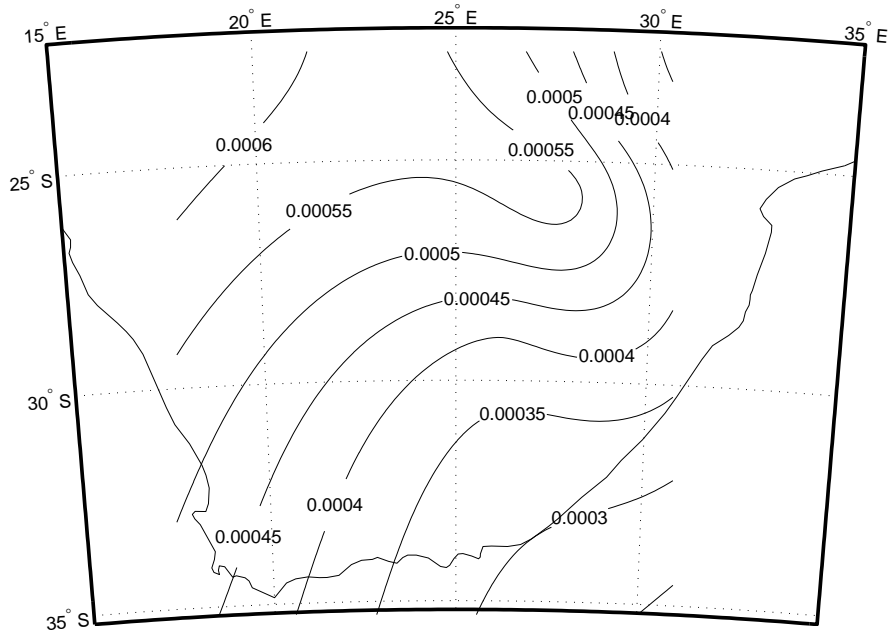


Figure 5.7: Contour plot for the geoclimatic factor K for May using thin-plate spline

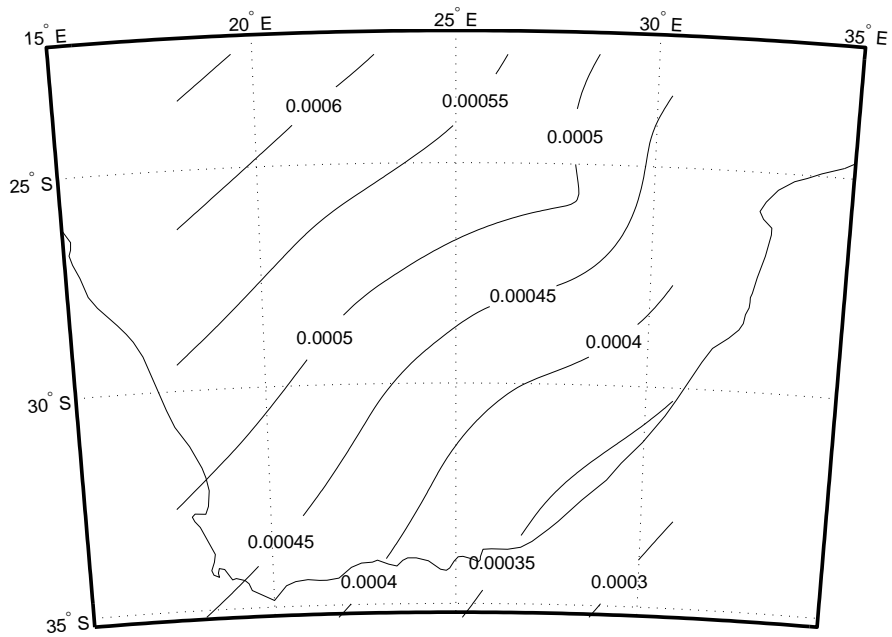


Figure 5.8: Contour plot for the geoclimatic factor K for May using kriging (spherical)

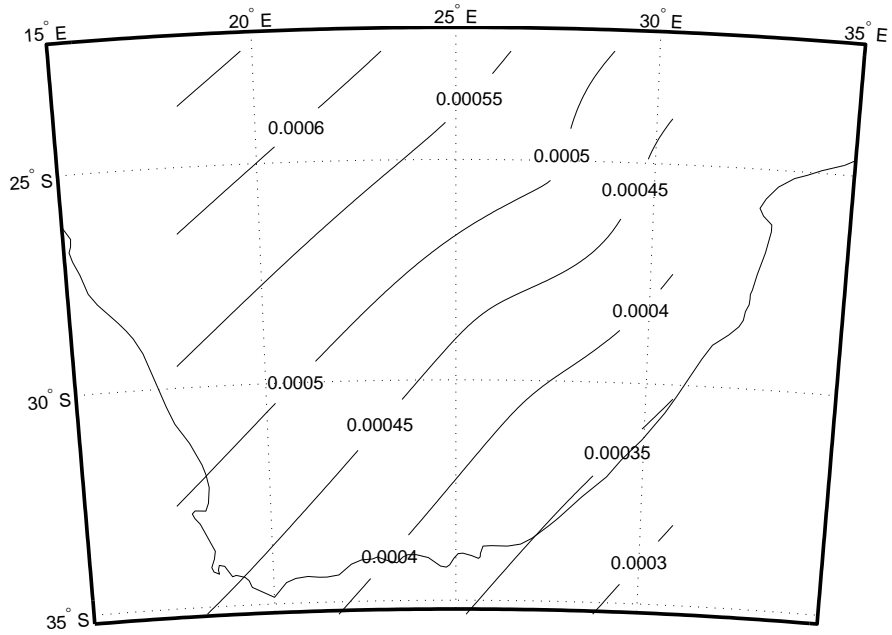


Figure 5.9: Contour plot for the geoclimatic factor K for May using kriging (exponential)

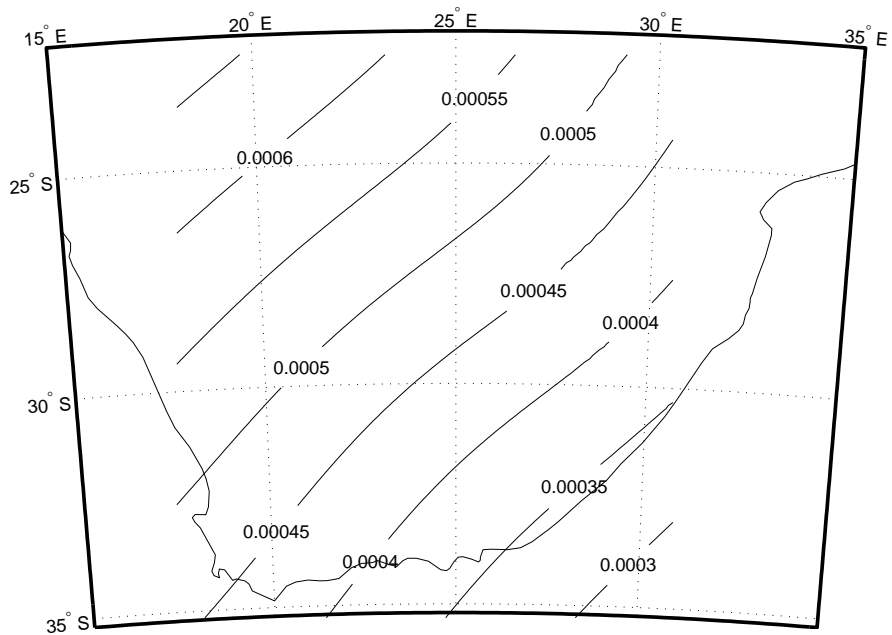


Figure 5.10: Contour plot for the geoclimatic factor K for May using kriging (Gaussian)

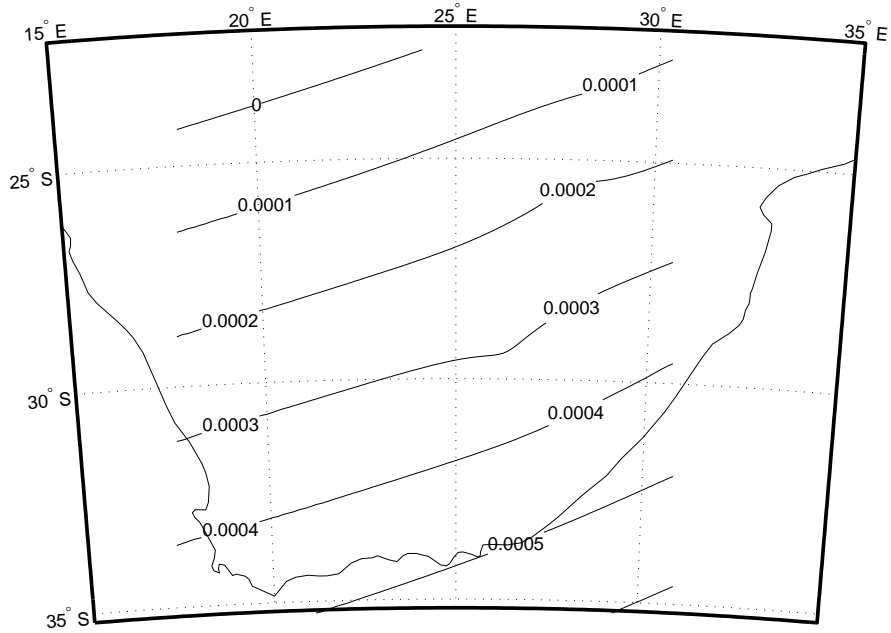


Figure 5.11: Contour plot for the geoclimatic factor K for August using inverse distance weighting

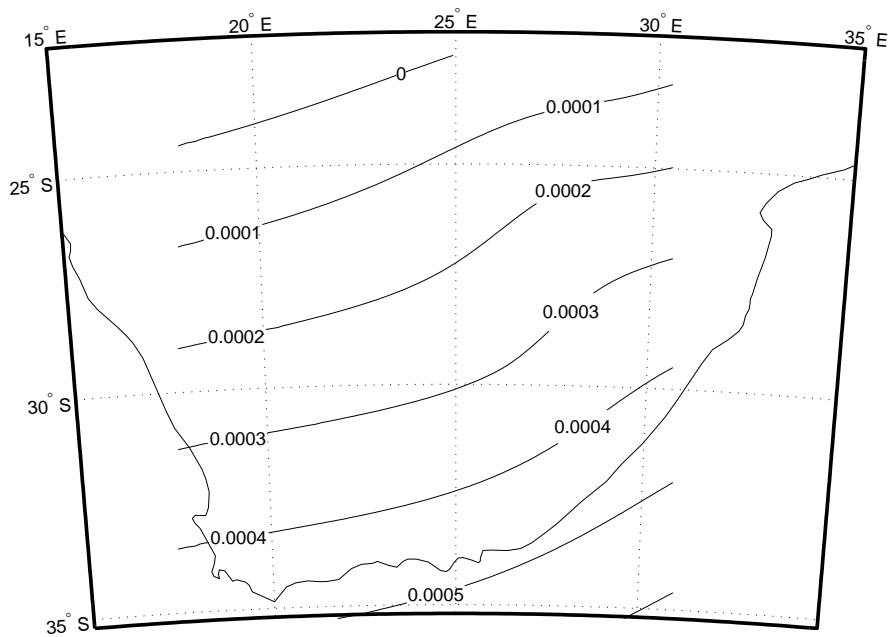


Figure 5.12: Contour plot for the geoclimatic factor K for August using thin-plate spline

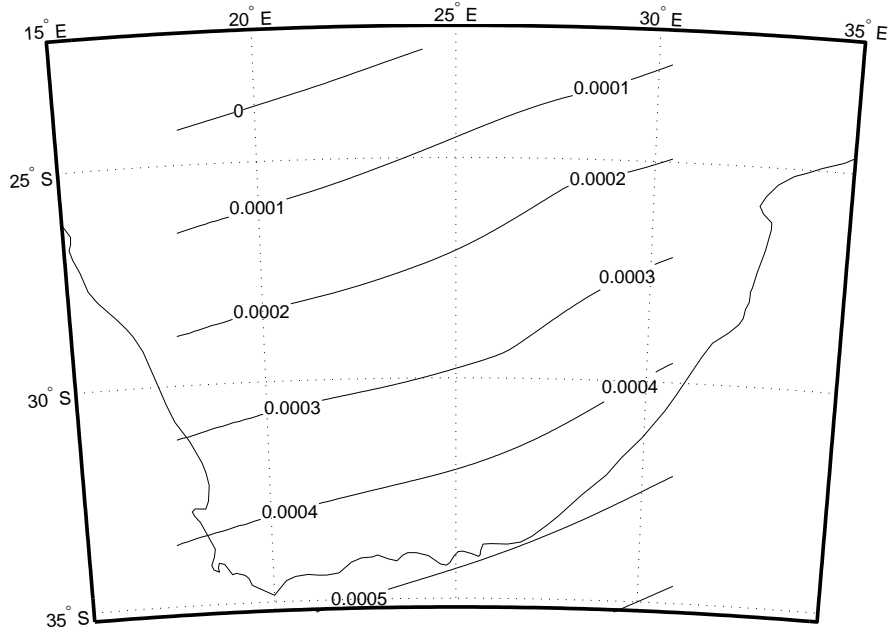


Figure 5.13: Contour plot for the geoclimatic factor K for August using kriging (spherical)

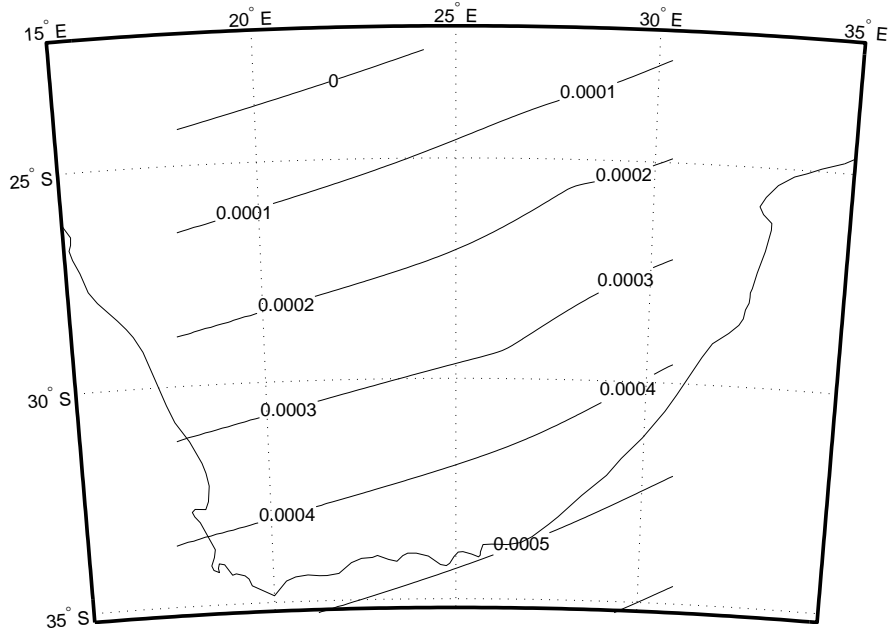


Figure 5.14: Contour plot for the geoclimatic factor K for August using kriging (exponential)

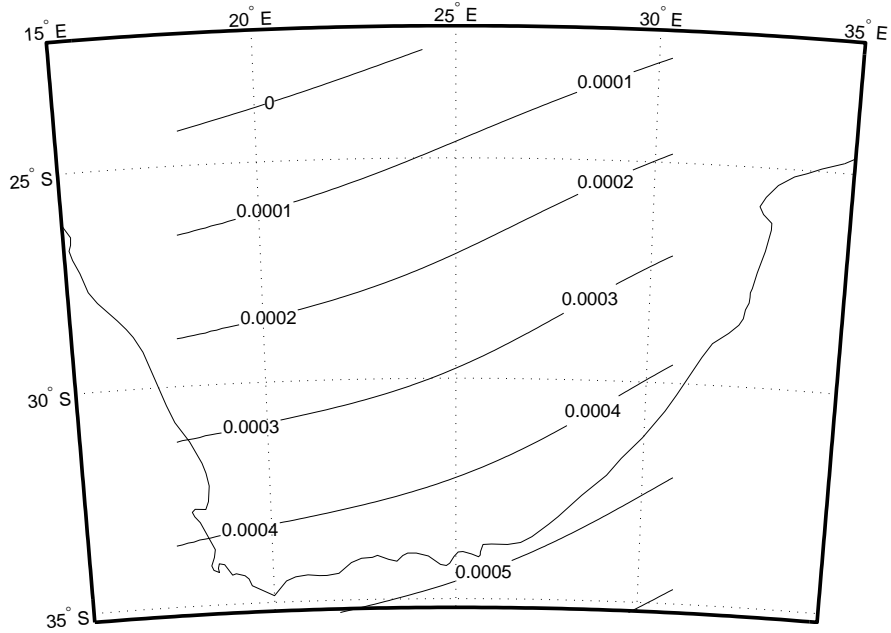


Figure 5.15: Contour plot for the geoclimatic factor K for August using kriging (Gaussian)

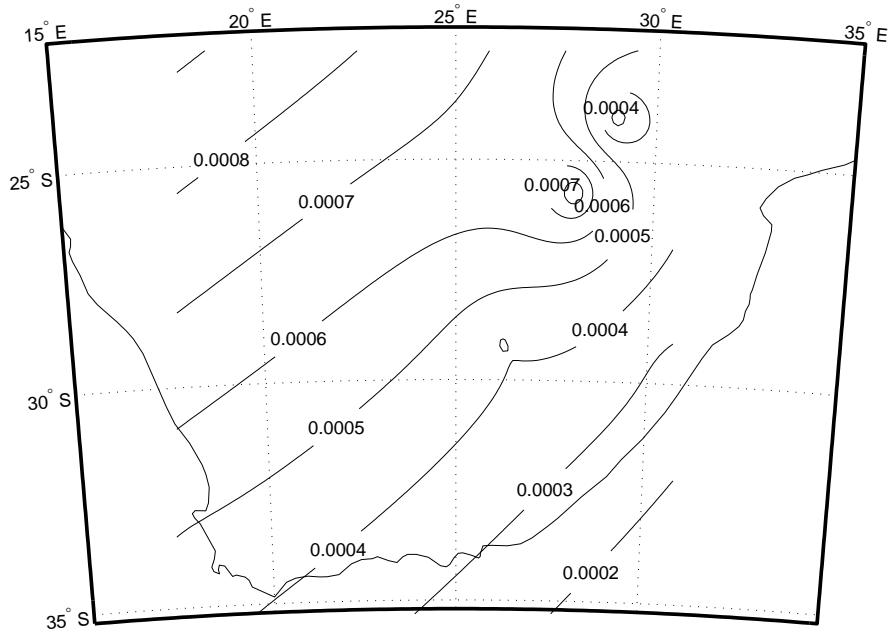


Figure 5.16: Contour plot for the geoclimatic factor K for November using inverse distance weighting

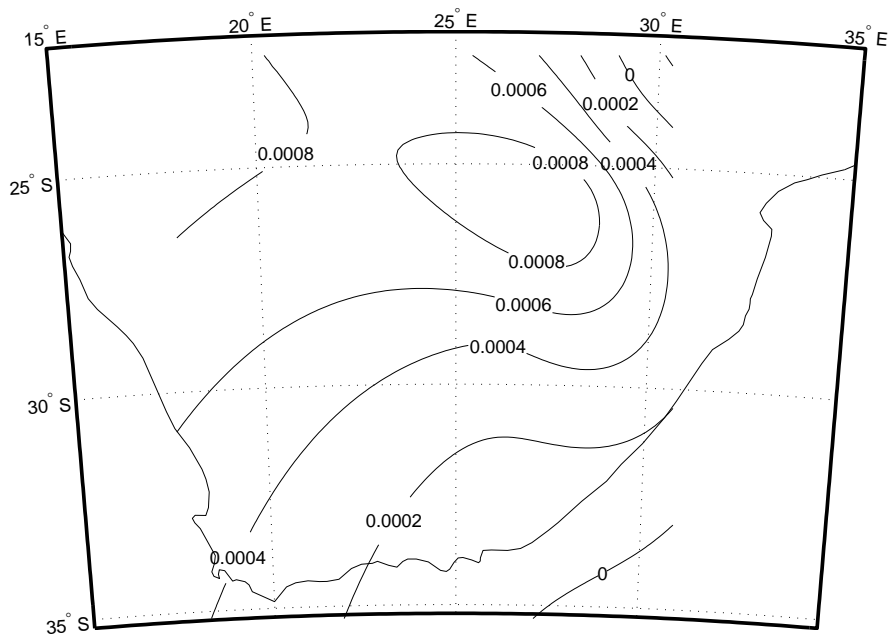


Figure 5.17: Contour plot for the geoclimatic factor K for November using thin-plate spline,

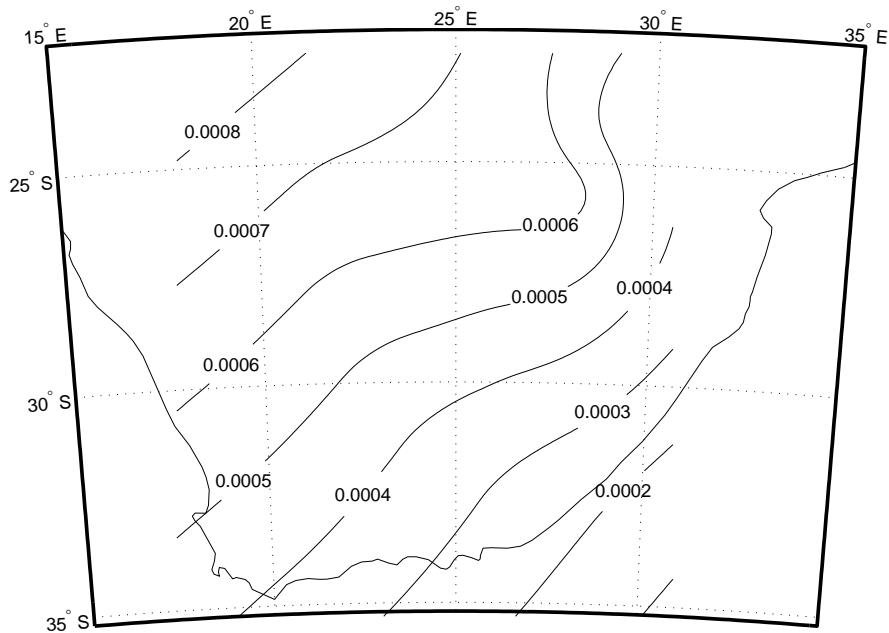


Figure 5.18: Contour plot for the geoclimatic factor K for November using kriging (spherical)

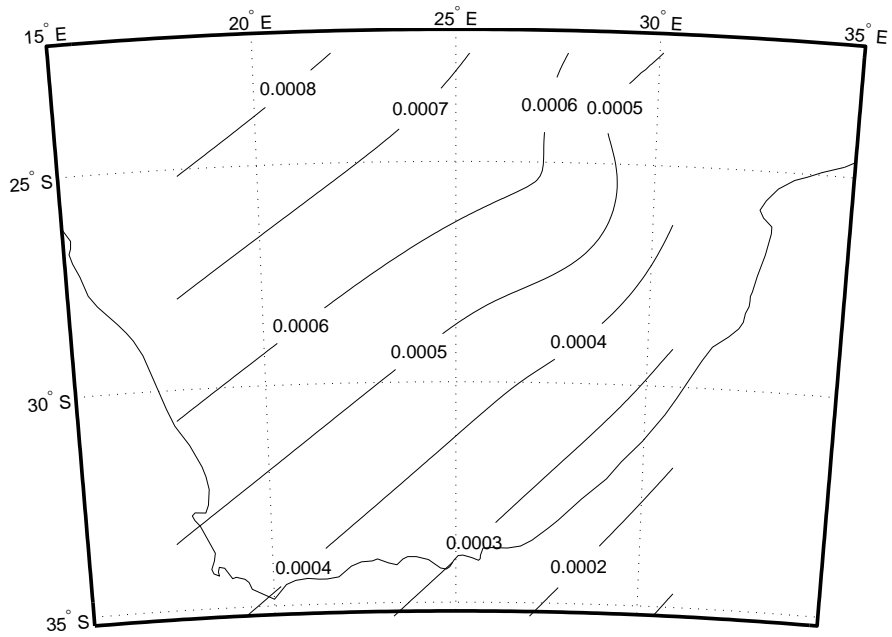


Figure 5.19: Contour plot for the geoclimatic factor K for November using kriging (exponential)

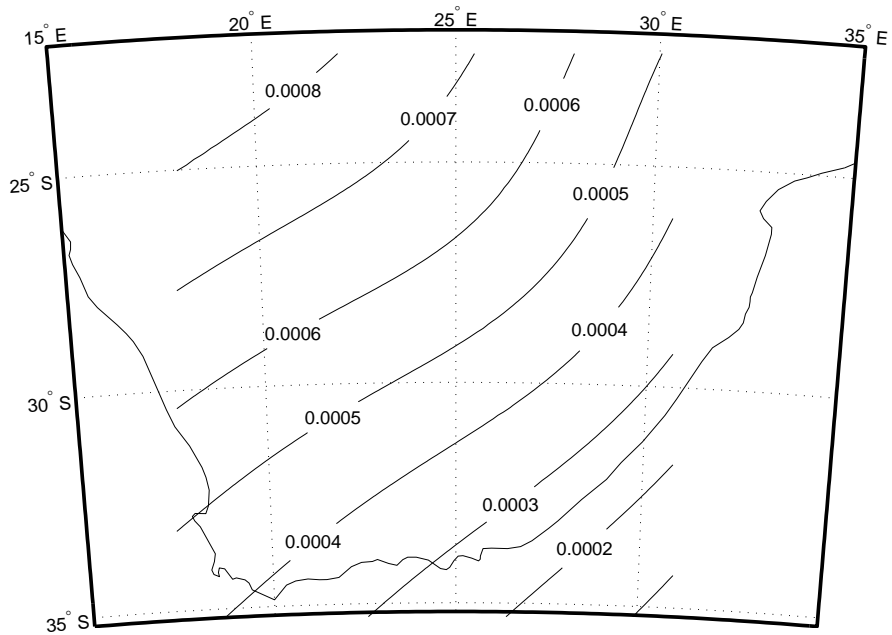


Figure 5.20: Contour plot for the geoclimatic factor K for November using kriging (Gaussian)

5.5 Chapter Conclusion

In this chapter, it can be concluded that Inverse distance weighting gives the best performance in interpolating the geoclimatic factor K . Geoclimatic factor depend on the variability of the atmosphere specifically temperature, pressure and relative humidity. If we assume that regions close to each other tend to exhibit the climatic conditions, then, we can certain that IDW is the best method for interpolating the geoclimatic factor. However, it is also known that the geoclimatic factor also depends on the topology of the area in addition to climatic conditions, hence more study needs to be done on this by incorporating fading data of given regions to the climatic conditions for a more decisive conclusion on the distribution of this factor in the region of study. It can be shown that different techniques used in evaluation give different results, making it a necessity to choose the best technique which gives the minimum error of performance. The best technique can further be optimized for better accuracy. The IDW here can be optimized by adjusting the power parameter and the search radius.

Chapter 6

Conclusion

6.1 Concluding Remarks

Terrestrial microwave LOS links are heavily used in communication systems. Their performance and availability are influenced by atmospheric conditions of the unguided wireless medium. The accuracy in predicting multipath fading distributions is key to proper LOS links of high reliability. This study used the geoclimatic factor approach and ITU-R recommendations P530-14 to obtain the multipath fading occurrence in five cities in South Africa, including Durban. A comparison was made with the outage probability by earlier work in Durban and Rwanda in Central Africa. It was confirmed that even though the geoclimatic factor of the two regions are close, outage probability in Rwanda which is hillier than Durban is lower, since hillier environments are less prone to multipath fading. Three-year radiosonde data was used in estimating the percentage of time that a certain fade depth is exceeded and hence outage probability due to atmospheric multipath propagation, assuming the given fade depth leads to the received signal falling below the squelch level.

Inverse Distance Square technique was employed to estimate point refractivity gradient not exceeded for 1 % of the time in the lowest 65 m above the ground for five locations within South Africa. The values of point refractivity gradient obtained are used in determining the geoclimatic factor K . The results presented show monthly, seasonal and annual variation of both point refractivity gradient and geoclimatic factor K . The results confirm that the geoclimatic factor K is region based. The percentage of time that a given fade depth is exceeded for a single frequency increases rapidly with increasing path length. This is due to the fact that as the path length increases so are the multiple reflections leading to multipath propagation, which results in multipath fading.

A typical LOS link in Durban, South Africa has been used to compare the outage probability obtained from ITU-R model with other two region-based models: the Barnett-Vigants model of USA and the Morita model of Japan. The results show that ITU-R model and Barnett-Vigants methods for coastal region give close estimates for the probability of outage for the Durban link. It was found that for a certain fade depth exceeded for 0.01 % of the time obtained from ITU-R method for quick planning, the Barnett-Vigants model for coastal region gave a close value of 0.0094 %. For the same fade depth, Morita model provides a probability of 0.0157 %.

It was also found that Inverse Distance Weighting performs better than other interpolation methods used. It is followed in accuracy by the Kriging method. In kriging

method, three variogram models were used: spherical, exponential and Gaussian. The study also revealed that for our data set, exponential model has the least error followed by spherical and lastly Gaussian. Among the three methods, thin-plate spline gave the highest error. Hence, we can conclude that for our data set, IDW provides the least error but this does not necessarily mean that it will always be the best interpolator.

6.2 Future Work

The study has dwelt much on the prediction on fade depth and outage probability due to atmospheric multipath. To the design engineer, knowledge of fade depth alone is not enough in understanding the fading phenomena. We propose that fade data from established links in the area/region be obtained for analysis to come up with the distribution of two other fade parameters: fade rate and fade duration.

We also recommend that for proper understanding of diurnal and spatial variation of refractivity gradient, refractometers or sensors installed on towers be used in measuring atmospheric refractivity. This will be able to resolve both poor time and space resolution of radiosonde sounding data.

For geoclimatic mapping, we recommend that more data be used in the interpolation so that the continuous data surfaces obtained by spatial interpolation techniques be much smoother.

References

- [1] L. Harvey, *Microwave Transmission Networks: Planning, Design and Deployment*. McGraw Hill, New York, 2010.
- [2] R. L. Freeman, *Radio System Design for Telecommunications*. John Wiley & Sons, 1997.
- [3] T. Manning, *Microwave Radio Transmission Design Guide*. Artech House, 2009.
- [4] M. O. Fashuyi, “A study of rain attenuation on terrestrial paths at milliwave wavelengths in South Africa,” MSc Thesis, University of KwaZulu-Natal, South Africa, 2006.
- [5] S. Djuma, “Clear-air microwave signal prediction on terrestrial paths in Central Africa,” MSc Thesis, National University of Rwanda, Rwanda, July 2012.
- [6] R. L. Olsen and T. Tjeta, “Worldwide techniques for predicting the multipath fading distribution on terrestrial LOS links: Background and results of tests,” *IEEE Transactions on Antennas and Propagation*, vol. 47, no. 1, pp. 157–170, January 1999.
- [7] ITU-R, “Propagation data and prediction methods required for the design of terrestrial line-of-sight systems,” International Telecommunications Union, Geneva, Recommendation of ITU-R P.530-14, February 2012.
- [8] M. Grabner *et al.*, “Multipath fading measurement and prediction on 10 GHz terrestrial link,” in *Proc. of IEEE 15th Conference of Microwave Techniques*, April 19-21, 2010.
- [9] P. A. Hancock and M. F. Hutchison, “Spatial interpolation of large climate data sets using bivariate thin plate smoothing splines,” *Environmental Modelling and Software*, vol. 21, pp. 1684–1694, 2006.
- [10] J. Bogucki and E. Wielowieyska, “Empirical season’s fading in radio communication at 6 GHz band,” *Journal of Telecommunications and Information Technology*, vol. 2, pp. 48–52, 2009.
- [11] G. Radha and M. Rao, “Addendum to study on coastal atmospheric effects on LOS links located in Visakhapatnam,” *AU J.T.*, vol. 10, no. 4, pp. 276–281, April 2007.
- [12] J. S. Seybold, *Introduction to RF Propagation*. John Wiley & Sons, 2005.
- [13] L. E. Braten *et al.*, “Time dynamic attenuation on a fixed radio communication link at 6 GHz in Western Norway,” COST Action 280, Norway, R&D Report R55, December 2002.
- [14] T. J. Afullo and P. K. Odedina, “On the k-factor distribution and diffraction fading for Southern Africa,” *South African Institute of Electrical Engineers Africa Research Journal*, vol. 97, no. 2, pp. 172–181, June 2006.
- [15] P. K. Odedina and T. J. Afullo, “Use of spatial interpolation technique for determination of geoclimatic factor and fade depth calculation in Southern Africa,” in *Proc. IEEE AFRICON Conference*, Windhoek, Namibia, September, 26-28, 2007.
- [16] P. Valtr and P. Pechac, “Tropospheric refraction modelling using ray-tracing and parabolic equation,” *Radioengineering*, vol. 14, no. 4, pp. 98–104, December 2005.

- [17] K. Naicker and S. H. Mneney, "Propagation measurements and multipath channel modelling for line-of-sight links at 19.5 GHz," *South African Institute of Electrical Engineers Africa Research Journal*, vol. 92, no. 2, pp. 162–171, June 2006.
- [18] P. Valtr *et al.*, "A terrestrial multi-receiver radio link experiment at 10.7 GHz-comparisons of results with parabolic equation calculations," *Radioengineering*, vol. 19, no. 1, pp. 117–121, April 2010.
- [19] M. Grabner and V. Kvicera, "Clear-air propagation modelling using parabolic equation method," *Radioengineering*, vol. 12, no. 4, pp. 50–54, December 2003.
- [20] S. D. Gunashekar *et al.*, "Transhorizon radiowave propagation due to evaporation ducting," *Resonance, Springer, India*, vol. 11, no. 1, pp. 51–62, January 2006.
- [21] J. A. Schiavone, "Prediction of positive refractivity gradients for line-of-sight radio paths," *The Bell System Technical Journal*, vol. 60, no. 6, pp. 803–822, August 1981.
- [22] ITU-R, "The radio refractivity index: Its formula and refractivity data," Institution of Telecommunication Union, Geneva, Switzerland, Recommendation of ITU-R P. 453-9, February 2012.
- [23] J. D. Parsons, *The Mobile Radio Propagation Channel*. Wiley, West Sussex, 2000.
- [24] H. V. Hitney, "Refractive effects from VHF to EHF: Propagation mechanisms," in *Propagation Modelling and Decision Aids for Communications, Radar and Navigation Systems*, AGARD Lecture series 196, pp.4A - 4B, September 1994.
- [25] M. O. Asiyoy and T. J. Afullo, "Tropospheric propagation mechanisms influencing multipath fading based on local measurements," in *Proc. of Southern Africa Telecommunication Networks and Applications Conference*, Fancourt, George, South Africa, September 2-5, 2012.
- [26] V. Herbertand *et al.*, "Tropospheric radio propagation assessment," *Proceedings of the IEEE*, vol. 73, no. 2, pp. 265–283, February 1985.
- [27] R. L. Olsen *et al.*, "Worldwide techniques for predicting the multipath fading distribution on terrestrial LOS links: Comparison with regional techniques," *IEEE Transactions on Antennas and Propagation*, vol. 51, no. 1, pp. 23–30, January 2003.
- [28] P. K. Odedina and T. J. Afullo, "Clear air signal level measurements for microwave line-of-sight link application in South Africa," *South African Institute of Electrical Engineers Africa Research Journal*, vol. 101, no. 4, pp. 132–139, December 2010.
- [29] T. Tjelta *et al.*, "Systematic development of new multivariable techniques for predicting the distribution of multipath fading on terrestrial microwave links," *IEEE Transactions on Antennas and Propagation*, vol. 38, no. 10, pp. 1650–1665, October 1990.
- [30] W. T. Barnett, "Multipath propagation at 4, 6, and 11 GHz," *Bell System Technical Journal*, vol. 51, no. 2, pp. 321–361, February 1972.
- [31] A. Vigants, "Space diversity engineering," *Bell System Technical Journal*, vol. 54, no. 1, pp. 103–142, January 1975.
- [32] B. L. Agba *et al.*, "Comparison of microwave links prediction methods: Barnett-Vigants vs. ITU methods," in *Proceedings of Progress In Electromagnetics Research Symposium*, Xi'an, China, March, 22-26 2010.
- [33] H. R. Anderson, *Fixed Broadband Wireless System Design*. John Wiley & Sons, 2003.
- [34] A. Vigants, "Number and duration of fades at 4 and 6 GHz," *Bell System Technical Journal*, vol. 50, no. 3, pp. 815–841, March 1971.

- [35] B. L. Agba *et al.*, “Recent evolution of ITU method for prediction of multipath fading on terrestrial microwave links,” in *Proceedings of Progress In Electromagnetics Research Symposium*, Marrakesh, Morocco, March, 20-23 2011.
- [36] ITU-R, “Propagation data and prediction methods required for the design of terrestrial line-of-sight systems,” International Telecommunications Union, Geneva, Recommendation of ITU-R P.530-08, October 1999.
- [37] —, “Propagation data and prediction methods required for the design of terrestrial line-of-sight systems,” International Telecommunications Union, Geneva, Recommendation of ITU-R P.530-09, February 2001.
- [38] —, “Propagation data and prediction methods required for the design of terrestrial line-of-sight systems,” International Telecommunications Union, Geneva, Recommendation of ITU-R P.530-13, October 2009.
- [39] T. J. Afullo and P. K. Odedina, “Effective earth radius factor characterization for line of sight paths in Botswana,” in *Proc. IEEE 7th AFRICON Conference*, September 15-17, 2004.
- [40] —, “Effective earth radius factor measurement and modelling for radio link design in Botswana,” *South African Institute of Electrical Engineers Africa Research Journal*, vol. 99, no. 3, pp. 77–86, September 2008.
- [41] P. K. Odedina and T. J. Afullo, “Multipath propagation modelling and measurement in a clear-air environment for LOS link design application,” in *Proc. of Southern Africa Telecommunication Networks and Applications Conference*, Ezulwini Swazi, Royal Spa, Swaziland, September 2009.
- [42] A. J. Palmer and D. C. Baker, “Predicting the monthly average cumulative distribution of the effective earth radius factor for South Africa,” *South African Institute of Electrical Engineers Africa Research Journal*, vol. 92, no. 2, pp. 186–190, June 2006.
- [43] —, “A model for the fraction of time availability of the effective earth radius factor for communications planning in South Africa: Part I-the basic model,” *South African Institute of Electrical Engineers Africa Research Journal*, vol. 93, no. 1, pp. 1–7, 2002.
- [44] —, “Predicting the long-term average of the effective earth radius factor for South Africa using ground based observations,” *South African Institute of Electrical Engineers Africa Research Journal*, vol. 92, no. 2, pp. 182–185, June 2006.
- [45] —, “A novel simple semi-empirical model for the effective earth radius factor,” *IEEE Transactions on Broadcasting*, vol. 52, no. 4, pp. 557–565, December 2006.
- [46] L. Jin and A. D. Heap, “A review of comparative studies of spatial interpolation methods in environmental sciences: Performance and impact factors,” *Ecological Informatics*, vol. 6, pp. 228–241, December 2011.
- [47] M. Azpurua and K. D. Ramos, “A comparison of spatial interpolation methods of average electromagnetic field magnitude,” *Progress in Electromagnetics Research M*, vol. 14, pp. 135–145, September 2010.
- [48] A. D. Hartkanp *et al.*, “Interpolation techniques on climate change,” International Maize and Wheat Improvement Centre, Netherlands, Tech. Rep., 1999.
- [49] J. Triantafilis *et al.*, “Five geostatistical models to predict soil salinity from electromagnetic induction data across irrigated cotton,” *Soil Science Society AM. J.*, vol. 65, pp. 869–878, May-June 2001.
- [50] E. Savelieva, “Using ordinary kriging to model radioactive contamination data,” *Applied GIS Mornash University press*, vol. 1, no. 2, pp. 1–10, 2005.

- [51] T. W. Simpson, "Kriging models for global approximation in simulation-based multidisciplinary design optimization," *AIAA JOURNAL*, vol. 39, no. 12, pp. 2233–2241, December 2001.
- [52] H. Gunes *et al.*, "Data enhancement, smoothing, reconstruction and optimization by kriging interpolation," in *Proceedings of the 2008 Winter Simulation Conference*, 2008, pp. 379–386.
- [53] A. Ghosh, "Efficient thin plate spline interpolator and its applications to adaptive optics," MSc Thesis, Johannes Kepler University, Linz, Austria, August 2010.
- [54] S. L. Lystad *et al.*, "Interpolation of clear air parameters observed at non-regular observation locations," in *Proceedings of URSI CLIMPARA Commission F Open Symposium on Climatic Parameters in Radiowave Propagation Predictions*, Ottawa, Canada, April 27-29, 1998.
- [55] A. T. Adediji and M. O. Ajewole, "Vertical profile of radio refractivity gradient in Akure, South-West Nigeria," *Progress in Electromagnetic Research C*, vol. 4, pp. 157–168, 2008.
- [56] T. Tjelta *et al.*, "Correlation of observed multipath occurrence with climatic parameters derived from radiosondes, surface stations, and numerical atmospheric models," in *Proceedings of URSI CLIMPARA Commission F Open Symposium on Climatic Parameters in Radiowave Propagation Predictions*, Ottawa, Canada, April 27-29, 1998.
- [57] M. O. Fashuyi *et al.*, "Rainfall rate modelling for LOS radio systems in South Africa," *South African Institute of Electrical Engineers Africa Research Journal*, vol. 97, no. 1, pp. 74–81, March 2006.
- [58] M. O. Asiyo and T. J. Afullo, "Statistical estimation of fade depth and outage probability due to multipath fading in Southern Africa," *Progress In Electromagnetics Research B*, vol. 46, pp. 251–274, 2013.
- [59] A. Abu-Alman and K. Al-Ansari, "Calculation of effective earth radius and point refractivity gradient in UAE," *International Journal of Antennas and Propagation*, vol. 2010, no. 1, pp. 1–4, 2010.
- [60] P. K. Odedina and T. J. Afullo, "Estimation of secondary radioclimatic variables and its application to terrestrial LOS link design in Southern Africa," in *Proc. IEEE AFRICON Conference*, Wild Coast Sun, South Africa, September, 7-10, 2008.
- [61] A. Stergios and D. Thomas, "Ten years analysis of tropospheric refractivity variations," *Annals of Geophysics*, vol. 47, no. 4, pp. 1333–1337, August 2004.
- [62] K. A. Ansari and R. A. Kamel, "Correlation between ground refractivity and refraction gradient and their statistical and worst month distribution in Abu Dhabi," *IEEE Antennas and Propagation Letters*, vol. 7, pp. 233–235, 2008.
- [63] A. S. Dabideen *et al.*, "Radio refractivity distribution and duct and fading occurrence measurements in KwaZulu-Natal," *South African Institute of Electrical Engineers Africa Research Journal*, vol. 96, no. 2, pp. 121–132, June 2005.
- [64] M. O. Asiyo and T. J. Afullo, "Spatial interpolation for mapping geoclimatic factor K in South Africa," in *Proceedings of Progress in Electromagnetic Research Symposium*, Taipei, Taiwan, March, 25-28 2013.